HIGH FIDELITY NUMERICAL INVESTIGATIONS OF TAILORED MAGNETIC FIELDS FOR DEFECT REDUCTION IN CONTINUOUS CASTING OF STEEL

BY

RAMNIK SINGH

THESIS

Submitted in partial fulfillment of the requirements
for the degree of Master of Science in Mechanical Engineering
in the Graduate College of the
University of Illinois at Urbana-Champaign, 2013

Urbana, Illinois

Advisers:

Professor Surya P. Vanka
Professor Brian G. Thomas

ABSTRACT

In the Continuous Casting (CC) process, defects are created when the inclusions are entrained deep into the strand and are entrapped in the solidifying shell. Both the creation and entrapment of inclusions are a function of transient fluid flow behavior in the mold along with the inclusion properties. This thesis focuses on better understanding of mold flow with Electromagnetic Braking (EMBr), which is an attractive method due to its non-intrusive nature. EMBr greatly influences turbulent flow in the continuous casting mold and its transient stability, which affects level fluctuations and inclusion entrainment. Large eddy simulations are performed to investigate these transient flow phenomena using an accurate numerical scheme implemented on a Graphics Processing Unit (GPU). Two arrangements of EMBr are studied in this work, the single ruler EMBr configuration and the "Flow-Control-mold" or "FC-mold" EMBr configuration. The effects of each configuration are studied by comparing with corresponding cases without any applied magnetic field.

The in-house developed CFD model is first applied to simulate experiments conducted on a $1/6^{th}$ scale physical caster model with GaInSn as the low-melting conducting liquid and is then applied to the corresponding full-size caster to evaluate scaling criterion in the presence of applied magnetic fields. The mold flow has a classic "double-roll" flow pattern without the application of any magnetic fields. The application of ruler EMBr over the nozzle deflects the jets upwards and increases the top surface velocity. With insulated walls, the mold flow has large scale fluctuations and an unstable flow pattern. This instability is completely damped by using conducting side walls. These flow patterns are matched well in the corresponding real-size caster by maintaining only the Stuart number. However, to match the level fluctuations between the two casters, a Froude number ratio based scaling technique is applied.

The computational model is next applied to study transient flow in a real commercial steel caster and the computed results are compared with nail board measurements. Without magnetic fields, this caster exhibits a "double-roll" flow pattern, but with transient unbalanced flow oscillations, producing unbalanced flows and vortices which might be detrimental to steel quality. The application of a FC-mold EMBr damps this unbalanced flow behavior and also reduces surface velocity, surface level fluctuations, and variations in the surface level profile. Although this might lessen slag entrainment problems, the small surface velocities resulting from this strong magnetic field across the top surface may make the meniscus prone to freezing and associated surface defects.

To my parents and sister.

ACKNOWLEDGEMENTS

I express my sincere gratitude to my advisers Professor Pratap S. Vanka and Professor Brian G. Thomas for their continuous support and guidance during the course of my masters study.

I am also really grateful to the National Science Foundation (Grant No.: 11-30882) and the Continuous Casting Consortium for the financial support during my masters research. The simulations performed for this work were conducted at the Vanka CFD Laboratory at University of Illinois at Urbana-Champaign. CUFLOW, an in-house developed model, was used for the simulations in the current work and I would like to thank Aaron Shinn for the non-magnetohydrodynamic version of CUFLOW and Rajneesh Chaudhary for the magnetohydrodynamic version of CUFLOW. The experimental data for model validation in the GaInSn was provided by Mr. Klaus Timmel, Dr. Sven Eckert and Dr. Gunther Gerbeth from FZD, Dresden, Germany. I would also like to thank Rui Liu, a fellow researcher, for his help in taking the nail board measurements and postprocessing the nail boards.

Special thanks to my fellow researchers at the Vanka CFD Lab (Purushotam Kuman and Jeremy Horwitz) and at the Metals Processing Simulation Laboratory (Rui Liu, A.S.M. Jonayat, Lance Hibbeler, Seong-Mook Cho, Matthew Zappulla, Prathiba Duvvuri, Aravind Murali, Bryan Petrus, Kai Jin and Pete Srisuk) for making my work enjoyable. I would also like to thank my friends (Vartika Vaish, Swati Gupta, Peeyush Agarwal, Achal Asawa, Akshay Agarwal and Dinkar Nandwana) form making my stay at UIUC memorable.

Most of all I would thank my family, especially my parents and sister. Without their incessant inspiration and support this work would not have been possible.

TABLE OF CONTENTS

LIST OF ABBREVIATIONS

AC	Alternating Current
AMG	Algebraic Multigrid
CPU	Central Processing Unit
CSM	Coherent Structure Model
DC	Direct Current
DNS	Direct Numerical Simulations
EPE	Electric Potential Equation
EMBr	Electromagnetic Braking
EMLA	Electromagnetic Level Accelerator
EMLS	Electromagnetic Level Stabilizer
EMS	Electromagnetic Stirring
FC	Flow Control
GB	Gigabyte
GPU	Graphics Processing Unit
IR	Inner Radius
LES	Large Eddy Simulation
MHD	Magnetohydrodynamics
OR	Outside Radius
PPE	Pressure Poisson Equation
RANS	Reynolds-Averaged Navier-Stokes
SEN	Submerged Entry Nozzle
SGS	Sug-Grid Scale
SM	Streaming Multiprocessor
SOR	Successive Over Relaxation

SP	Streaming Processor
TKE	Turbulent Kinetic Energy
UDV	Ultrasonic Doppler Velocimetry
URANS	Unsteady Reyolds-Averaged Navier-Stokes
UTN	Upper Tundish Nozzle
WALE	Wall-Adapting Local Eddy-viscosity

LIST OF SYMBOLS

English

a	pressure coefficient
A	area
$\boldsymbol{B_0}$	applied magnetic field
C_s	Smagorinsky constant
C_w	WALE model constant
C_{CSM}	CSM model constant
$\boldsymbol{E}$	electric field
$\boldsymbol{F}$	body force term
Fr	Froude number
$\mathcal{F}_{cs}$	coherent characteristic velocity
G	filter function
g	gravitational acceleration
GHz	gigahertz
$\boldsymbol{H}$	sum of convection and diffusion terms
Ha	Hartmann number
h_{lump}	height difference at nail board lump
$\boldsymbol{J}$	induced current
L	characteristic length
$\boldsymbol{n}$	normal vector
N	Stuart number or interaction parameter
p	pressure
p^*	modified pressure for LES
Q	volume flow rate

Re	Reynolds Number
r	distance from SEN center
R	radius
S	source term
S_{ij}	rate-of-strain strain tensor
$\lvert\bar{S}\rvert$	magnitude of the rate-of-strain strain tensor
t	time
$\boldsymbol{u}$	velocity vector
U	characteristic velocity
u, v, w	Cartesian velocity components
x,y,z	Cartesian coordinates
$\boldsymbol{x}$	position vector

Greek

δ_{ij}	Kronecker delta
Δ	local filter width
$\Delta x, \Delta y, \Delta z$	mesh spacings
μ	dynamic viscosity
ν	kinematic viscosity
ρ	density
σ	conductivity
τ	shear stress
τ_{ij}	sub-grid scale stress tensor
ϕ	electric potential field or scalar
Ω	domain
$\partial\Omega$	boundary of Ω

Subscripts

$face$	face of control volume
i, j, k	cell indices or tensor indices
rms	root mean square
R	real size caster
S	scaled caster
s	sub-grid scale
$x+, y+, z+$	x-face, y-face and z-face located at maximum value of x,y and z respectively in a given control volume
$x-, y-, z-$	x-face, y-face and z-face located at minimum value of x,y and z respectively in a given control volume
e,w,n,s,l,h,p	compass directions to identify the values of variables on faces of a given control volume or centers of neighbours control volume

Superscripts

n	time level
$'$	fluctuating quantity
$\widehat{()}$	provisional quantity
$\overline{()}$	time-averaged quantity
$\widetilde{()}$	filtered quantity
$\lvert\,\rvert$	magnitude of a vector or tensor

CHAPTER 1- MOTIVATION AND INTRODUCTION

Steel is considered to be the backbone of the economic development of any country. With abundant iron ore and coal supplies, American industrial growth has been perpetually supported by the steel production as it provides for the infrastructure development of transport: road and railways, power: production and transmission, military and most other industries. The steel manufacturing process has undergone continuous improvements for at least 150 years and today it has evolved into a highly sophisticated process.

Figure 1.1 shows the flow chart of the steel making process. The iron ore is reduced to iron which is then converted to steel. The final step, after some purification processes, is the casting of the steel. The continuous casting of steel process is the most important method of steel casting and was responsible 97.8% (approximately 84.5 million tonnes) of the total steel production in North America; and 95% (approximately 1432.1 million tonnes) of the total steel produce in the world for the year 2011 [1].

1.1 Continuous Casting of Steel

This method, as the name suggests, produces cast slab steel continuously. Although continuous casting of steel is capital intensive, the low operating cost has made it popular for mass production of semi-finished steel. Figure 1.2 shows the schematic of the entire process of curved continuous casting [2]. There are other continuous casting methods, such as vertical continuous casting which is mostly used for casting aluminium, however steel is mostly cast using the curved continuous casting method. Refined and processed molten steel is continuously supplied to the tundish through the ladle which is replaced with a freshly prepared full ladle after the previous one is completely drained. The tundish continuously supplies molten steel to the mold, via the submerged entry nozzle (SEN), even when the ladle

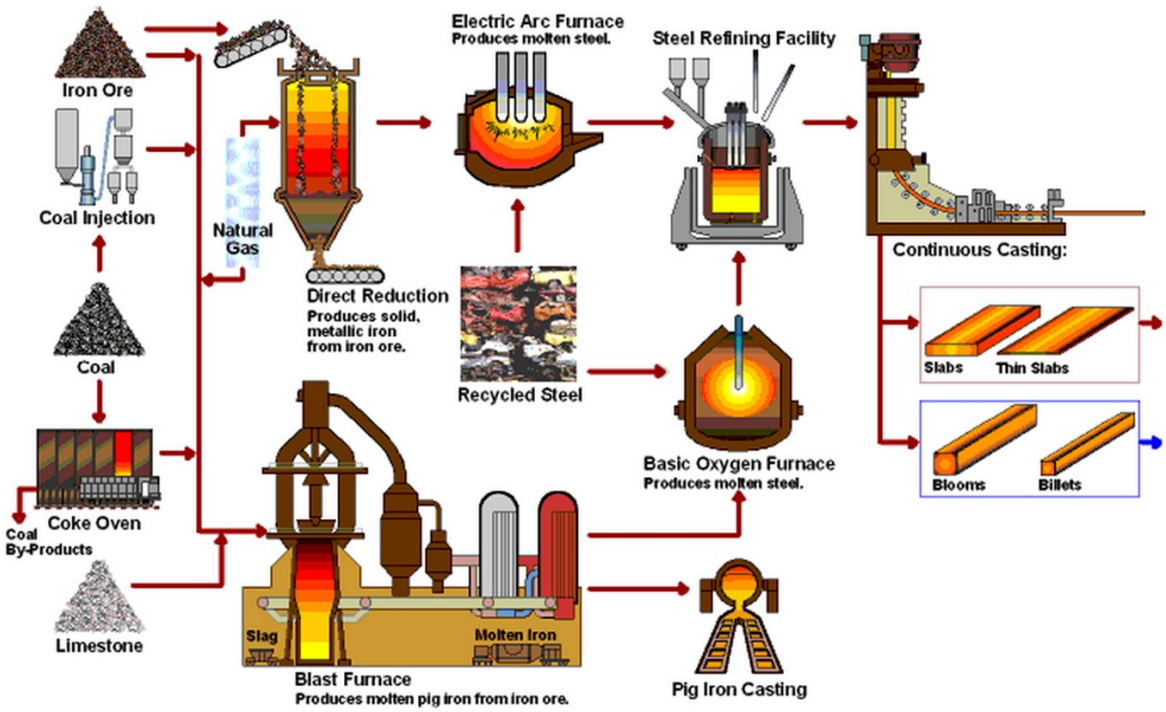

Figure 1.1 Schematic of the iron and steel making process [2]

is being replaced. Solidification starts on the mold walls and the steel shell grows as it moves along the casting direction. The shell with liquid steel exiting the mold needs to be supported in order to avoid bulging due to the ferrostatic pressure. Thus a set of soft rolls are provided to support the solidifying slab till its metallurgical length, which is defined as the length after which the steel completely solidifies in the continuous casting process [3]. The curved strand is then straightened by a set of successive rolls after which the slabs are cut, by the cut-off torch, according to slab specifications.

Figure 1.2 and Figure 1.3 show the tundish and mold assembly; and the detailed view of the mold region respectively. A layer of slag covers the free surfaces in both the tundish and the mold in order to protect the steel from being exposed to air. These layers also help in capturing inclusions which are advected by the flow and also driven by the buoyant forces. The mold region is a critical stage in the continuous casting process. It contains a complex turbulent flow, as two bifurcated jets impinge on the narrow faces and recirculate in a high

aspect ratio geometry, with large velocities. The mold flow if optimized can help reduce defects and remove inclusions present from previous stages. On the other hand non-optimized flow patterns can result in more surface defects, slag entrainment and other steel quality problems. The flow at the top surface of the mold can result in hook formation if the velocities are not sufficiently large. However, if the surface velocities are very large, turbulence and shear instabilities can entrain slag from the top surface. If the surface level fluctuates, the defects can be caused intermittently. Thus tailoring of the mold flow provides an opportunity to improve the steel quality.

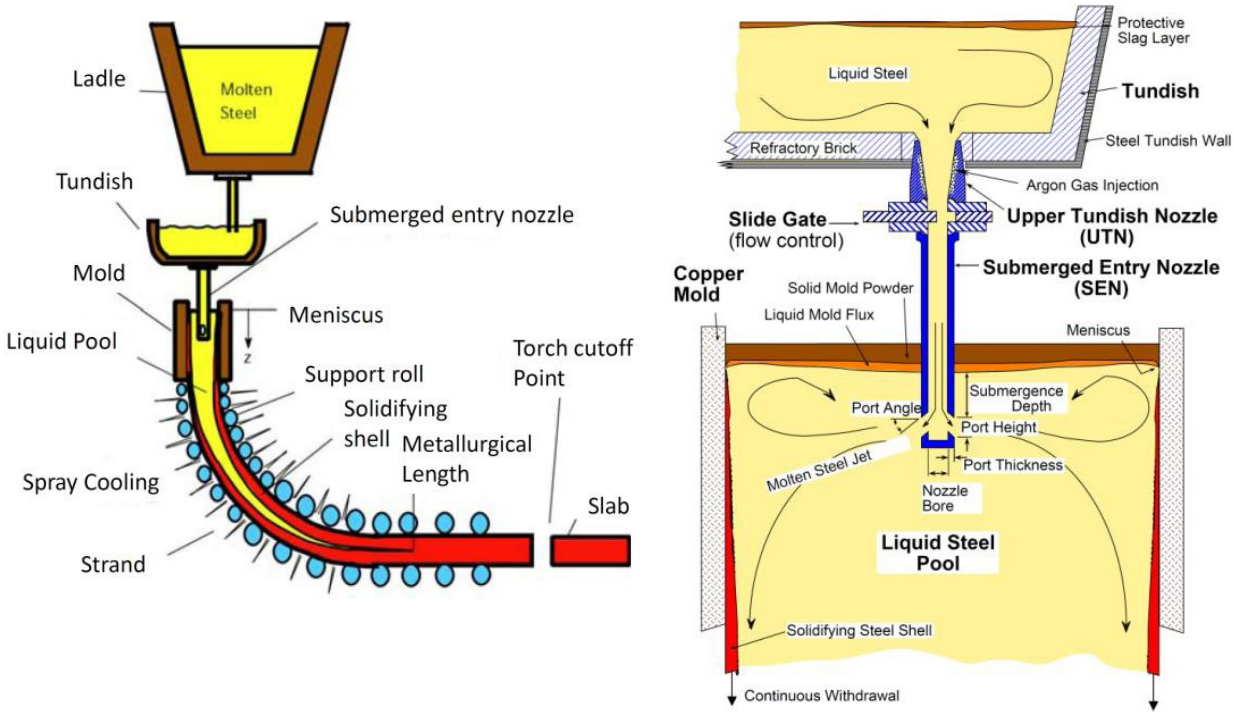

Figure 1.2 Schematic of the (a) continuous casting process (b) tundish and mold region [4]

Mold flow can be controlled to achieve an optimal flow behavior by adjusting geometry: mold cross-section, Submerged Entry Nozzle (SEN) design and type, submergence depth of the SEN; operating parameters: casting speed, slag properties, cooling rate, alloying elements; and by applying external control mechanisms such as argon gas injection and application of magnetic fields. Understanding the effects of each parameter on the flow

behavior and subsequent changes in quality is non-trivial. Also the interplay between each factor is really important in this system.

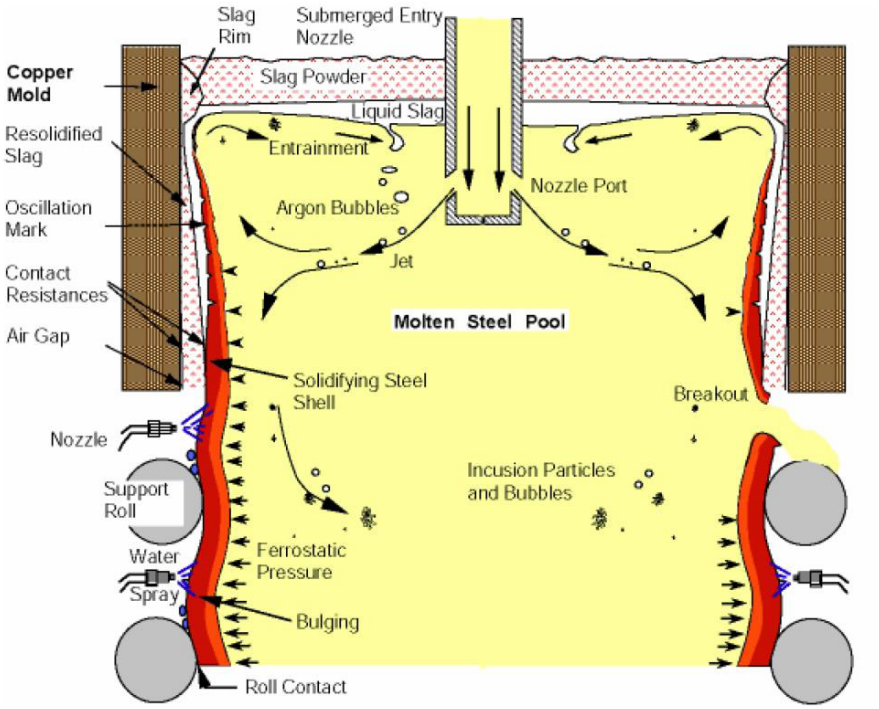

Figure 1.3 Detailed view of the mold region [4]

The application of a magnetic field is an attractive method to control mold flow because it is nonintrusive and can be adjusted during operation. The principle behind this mold flow control method is that the movement of a conducting material, such as steel, under the influence of a magnetic field produces a force opposing the motion and thus are also known as Electromagnetic Brakes (EMBr). This suggests that the coupled fluid flow and the forces produced should result in a self-stabilizing flow system. However, the application of a magnetic field can change the flow pattern in non-obvious ways [5,6] which makes the understanding of the effects even more difficult. In a continuous caster mold the magnetic field configurations are classified based on the type of source and distribution of the field. The classification is broadly based on the use of static magnetic fields using DC current for the electromagnets, or moving fields using AC current. Static applied magnetic fields are

further classified as local, ruler and double ruler or Flow-Control (FC) mold as shown in Figure 1.4.a to Figure 1.4.c respectively. The common feature among all three static-field configurations is that the applied magnetic field has only one non-zero component which is normal to the wide face of the mold. Local EMBr fields have high strength of applied magnetic field confined to two regions which are adjacent to the port exits braking the high velocity jets and the fields are in opposite directions as indicated in the figure. Ruler EMBr configuration can be described as a single band of strong field spanning across the width of the mold and the double ruler configuration has two rulers with opposite magnetic field orientations. The single ruler configuration deflects the jets upwards, if placed over or below the nozzle ports, which may decrease penetration depth of the inclusions and also alter surface flow behavior [5]. FC mold configuration provides more control as the surface velocities and the jet regions can be controlled independently. Moving field configurations (Figure 1.4.d) using AC currents are classified based on the different modes of operation. Electromagnetic level stabilizer (EMLS) and electromagnetic level accelerator (EMLA) are used to decelerate and accelerate the flow respectively. Electromagnetic stirring (EMS) mode is used to induce rotational flow in the mold. Moving field systems add more control parameters and flexibility, which also adds to the challenge of optimizing the system.

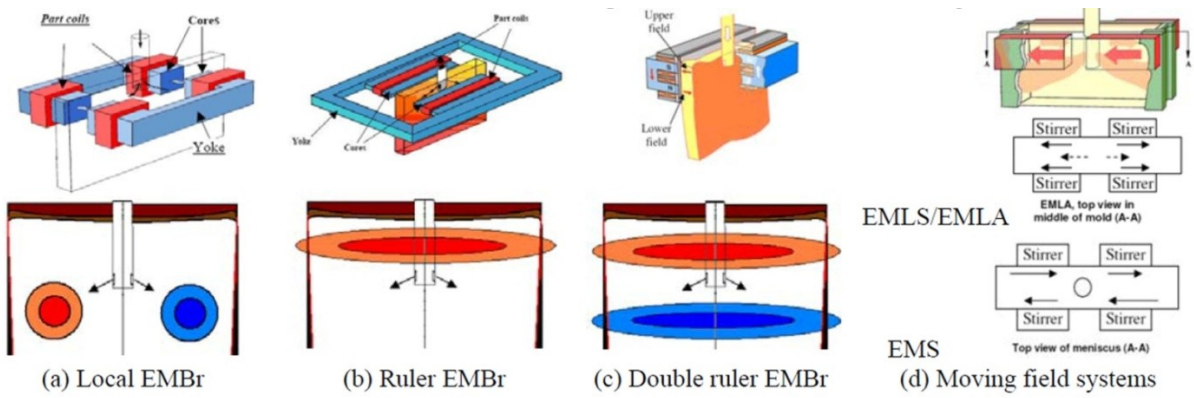

Figure 1.4 Various types of electromagnetic flow-control configurations with hardware setup (top) and schematic of the applied magnetic field (bottom) [7]

The work presented in this thesis focuses on developing a model to numerically study and understand the highly transient process of mold flow including the effects of various EMBr configurations. As the transient behavior and flow stability is more important to mold flow quality [8], Large Eddy Simulations (LES) of the mold flow were performed in the study to resolve the extreme unsteadiness of the flow in detail. Details of the governing equations for LES and the numerical method for solving these equations are presented in Chapter 2. Chapter 3 discusses the model validation with instantaneous and time-averaged measurements in scaled caster with liquid metal [9,10,11]. The model then was used to study the corresponding real size caster. The important effect of the current flow through the conducting solid steel shell on stabilizing the fluid flow pattern is investigated. The transient behavior of the mold flow reveals the effects of EMBr on stability of the jet, top surface velocities, surface profile and level fluctuations. Scaling criteria were also evaluated in the presence of applied magnetic fields. In the absence of any applied magnetic field, caster model operating conditions are scaled to match flow pattern and free surface behavior by maintaining only the Froude number, which is the ratio between the inertial and gravitational forces. However in the presence of a magnetic field the Stuart number, which is the ratio between electromagnetic and inertial forces, is crucial as well. Sometimes maintaining both, the Froude number and the Stuart number, in a physical model simultaneously is difficult as it might pose difficulties due to the need of having too high or too low velocities and high applied magnetic field strength. In the present study effect of maintaining only the Stuart number scaling criterion was evaluated.

This work has been published at "Metallurgical and Materials Transactions B" :

R. Singh, B.G. Thomas and S.P. Vanka, "Effects of a magnetic field on turbulent flow in the mold region of a steel caster", *Metallurgical and Materials Transactions B,* pp.1-21, May 2013.

Chapter 4 presents the results from large eddy simulations of a real industrial caster at industrial operating conditions. The caster geometry and operating conditions were taken from a commercial steel caster. This caster has argon gas injection but the simulations were performed assuming single phase flow. Two cases were studied for the real caster: first without any applied magnetic fields same as the commercial caster and the second with a FC-Mold EMBr configuration, which is mostly used in the industry. The effects of this FC-Mold EMBr configuration on the transient and time-averaged behavior of the flow pattern, surface level profile, surface level fluctuations and surface velocities, were studied, with and without the applied magnetic field. The calculated results, for the case without EMBr, were also compared to the nail board measurements taken at the commercial caster.

1.2 CFD on Graphics Processing Units (GPUs)

Graphics processing units are different from conventional CPUs with regards to the architecture. CPUs rely on multicore processors for parallel computing, whereas a GPU is a multi-core multi-thread multiprocessor which focuses on throughput of parallel applications [12]. Traditionally GPUs were used for rendering images and graphics on computers; however over the last 10 years the architecture has evolved to support scientific computing. The computational capability has increased many times and Figure 1.5 compares the improvement in peak performance of GPUs and CPUs over the last decade. The GPU performance is memory-access-latency bound. Thus the algorithms that can derive the most computational efficiency are explicit where only the neighbour values are needed. Implicit algorithms, such as line-inversion, have more recursive relations which inhibit the performance [13]. Some advanced algorithms make use of implicit algorithms on GPUs computationally feasible but are extremely code intensive.

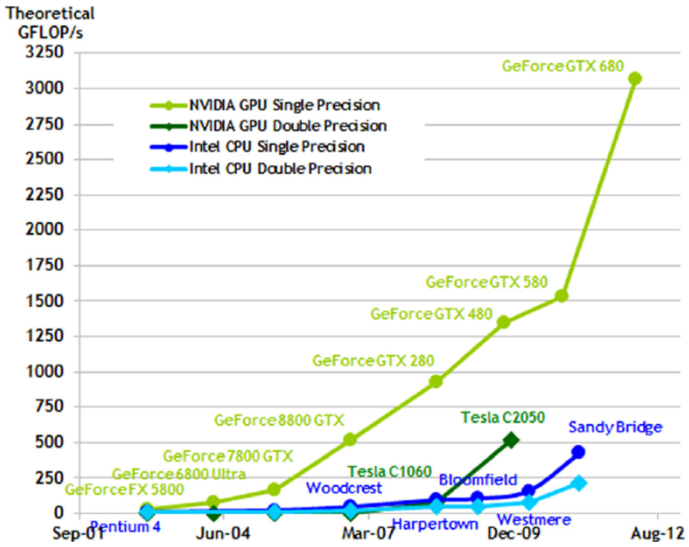

Figure 1.5 Comparison of computing power of CPUs and GPUs over the last decade [14]

Figure 1.6 shows the architecture of the NVIDIA Fermi family of GPUs. The GPU building blocks are the streaming multiprocessor (SMs) which are shown in the figure as vertical rectangular strips. Each of these SMs (Figure 1.7) has a number of streaming processors (SPs) or CUDA cores. The number of SMs and SPs per SM may vary with the generation of the GPU. The SPs are massively threaded and can run thousands of threads depending upon the need of the application. To clearly establish the difference between a CPU and a GPU, consider a simple example of matrix addition. Two arrays, A and B, with a hundred elements in each were to be added to produce C. In a CPU a single thread would do the addition sequentially, starting from the first element of each array proceeding one by one till the completion of the task. However a GPU would release a hundred threads and process each of the summation operations simultaneously. NVIDIA Tesla® C2075, which has 14 SMs with 32 SPs in each SM, is used in the present study. The other attractive feature in the C2075 is the 6GB of on-board memory which facilitates processing of bigger computational meshes for more accurate simulations.

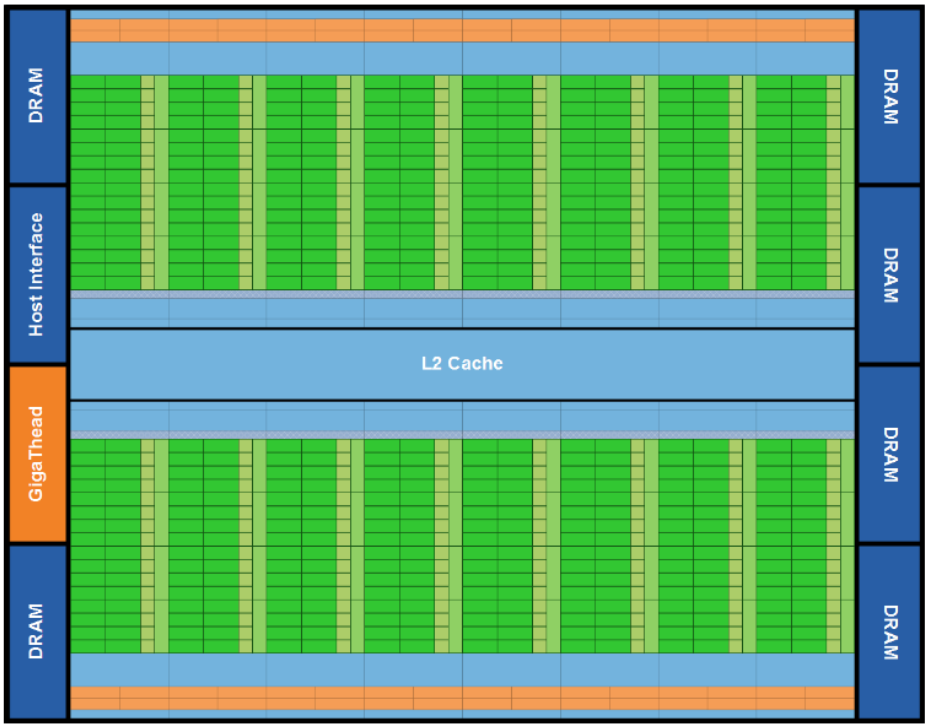

Figure 1.6 Schematic of the NVIDIA Fermi® architecture [15]

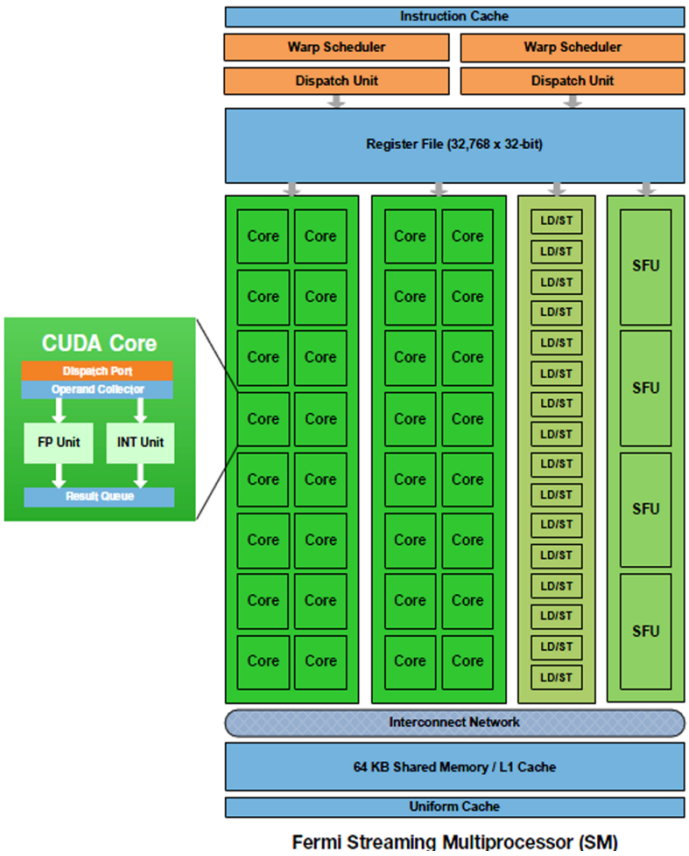

Figure 1.7 Schematic of a streaming multiprocessor (SM) of the NVIDIA Fermi® architecture [15]

1.3 References

1. "World steel in figures 2012", *World Steel Association*, Brussels, Belgium, 2012.
2. American Iron and Steel Institute, Steel Works- The online resource for steel, http://www.steel.org/en/ .
3. B.G. Thomas, "Continuous Casting", *Yearbook of Science and Technology*, McGraw-Hill, 2004.
4. Continuous Casting Consortium, Department of Mechanical Science & Engineering, University of Illinois at Urbana-Champaign, IL, USA, http://ccc.illinois.edu/.
5. R. Chaudhary, B. G. Thomas, and S. P. Vanka, "Effect of Electromagnetic Ruler Braking (EMBr) on transient turbulent flow in continuous slab casting using large eddy simulations", *Metallurgical and Materials Transactions B*, 2012, vol. 43, pp. 532-553.
6. C. Zhang, S. Eckert, and G. Gerbeth, "The flow structure of a bubble-driven liquid-metal jet in a horizontal magnetic field", *Journal of Fluid Mechanics*, 2012, vol. 575, pp. 57-82.
7. B.G. Thomas and R. Chaudhary, "State of the art in electromagnetic flow control in continuous casting of steel slabs: modeling and plant validation", *in 6th International Conference on Electromagnetic Processing of Materials EPM*, Oct 19-23, 2009, Dresden, Germany.
8. P.H. Dauby, "Continuous casting: make better steel and more of it!", *International Journal of Metallurgy*, 2012, vol. 109, pp. 113-136.
9. K. Timmel, X. Miao, S. Eckert, D. Lucas, and G. Gerbeth, "Experimental and numerical modeling of the steel flow in a continuous casting mold under the influence of a transverse DC magnetic field", *Magnetohydrodynamics*, 2010, vol. 46, pp. 437-448.

10. K. Timmel, S. Eckert, and G. Gerbeth, “Experimental investigation of the flow in a continuous-casting mold under the influence of a transverse, direct current magnetic field”, *Metallurgical and Materials Transactions B*, 2011, vol. 42, pp. 68-80.
11. X. Miao, K. Timmel, D. Lucas, S. Ren, Z.and Eckert, and G. Gerbeth, “Effect of an electromagnetic brake on the turbulent melt flow in a continuous-casting mold”, *Metallurgical and Materials Transactions B*, 2012, vol. 43, pp. 954-972.
12. D.B. Kirk and W.W. Hwu, “Programming a massively parallel processor- A hands on approach”, Elsevier Inc., 2010.
13. S.P. Vanka, “2012 Freeman Scholar Lecture: Computational Fluid Dynamics on Graphics Processing Units”, *Journal of Fluids Engineering*, 2013, vol. 135, pp. 061401.
14. “Products & Technologies,” AMD, http:/www.amd.com/us/products.
15. “NVIDIA’s Next Generation CUDA™ Compute Architecture: Fermi™”, NVIDIA, http://www.nvidia.com/content/PDF/fermi_white_papers.

CHAPTER 2 -GOVERNING EQUATIONS AND NUMERICAL METHODOLOGY

2.1 Governing Equations

2.1.1 Fluid Flow Equations

The fluid flow equations solved in the current work are the mass conservation equation and the unsteady momentum equation which are given by Equations 2.1 and 2.2 respectively. These equations are presented in indicial notations as this representation is convenient in the context of the present study.

$$\frac{\partial u_j}{\partial x_j} = 0 \tag{2.1}$$

$$\frac{\partial u_i}{\partial t} + \frac{\partial u_i u_j}{\partial x_j} = -\frac{1}{\rho}\frac{\partial p}{\partial x_i} + \frac{\partial}{\partial x_j}\left(\nu \frac{\partial u_i}{\partial x_j}\right) + \frac{1}{\rho}F_i \qquad i = 1,2,3 \tag{2.2}$$

Here *i,j* represent the indices of the respective vectors, u_i represents the ith component of the velocity vector, ρ is the density, p is the pressure, ν is the kinematic viscosity of the fluid and F_i represents the ith component of the body force.

2.1.2 Magnetohydrodynamic (MHD) Equations

The present study requires the solution of the coupled magnetohyrodynamic and fluid flow equations. The coupling happens via the induced body force which is known as the Lorentz force. The molten steel flowing through the magnetic field generates an electric current ($\boldsymbol{J}$) and is calculated using Equation 2.3.

$$\boldsymbol{J} = \sigma(\boldsymbol{E} + \boldsymbol{u} \times \boldsymbol{B_0}) = \sigma(-\boldsymbol{\nabla}\phi + \boldsymbol{u} \times \boldsymbol{B_0}) \tag{2.3}$$

Here, σ is electrical conductivity, $\boldsymbol{E}$ is induced electric field, ϕ is electric potential and $\boldsymbol{B_0}$ is the applied magnetic field. Now as the induced current is a solenoidal vector field its divergence should be zero. This condition is better known as the current conservation equation and can be written as

$$\boldsymbol{\nabla} \cdot \boldsymbol{J} = 0 \tag{2.4}$$

By taking the divergence of Equation 2.3 and applying the current conservation equation we get a Poisson equation for electric potential field, known as the Electric Poisson Equation (EPE), which can be written as

$$\boldsymbol{\nabla} \cdot (\sigma \boldsymbol{\nabla} \phi) = \boldsymbol{\nabla} \cdot \big(\sigma(\boldsymbol{u} \times \boldsymbol{B_0})\big) \tag{2.5}$$

where the electrical conductivities could be cancelled from both sides of the equation if assumed to be uniform. However, in the current study systems with spatially-variable conductivities were solved.

Finally, the Lorentz force $(\vec{F})$ is calculated by taking the cross product of the induced current and the applied magnetic field as shown in Equation 2.6.

$$\boldsymbol{F} = \boldsymbol{J} \times \boldsymbol{B_0} \tag{2.6}$$

2.2 Governing Equations for Large-Eddy Simulations (LES)

As the Reynolds number of a turbulent flow increases, the scale separation between the large energy containing eddies and the Kolmogorov scales widens. Due to the computational limitations resolving all scales for high Reynolds number flows, such as the steel flow in the mold (Re ~ $O[10^5]$), is not feasible. In LES the equations are solved numerically only for the large scales, starting from the largest to a lower threshold, and the effects of all scales below the lower threshold on the larger flow scales are modeled.

LES equations are derived by applying a filtering operation to the governing equations, which decomposes the velocity field $\boldsymbol{u}$ into a filtered velocity $\widetilde{\boldsymbol{u}}$ and residual velocity $\boldsymbol{u}'$.

$$\boldsymbol{u} = \widetilde{\boldsymbol{u}} + \boldsymbol{u}' \tag{2.7}$$

The filtering operation is achieved by using an integral over the entire domain (Ω).

$$\widetilde{\boldsymbol{u}}(\boldsymbol{x}) = \int_{\Omega} G(\boldsymbol{x}, \boldsymbol{x}')\boldsymbol{u}(\boldsymbol{x}')dx_1'dx_2'dx_3' \tag{2.8}$$

where G is the filter function and $\boldsymbol{x}, \boldsymbol{x}'$ are position vectors. In the present study implicit filtering is performed, so the computational mesh cells act as the spatial filter and any scale smaller than the mesh size is filtered.

Apply the filtering operation to fluid flow equations, Equations 2.1 and 2.2, produces

$$\frac{\partial \widetilde{u}_j}{\partial x_j} = 0 \tag{2.9}$$

$$\frac{\partial \widetilde{u}_i}{\partial t} + \frac{\partial \widetilde{u_i u_j}}{\partial x_j} = -\frac{1}{\rho}\frac{\partial \widetilde{p}}{\partial x_i} + \frac{\partial}{\partial x_j}\left(\nu \frac{\partial \widetilde{u}_i}{\partial x_j}\right) + \frac{1}{\rho}F_i \tag{2.10}$$

The filtering of the non-linear term produces $\widetilde{u_i u_j}$ which cannot be calculated as it requires knowledge of the unfiltered velocity field. This illustrates the difficulty in scale separation as the small scales and the large scales interact. In order to split the non-linear term, Leonard [1] defined a sub-grid scale tensor as

$$\tau_{ij} = \widetilde{u_i u_j} - \widetilde{u}_i \widetilde{u}_j \tag{2.11}$$

Substituting this into the filtered momentum equation produces

$$\frac{\partial \widetilde{u}_i}{\partial t} + \frac{\partial \widetilde{u}_i \widetilde{u}_j}{\partial x_j} = -\frac{1}{\rho}\frac{\partial \widetilde{p}}{\partial x_i} + \frac{\partial}{\partial x_j}\left(\nu \frac{\partial \widetilde{u}_i}{\partial x_j}\right) + \frac{1}{\rho}F_i - \frac{\partial \tau_{ij}}{\partial x_j} \tag{2.12}$$

The last term needs to be modelled which is done using the linear eddy viscosity model as shown in Equation 2.13.

$$\tau_{ij} - (1/3)\delta_{ij}\tau_{kk} = -2\nu_s\widetilde{S_{ij}} \tag{2.13}$$

where ν_s is the sub-grid scale or eddy viscosity and $\widetilde{S_{ij}}$ is the filtered rate-of-strain tensor defined in Equation 2.14.

$$\widetilde{S_{ij}} = \frac{1}{2}\left(\frac{\partial \widetilde{u_i}}{\partial x_j} + \frac{\partial \widetilde{u_j}}{\partial x_i}\right) \tag{2.14}$$

The sub-grid scale tensor in Equation 2.12 is substituted with the definition provided by the eddy viscosity model (Equation 2.13). The isotropic part of the sub-grid scale tensor is added to the pressure to give the modified pressure $\tilde{p}^* = \tilde{p} + (1/3)\delta_{ij}\tau_{kk}$. Thus the derived filtered momentum equation is

$$\frac{\partial \widetilde{u_i}}{\partial t} + \frac{\partial \widetilde{u_i}\widetilde{u_j}}{\partial x_j} = -\frac{1}{\rho}\frac{\partial \tilde{p}^*}{\partial x_i} + \frac{\partial}{\partial x_j}\left(\nu\frac{\partial \widetilde{u_i}}{\partial x_j}\right) + \frac{1}{\rho}F_i + \frac{\partial}{\partial x_j}\left(\nu_s\left(\frac{\partial \widetilde{u_i}}{\partial x_j} + \frac{\partial \widetilde{u_j}}{\partial x_i}\right)\right) \tag{2.15}$$

This equation is further simplified by using the incompressibility condition and by neglecting the non-uniform eddy viscosity term as it is usually small. This gives the final form of the filtered momentum equation as

$$\frac{\partial \widetilde{u_i}}{\partial t} + \frac{\partial \widetilde{u_i}\widetilde{u_j}}{\partial x_j} = -\frac{1}{\rho}\frac{\partial \tilde{p}^*}{\partial x_i} + \frac{\partial}{\partial x_j}\left((\nu + \nu_s)\frac{\partial \widetilde{u_i}}{\partial x_j}\right) + \frac{1}{\rho}F_i \tag{2.16}$$

2.2.1 Models for Sub-grid Scale Viscosity (ν_s)

The effects of the turbulent flow scales too small to be captured by the computational grid are incorporated by SGS models. With increase in grid refinement, the contribution of the SGS model diminishes such that the modeled eddy viscosity tends to zero as the refinement nears

the requirements of a Direct Numerical Simulation (DNS) in which all flow scales are resolved. One of the earliest and the simplest of the SGS models is the Smagorinsky model [2] in which the subgrid scale eddy viscosity is calculated as

$$\nu_s = (C_s\Delta)^2|\bar{S}| \tag{2.17}$$

Where C_s is the Smagorinsky constant, $\Delta = (\Delta x_i \Delta y_j \Delta z_k)^{1/3}$ is the local filter width of individual mesh cells and $|\bar{S}|$ is the magnitude to the filtered rate-of-strain tensor $\widetilde{S_{ij}}$ as shown in Equation 2.14. For the sake of simplicity the filter sign ~ will be neglected beyond this point in this text as all LES equations discussed will consider only filtered quantities.

$$|\bar{S}| = \sqrt{2S_{ij}S_{ij}} \tag{2.18}$$

This model is computationally inexpensive but has some drawbacks. The eddy viscosity should ideally reduce to zero close to the wall but this model produces non-zero values. Thus additional near-wall scaling laws are required, such as the Van Driest damping which still does not accurately produce the $O(y^3)$ scaling of the eddy viscosity close to the walls.

In the present study two variants of the Samgorinsky SGS models were used:

2.2.1.1 Wall Adapting Local Eddy-viscosity (WALE) model

The WALE model [3] calculates the eddy viscosity with appropriate scaling to ensure a near zero value close to the walls ($O(y^3)$). This is a favorable feature for studies involving confined flows. The eddy viscosity is calculated as

$$\nu_s = L_s^2 \frac{\left(S_{ij}^d S_{ij}^d\right)^{3/2}}{\left(S_{ij}S_{ij}\right)^{5/2} + \left(S_{ij}^d S_{ij}^d\right)^{5/4}} \tag{2.19}$$

where, $S_{ij}^{d} = \frac{1}{2}\left(g_{ij}^{2} + g_{ji}^{2}\right) - \frac{1}{3}\delta_{ij}g_{kk}^{2}$, $g_{ij} = \frac{\partial u_i}{\partial x_j}$, $L_s = C_w(\Delta x \Delta y \Delta z)^{1/3}$, $C_w^2 = 10.6C_s^2$, $C_s = 0.18$, and Δx, Δy and Δz are grid spacing in x, y and z directions respectively.

2.2.1.2 Coherent-structure Smagorinsky Model (CSM)

The CSM SGS model [4] dynamically calculates the model parameter (C) and has been shown to accurately predict the relaminarization of a turbulent flow subjected to a strong magnetic field. The CSM model incorporates the anisotropic effects of the applied magnetic field and also damps the eddy viscosity close to the wall by dynamically calculating the model constant. The model constant is calculated using a coherent structure function ($\mathcal{F}_{CS}$) as shown in Equations 2.20 to 2.23.

$$C_s^2 = C = C_{CSM}|\mathcal{F}_{CS}|^{3/2}\mathcal{F}_{\omega} \tag{2.20}$$

$$C_{CSM} = \frac{1}{22}, \qquad \mathcal{F}_{CS} = \frac{Q}{E}, \qquad \mathcal{F}_{\omega} = 1 - \mathcal{F}_{CS} \tag{2.21}$$

$$W_{ij} = \frac{1}{2}\left(\frac{\partial u_j}{\partial x_i} - \frac{\partial u_i}{\partial x_j}\right) \tag{2.22}$$

$$Q = \frac{1}{2}\left(W_{ij}W_{ij} - S_{ij}S_{ij}\right) \qquad E = \frac{1}{2}\left(W_{ij}W_{ij} + S_{ij}S_{ij}\right) \tag{2.23}$$

2.3 Numerical Solution of the Governing Equations

The equations are solved using a in-house developed model, CUFLOW. This flagship model has been previously applied to study various canonical flows with and without applied magnetic fields [5-8]. This code uses a fractional step method for the pressure-velocity coupling and the Adams Bashforth temporal scheme and second order finite volume method for discretizing the momentum equations on a Cartesian grid. Figure 2.1 shows the flowchart of the steps involved in the CUFLOW solver. In the fractional step method, the momentum

equations are first solved to give the intermediate or provisional velocity $\hat{\boldsymbol{u}}$ without considering the effect of the pressure gradient term as shown for all three directions in Equations 2.24, 2.27 and 2.30.

x-momentum equation:

$$\frac{\hat{u} - u^n}{\Delta t} = \frac{3}{2} H_u^n - \frac{1}{2} H_u^{n-1} + \frac{1}{\rho} F_u^n \tag{2.24}$$

$$H_u^n = \left[-\left(\frac{\partial uu}{\partial x} + \frac{\partial uv}{\partial y} + \frac{\partial uw}{\partial z} \right) + (\nu + \nu_s) \left(\frac{\partial^2 u}{\partial x^2} + \frac{\partial^2 u}{\partial y^2} + \frac{\partial^2 u}{\partial z^2} \right) \right]^n \tag{2.25}$$

$$\frac{u^{n+1} - \hat{u}}{\Delta t} = -\frac{1}{\rho} \frac{\partial p^{n+1}}{\partial \mathrm{x}} \tag{2.26}$$

y-momentum equation:

$$\frac{\hat{v} - v^n}{\Delta t} = \frac{3}{2} H_v^n - \frac{1}{2} H_v^{n-1} + \frac{1}{\rho} F_v^n \tag{2.27}$$

$$H_v^n = \left[-\left(\frac{\partial vu}{\partial x} + \frac{\partial vv}{\partial y} + \frac{\partial vw}{\partial z} \right) + (\nu + \nu_s) \left(\frac{\partial^2 v}{\partial x^2} + \frac{\partial^2 v}{\partial y^2} + \frac{\partial^2 v}{\partial z^2} \right) \right]^n \tag{2.28}$$

$$\frac{v^{n+1} - \hat{v}}{\Delta t} = -\frac{1}{\rho} \frac{\partial p^{n+1}}{\partial \mathrm{y}} \tag{2.29}$$

z-momentum equation:

$$\frac{\hat{w} - w^n}{\Delta t} = \frac{3}{2} H_w^n - \frac{1}{2} H_w^{n-1} + \frac{1}{\rho} F_w^n \tag{2.30}$$

$$H_w^n = \left[-\left(\frac{\partial wu}{\partial x} + \frac{\partial wv}{\partial y} + \frac{\partial ww}{\partial z} \right) + (\nu + \nu_s) \left(\frac{\partial^2 w}{\partial x^2} + \frac{\partial^2 w}{\partial y^2} + \frac{\partial^2 w}{\partial z^2} \right) \right]^n \tag{2.31}$$

$$\frac{w^{n+1} - \hat{w}}{\Delta t} = -\frac{1}{\rho} \frac{\partial p^{n+1}}{\partial \mathrm{z}} \tag{2.32}$$

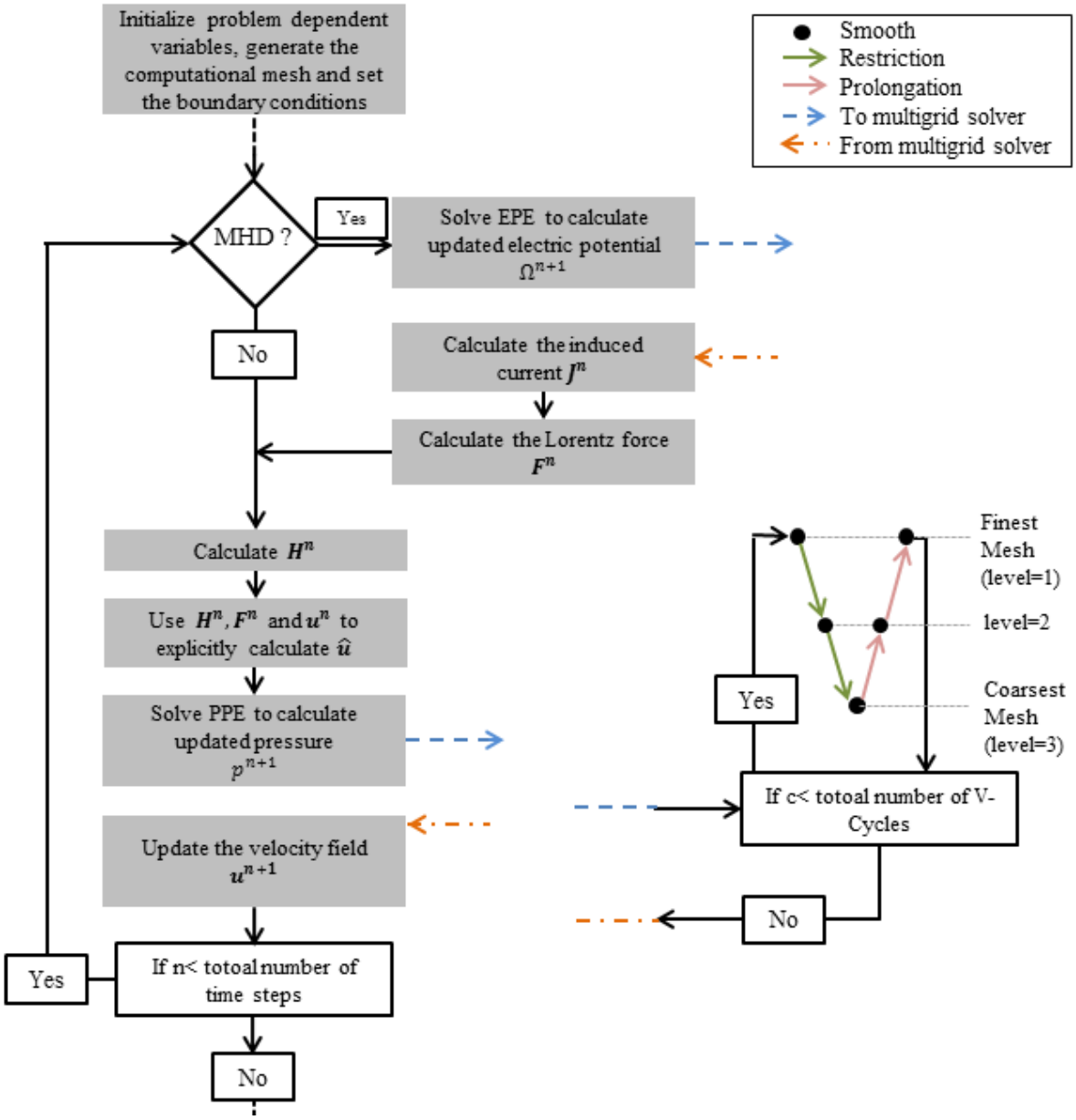

Figure 2.1: Flowchart of the numerical method implemented in CUFLOW for solving the governing equations

This provisional velocity calculated is not divergence free as the pressure gradient term is not considered in its calculation. Taking the divergence of the sum of the Equations 2.26, 2.29 and 2.32, and applying the discrete continuity equation ($\nabla \cdot \boldsymbol{u}^{n+1} = 0$) results in a pressure Poisson equation (PPE) which is solved to update the pressure field.

$$\frac{\partial}{\partial x}\left(\frac{\partial p^{n+1}}{\partial \mathrm{x}}\right)+\frac{\partial}{\partial y}\left(\frac{\partial p^{n+1}}{\partial \mathrm{y}}\right)+\frac{\partial}{\partial z}\left(\frac{\partial p^{n+1}}{\partial \mathrm{z}}\right)=\frac{\rho}{\Delta t}\left(\frac{\partial \hat{\mathrm{u}}}{\partial \mathrm{x}}+\frac{\partial \hat{\mathrm{v}}}{\partial \mathrm{y}}+\frac{\partial \hat{\mathrm{w}}}{\partial \mathrm{z}}\right) \tag{2.33}$$

Now the divergence free velocity field $\boldsymbol{u}^{\boldsymbol{n+1}}$ can be calculated by using the updated pressure in 2.26, 2.29 and 2.32.

If MHD equations are being solved, the electric Poisson equation (EPE, Equation 2.5) is solved prior to the PPE as this requires the provisional velocity $\hat{\boldsymbol{u}}$ which depends on the updated Lorentz force. The solution of the EPE gives the updated electric potential field ϕ^{n+1}. The induced current is then calculated, with the updated electric potential field, using Equation 2.3. The Lorentz force is calculated as shown in Equation 2.6 which is then added as a source term to the momentum equations and solved as discussed earlier.

The solutions of the two Poisson equations, pressure Poisson Equation and electric Poisson equation, are the computationally most expensive steps in the model (both responsible for approximately 4/5th of the total computational time together). To accelerate the convergence of the Poisson equations a geometric multigrid technique is employed with red-black Gauss-Seidel and Successive Over-Relaxation (SOR) to smooth the errors on each grid level. A V-cycle (Figure 2.1) is used, for the multi-grid solver, where the residuals are restricted to the successive coarser level till the coarsest grid, relaxed and the corrections prolonged to the finer levels until the finest level.

The spatial discretization of the source terms in momentum equations and the pressure Poisson equation (PPE) have been discussed in detail in Reference [8]. The spatial discretization of the electric Poisson Equation (EPE) is discussed in APPENDIX A.

2.4 References

1. A. Leonard, "Energy cascade in large-eddy simulations of turbulent fluid flows", *Advances in Geophysics,* 1974, vol. 18, pp. 237-248.
2. J. Smagorinsky, “General circulation experiments with the primitive equations”, *Annual Weather Review*, 1963, vol. 96, pp. 99-164.
3. F. Nicoud and F. Ducros, “Subgrid-scale stress modelling based on the square of the velocity gradient tensor”, *Flow, Turbulence and Combustion*, 1999, vol. 62, pp. 183-200.
4. H. Kobayashi, “Large eddy simulation of magnetohydrodynamic turbulent channel flows with local subgrid-scale model based on coherent structures”, *Physics of Fluids*, 2006, vol. 18, pp. 045107.
5. R. Chaudhary, S. P. Vanka, and B. G. Thomas, “Direct numerical simulations of magnetic field effects on turbulent flow in a square duct”, *Physics of Fluids*, 2010, vol. 22, pp. 075102-15.
6. R. Chaudhary, A.F. Shinn, S.P. Vanka, and B.G. Thomas, “Direct numerical simulations of transverse and spanwise magnetic field effects on turbulent flow in a 2:1 aspect ratio rectangular duct”, *Computers & Fluids*, 2011, vol. 51, pp. 100-114.
7. A.F. Shinn and S.P. Vanka, “Large eddy simulations of film-cooling flows with a micro-ramp vortex generator”, *Journal of Turbomachinery*, 2013, vol. 135, pp. 011004-16.
8. A.F. Shinn, “Large eddy simulations of turbulent flows on graphics processing units: application to film-cooling flows”, PhD Thesis, University of Illinois at Urbana-Champaign, 2011.

CHAPTER 3- APPLICATION TO GaInSn MODEL CASTER FOR VALIDATION WITH EXPERIMENTS AND STUDY OF EFFECTS OF THE RULER ELECTROMAGNETIC BRAKING (EMBr)

3.1 Introduction

In Chapter 3 we discuss the motivation for application of the developed computational model, CUFLOW, to the GaInSn scaled model caster and validate the simulated results with measurements. Various cases were studied to understand the effects of a ruler EMBr and also to evaluate scaling criteria in the presence of the applied magnetic fields. As discussed earlier the mechanism to control mold flow with externally applied magnetic fields is very powerful as it intrinsically damps the turbulent fluctuations and can be varied during operation.

Several previous studies have attempted to understand the flow in the mold region under the influence of different static magnetic field configurations such as local [5-9], ruler [3, 9] and Flow-Control(FC) mold [3, 10, 11] configuration. Cukierski et al. [5] observed that application of local EMBr weakens the upper recirculation region and decreases the top surface velocity. Harada et al. [9] compared the effects of local and ruler EMBr systems and claimed that both configurations increase surface velocities and dampen high velocities below the mold, and that configuring the ruler configuration below the nozzle ports has better braking efficiency and also results in better surface stability. Li et al. [10] studied the effect of FC mold and reported that with application of the two magnets, one at the meniscus and the second below the nozzle, plug like flow develops below the mold and the top surface velocities were so low that the meniscus would be prone to freezing.

As it is difficult to make measurements in real casters, due to the high temperatures of the molten steel, physical models with other conducting working fluids, such as mercury [9], tin [10] and eutectic alloys such as GaInSn [12-14], have been used in the past to study the effect of magnetic fields. Numerical studies of the mold flow have been extensively used to

understand the continuous casting process [3, 5, 7, 8, 14-20]. Most of the studies exploring mold flow used Reynolds-averaged Navier-Stokes (RANS) [3, 5, 7, 8, 20, 21] or unsteady RANS (URANS) [14, 16] which compute only the mean flow behavior and model the effects of turbulence through turbulence models. However, transient behavior and flow stability is more important to mold flow quality [22], and has received relatively less attention. Direct Numerical Simulations (DNS) resolve the instantaneous flow accurately but are computationally infeasible at the Reynolds numbers involved in the continuous casting process. On the other hand, Large Eddy Simulations (LES) only model the small scales of turbulence. LES of the mold flow region in continuous casting, without EMBr [16, 23] and with EMBr [3, 17-19], have been performed by a few researchers and were seen to provide a better understanding of the transients involved in the process.

The instantaneous and the mean behaviors of the mold flow are also greatly affected by the electrical conductivity of the solidifying shell [10, 13, 14]. Li et al. [10] showed that the incorporation of accurate wall conductivity is necessary as it affects the braking efficiency of the magnetic field. Timmel et al. [13] performed experiments with GaInSn alloy and concluded that with conducting side walls the mold flow was very stable as opposed to insulated walls with the same magnetic field configuration. Miao et al. [14] conducted URANS simulations of the GaInSn model to study the effects of wall conductivity. However, to our knowledge, there have been no previous studies which performed LES to understand the effects of magnetic fields and wall conductivity on real caster geometries.

In the current work we have studied the mold flow patterns under the influence of applied magnetic fields incorporating the influence of a conducting shell. An in-house computational fluid dynamics code, CUFLOW, was used to perform LES of the MHD flow in the mold region. The CUFLOW code has been previously validated for several canonical flows such as MHD flows in rectangular ducts [24, 25] and also for the GaInSn model with electrically

insulated walls [3]. Numerical methods implemented in CUFLOW have already been discussed in Section 2.3 and are only briefly mentioned in Section 3.2.2. In addition, in the current study we use an additional sub-grid scale (SGS) model, called the Coherent-Structure Model (CSM) proposed by Kobayashi et al. [26], which incorporates the effect of anisotropy induced by the applied magnetic fields on the filtered scales. The SGS models used in this study have already been discussed in Section 2.2.1. The code is first validated by comparing with measurements taken in scaled GaInSn model with conducting brass plates on the wide face walls [13]. These results are presented in Section 3.3.1 and compared with results for the same model by Chaudhary et al. [3] who performed computations assuming insulated walls. The code is then used to study a full-scale real continuous caster of steel under the influence of a magnetic field. Results for the full scale caster, with and without the applied magnetic field, are presented in Section 3.4. The time-averaged and instantaneous flows, Reynolds stresses, turbulent kinetic energy, surface level profiles and surface level fluctuations are computed to study the effects of ruler EMBr on the details of the flow phenomena and similarity criteria for scaleup.

3.2. Computational Model

3.2.1. Computational Domain, Mesh and Boundary Conditions

Two different flow geometries were investigated in this work: a scaled low-melting point liquid-metal (GaInSn) model with a ruler EMBr field, and a corresponding full-scale caster, six-times larger in every dimension. Figure 3.1 gives the geometric details, with dimensions corresponding to the real caster domain, with the sectioned region representing the solidified steel shell on the walls of the real caster mold. The maximum field strength of the ruler EMBr is positioned across the nozzle outlet ports, centered 92-mm below the free surface of the liquid metal in the scale model, and 552mm (= 6*92mm) in the real caster. The variations of the applied magnetic field within the mold for both the GaInSn model and the real caster are

shown in Figure 3.2. Dimensions, process parameters and material properties for both geometries are provided in Table 3.1.

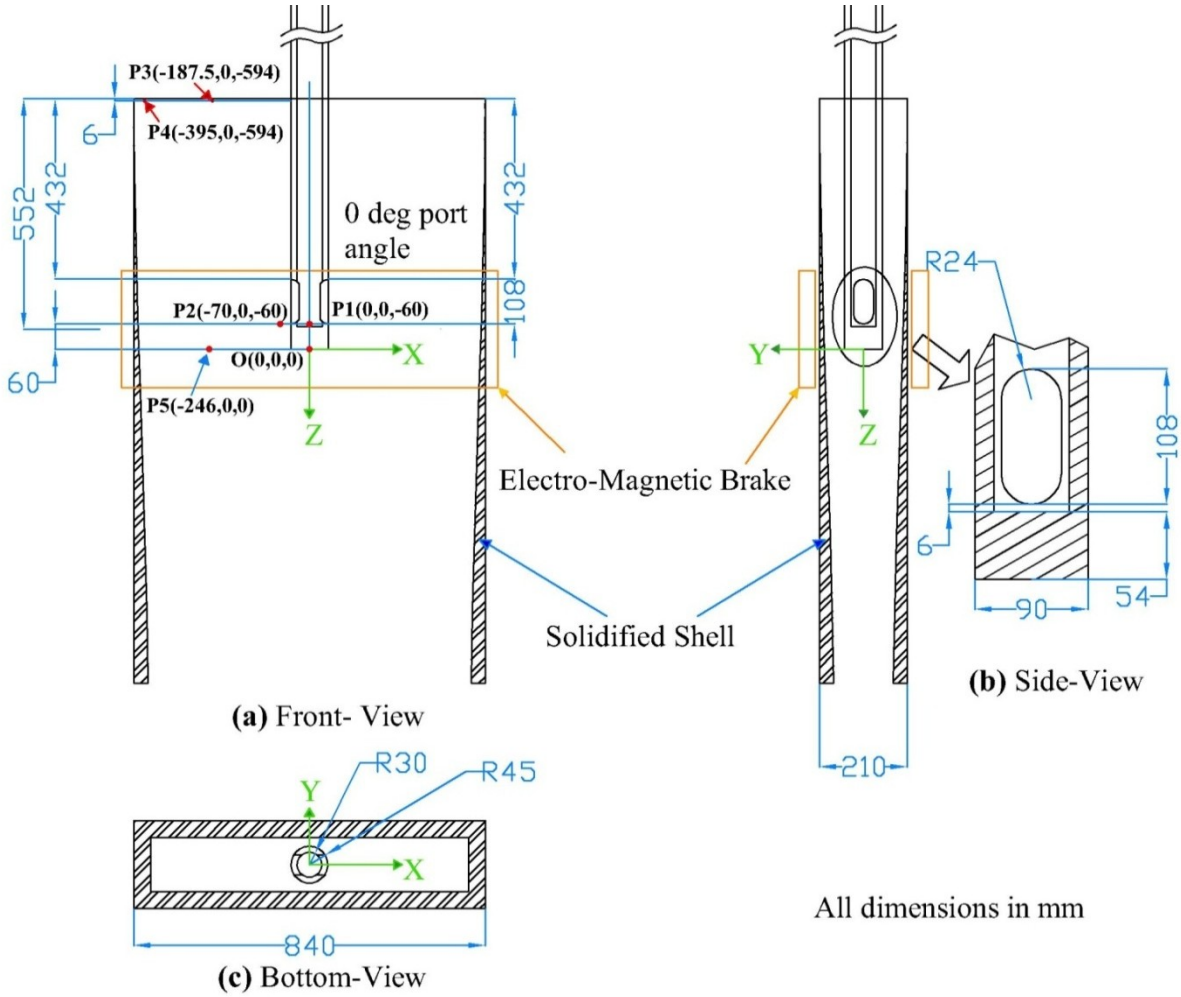

Figure 3.1- Geometry of the real caster with the rectangle showing the location of the applied ruler EMBr

The GaInSn model has been experimentally studied with no magnetic braking (Case 1) [12], magnetic braking with insulated walls (Case 2) [12] and magnetic braking with conducting side walls (Case 3)[13]. Miao et al.[14] modeled all three cases with URANS. Chaudhary et al.[3] validated CUFLOW with measurements for Case 1 and Case 2, and also studied the flow features in detail. Case 3, which has conducting brass-plate wide-face walls, also was simulated in the current work to validate the model by comparing the results with measurements, and also to investigate the effects of wall conductivity.

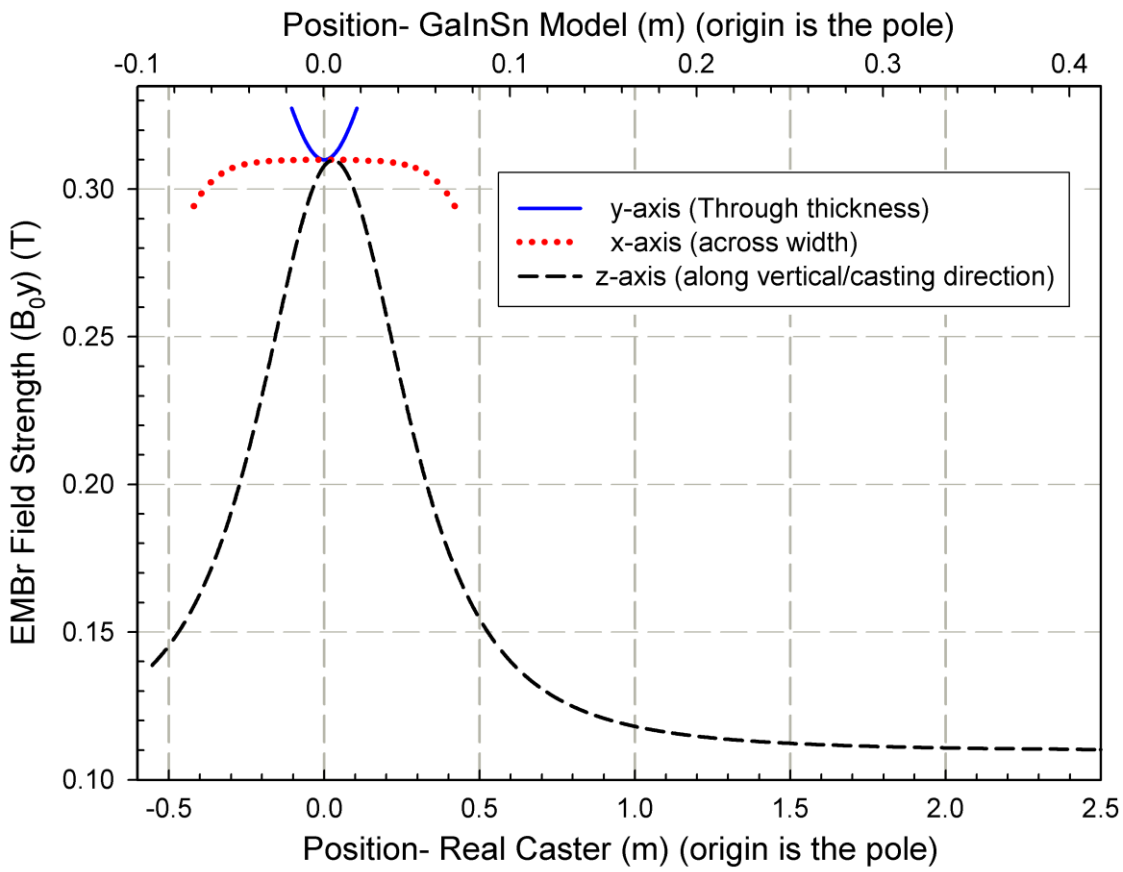

Figure 3.2- Applied magnetic field in the x,y and z directions for GaInSn model and real caster

For the real caster domain, simulations with no EMBr (Case 4) and with EMBr (Case 5) were performed. The computational domain for the real caster included both the liquid pool, shown in Figure 3.3, and the solidifying shell, which was initialized to move in the casting direction at the casting speed. The shell thickness s at a given location below the meniscus was calculated from $s = k\sqrt{t}$, where t is the time taken by the shell to travel the given distance and the constant k was chosen to match the steady-state shell profile predicted from break-out shell measurements by Iwasaki et al. [33]. The scaling factor of six over the GaInSn model was chosen to have mold dimensions typical of a commercial continuous slab caster. In the absence of EMBr, previous studies [34] have found that the Froude similarity criterion matches the flow patterns between a real caster and a 1/3*rd* scaled water model. In a

Table 3.1: Process Parameters

	GaInSn Model	Real Caster
Volume flow rate | nozzle bulk inlet velocity	$110mL/s$ | $1.4m/s$	$4.8L/s$ | $1.7m/s$
Casting speed	$1.35m/min$	$1.64m/min$
Mold width	$140mm$	$840mm$
Mold thickness	$35mm$	$210mm$
Mold length	$330mm$	$1980mm$
Computational domain length	$330mm$	$3200mm$
Nozzle port dimensions($width \times height$)	$8mm \times 18mm$	$48mm \times 108mm$
Nozzle bore diameter($inner \mid outer$)	$10mm \mid 15mm$	$60mm \mid 90mm$
SEN submergence depth (liquid surface to top of port)	$72mm$	$432mm$
Thickness of shell on the wide faces	$0.5mm$	$s(mm) = 2.75\sqrt{t(s)}$
Thickness of shell on the narrow faces	$0mm$	$s(mm) = 2.75\sqrt{t(s)}$
Fluid material	GaInSn eutectic alloy	Molten steel
Viscosity	$0.34\times10^{-6}m^2/s$	$0.86\times10^{-6}m^2/s$
Fluid density	$6360Kg/m^3$	$7000Kg/m^3$
Conductivity of liquid (σ_{liquid})	$3.2\times10^6 1/\Omega m$	$0.714\times10^6 1/\Omega m$
Conductivity of walls (σ_{wall})	$15\times10^6 1/\Omega m$	$0.787\times10^6 1/\Omega m$
Conductivity ratio (C_w)	0.13	0.13
Nozzle port angle	$0\ deg$	$0\ deg$
Gas injection	No	No
Reynolds number (Re, based on nozzle diameter)	41,176	118,604
Hartmann number (Ha= $BL\sqrt{\sigma/\rho\nu}$, based on mold width)	1,670	2,835
Froude number (Fr= $U/\sqrt{gL}$), based on mold width)	1.19	0.59
Stuart number (N= $B_0^2 L\sigma/\rho U$), based on mold width)	4.84	4.84
Cases	1. No-EMBr 2. EMBr with Insulated walls 3. EMBr with Conducting side walls	4. No-EMBr 5. EMBr with Conducting side walls

previous study with EMBr in a scaled mercury model [9], Froude number ($Fr = U/\sqrt{gL}$) and Stuart number ($N = B_0^2 L\sigma/\rho U$) similarity criteria were simultaneously maintained by scaling the casting speed and the magnetic field strength. Froude number maintains the ratio between inertial and gravitational forces, whereas Stuart number maintains the ratio between electromagnetic and inertial forces. However in the present study, only the Stuart number was matched between the $1/6th$ scaled GaInSn model and the corresponding real caster, keeping

the magnetic field strength constant at the realistic maximum of 0.31*Tesla*. Maintaining Froude similarity as well would have required a very high casting speed of 3.3*m*/*min*, and a higher magnetic field strength of 0.44*Tesla*. The applicability of this scaleup criterion was investigated by comparing results for the scale model and the real caster with EMBr.

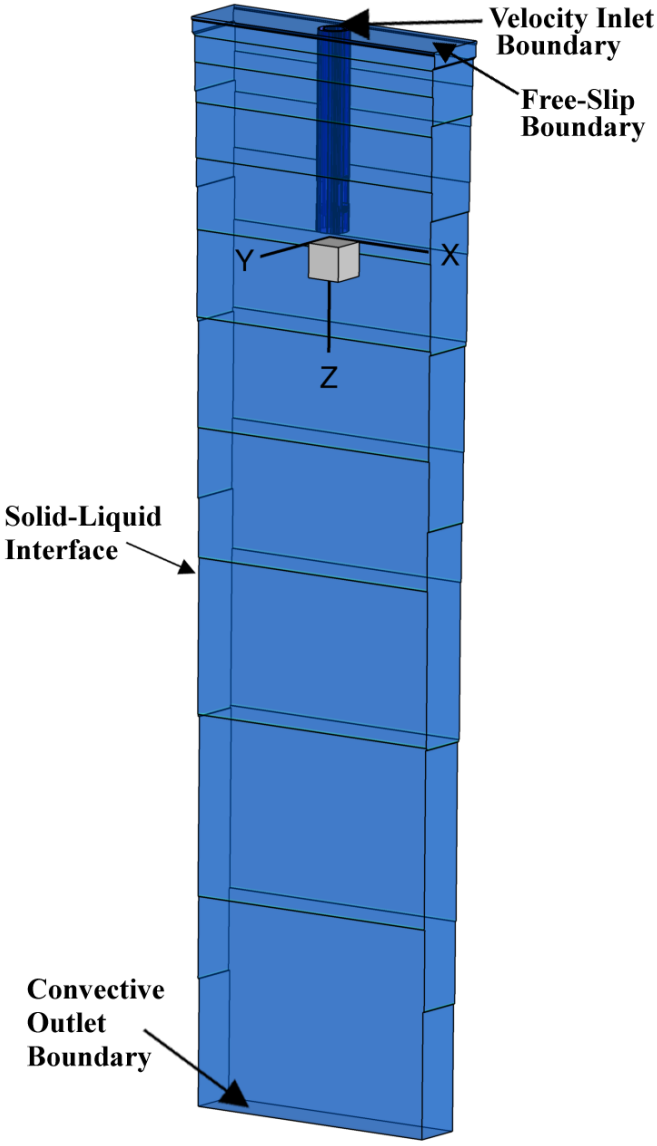

Figure 3.3 –Isometric view of the computational domain (fluid flow region) for the real caster

The GaInSn and the real caster computational meshes consist of 7.6 million and 8.8 million brick cells respectively. The nozzle in the physical model was very long (20 diameters), hence the nozzle inlet flow conditions had no effect on the flow entering the

mold. Thus in the computational model the nozzle was truncated at the level of the liquid surface in the mold and a fully developed turbulent pipe flow velocity profile (Eq. 3.1) was applied at the domain inlet, as used in previous studies [16, 3].

$$V_z(r) = V_z^{centerline}\left(1 - \frac{r}{R}\right)^{\frac{1}{7}} \tag{3.1}$$

Here $V_z(r)$ is the mean velocity in the casting direction as a function of r, which is the distance from the center of the circular nozzle, and R is the radius of the nozzle. The top free surface in the mold was a free-slip boundary with zero normal velocity and zero normal derivatives of tangential velocity. A convective boundary condition (Eq. 3.2) was applied to all three velocity components at the two mold outlet ducts on the narrow faces (NF) in the case of the scaled model [16] and across the open bottom of the real caster domain.

$$\frac{\partial u_i}{\partial t} + U_{convective}\frac{\partial u_i}{\partial n} = 0 \qquad i = 1,2,3 \tag{3.2}$$

Here $U_{convective}$ is the average normal velocity across the outlet plane based on the average inlet flow rate, and n is the direction normal to the outlet plane. This equation is discretized and rearranged to update the velocity components on the outlet boundary at the end of every time step. In order to conserve mass, a correction to the normal velocity component is applied at the beginning of every time step as follows:

$$u_{normal}^{new} = u_{normal} + (U_{convective} - Q_{current}/A_{outlet}) \tag{3.3}$$

All other boundaries were solid walls and the wall treatment previously reported by Werner and Wengle [35] was applied. In the real caster, the boundaries between the shell and fluid region were initialized with fixed downward vertical velocity equal to the casting speed, which accounts for mass transfer from the fluid region to the solidifing shell. Insulated

electrical boundary condition $\left(\frac{\partial \phi}{\partial n} = 0\right)$ was applied on the outer-most boundary of the computational domain. The fluid flow equations were solved only in the fluid domain and the MHD equations were solved in the entire computational domain, including the brass walls for the GaInSn domain and the shell (shaded) region for the real caster domain.

3.2.2. Computational Details and Cost

The cases without the EMBr field were started with a zero initial velocity whereas the EMBr cases were started from a developed instantaneous flowfield from a simulation with no magnetic field. For the GaInSn model, the magnetic field was applied after 10 seconds of simulation time (200,000 time steps) for the conditions of Case 1. The flow field for Case 3 was then allowed to develop for 5 seconds before starting to collect the time averages. The time averaged quantities were stabilized for 2 seconds after which the turbulence statistics were collected for 10 seconds. This simulation required a total of 10 days of calendar computation time. The real caster simulation was also started first with zero initial velocity and no magnetic field (Case 4). The collection of time averages was started after 10 seconds (200,000 time steps) and the turbulence quantities were calculated after the means stabilized for 5 seconds. The turbulence quantities were then averaged for another 15 seconds, requiring a total of 10 days computing time. For the case with EMBr (Case 5), the developed no EMBr flow field was taken as a starting condition and the flow was allowed to stabilize for 10 seconds physical time before calculating the time averaged quantities. The turbulence quantities were then calculated after the time averaged quantities were stabilized for 5 seconds of physical time after which further averaging for 10 seconds was performed. This calculation required a total of 15 days computation time.

The computations were performed on a NVIDIA C2075 GPU with 1.15GHz cuda-core frequency and 6GB memory. The solution times for the EMBr cases were nearly double that

of the cases without EMBr, which also require the solution of the electric Poisson equation (EPE). The calculations with EMBr produced approximately 55,000 time steps per day for the GaInSn model and approximately 35,000 time steps per day for the real caster. The computational expense due to a larger grid size and double precision accuracy in the real caster cases required larger computing time per time step.

3.3. Results for the GaInSn scaled model

3.3.1. Comparison with Experimental Measurements

Measurements of time-varying horizontal velocity (V_x) in the GaInSn model were collected at 5Hz using an array of ten ultrasonic Doppler velocimetry (UDV) sensors [12, 13]. The first sensor was placed at $z = -40mm$ on the midplane of the narrow face and the subsequent ones were placed at 10mm intervals below the first. Figure 3.4a shows the contour plot of measured time averaged horizontal velocity [12, 13]. The plot on the top is for the insulated wall case whereas the lower plot is for the conducting side wall case. Figure 3.4b shows the contour plot of the same quantity calculated using CUFLOW for both cases. However, here the vertical resolution was matched with the experimental data by using the calculated values on ten horizontal lines with positions matching those of the UDV sensors in the experimental setup. Figure 3.4b shows a good qualitative match with the measurements for both the insulated and conducting side wall cases. Figure 3.4c shows the contour plots of the same calculated quantity for both cases but with a much higher data resolution, using all computational grid points. In this plot the entire jet region is visualized by a continuous region of high velocity unlike the previous plots. The low vertical resolution, used in the measurements, results in graphical artifacts such as two isolated regions of high velocity in each jet. The plots shown in Figure 3.4b help in comparing the calculated results with the plots obtained from the measurements, which exhibit almost exactly the same respective flow fields, including the two high-velocity regions in each jet. However, the higher-resolution

contour plots of the same data look considerably different from the low-resolution contour plots.

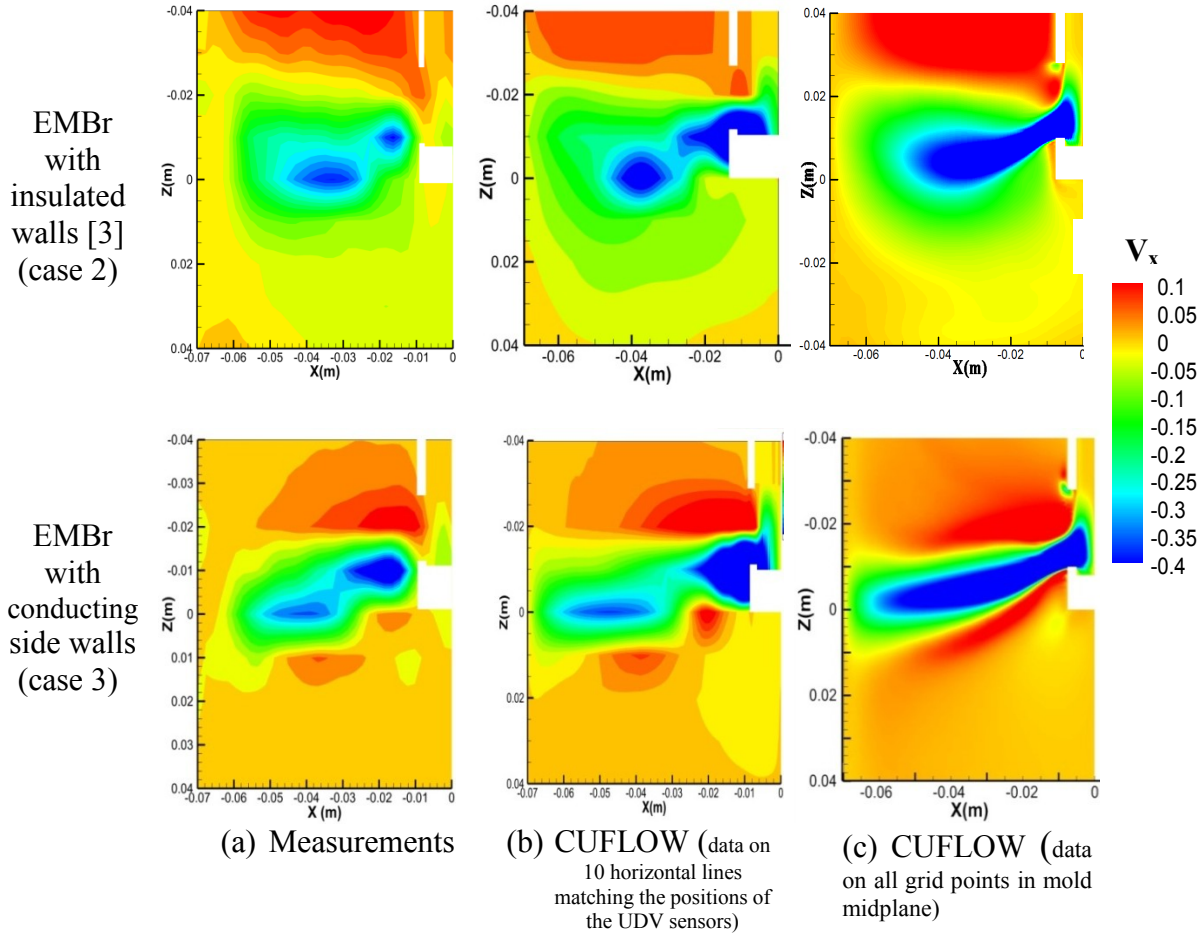

Figure 3.4 - Contours of time-averaged horizontal velocity for case2 (top) and case3 (bottom) for the GaInSn model caster (a) Measurements (b)(c) Calculations using CUFLOW

The application of a ruler magnetic field is known to deflect the jet upwards [3] and a similar behavior is seen in the simulation with conducting side walls. The time-averaged horizontal velocity shows that the jet angles for both conducting and insulated cases are nearly the same, but the conducting side wall case shows less spreading of the jet, before it impinges on the narrow face, as compared to the case with insulated walls. Also, for the case with a conducting shell strong recirculation regions were seen, just above and below the jet (negative velocity implies flow towards the narrow face). This contrasts with the insulated

wall case, in which very strong recirculating flow is seen only above the jet. Both flow fields contrast to that without EMBr (presented later) where no recirculation is seen in this zoomed-in portion of the domain.

Figure 3.5 compares the measured and calculated time averaged horizontal velocities on three horizontal lines, 90 mm,100 mm and 110 mm from the free surface (corresponding to the 4th, 5th and 6th sensors) for the case with conducting side walls. Results computed using both the WALE SGS model and the CSM SGS model are shown. For the present case, both models give results which closely match the measurements but the CSM SGS model is expected to perform better for the real caster because of the higher Reynolds number and larger fraction of the energy in the filtered scales. Further, the large Stuart number, 4.84, induces anisotropy of the turbulence [36] which is better represented by the CSM SGS model. Thus from now onwards, only results with the CSM SGS model are shown. The agreement between the measurements and the calculations is good except close to the SEN and narrow face walls, which is primarily due to limitations in the UDV measurements. Timmel et al [12, 13] report that the UDV measurements are inaccurate near the SEN and the walls due to the low vertical spatial resolution and interaction of the ultrasonic transducer beam with solid surfaces.

The transient horizontal velocities measured by the UDV probes were compared to the calculations at P5 (point in the jet region), P6 (point close to the port exit) and P7 (point in the upper recirculation region) in Figure 3.6b, 3.6c and 3.6d respectively. In order to match the conditions of the transient measurements closely, a 0.2 second time average was performed on the calculated signal to match the response frequency (5Hz) of the measuring instrument [13]. The measured and the time-averaged signals match well.

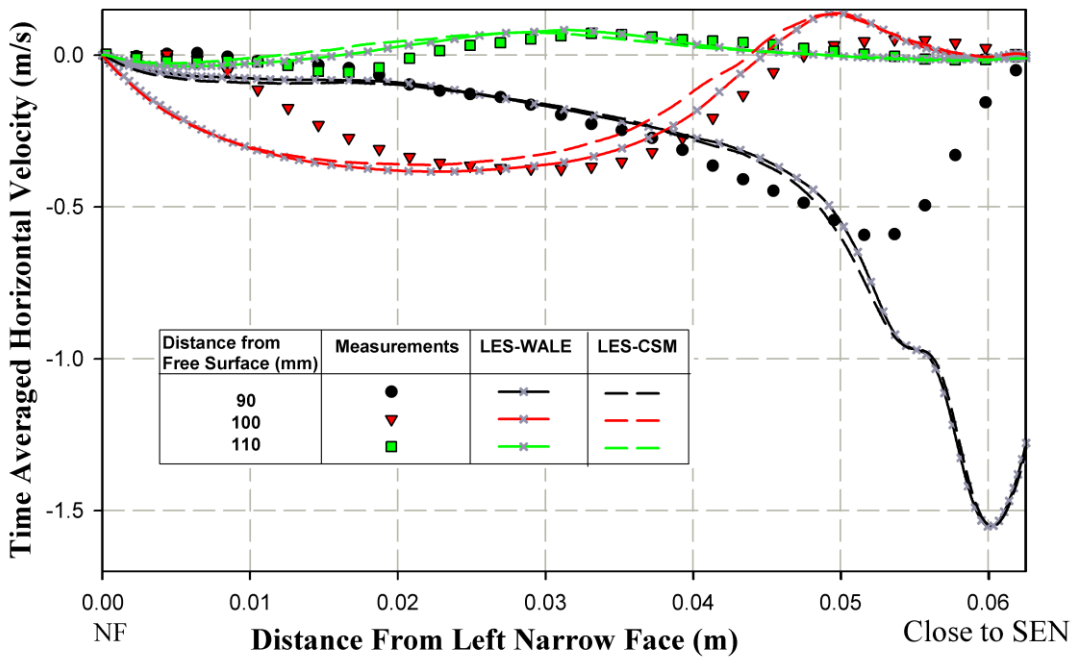

Figure 3.5- Comparison of time averaged horizontal velocity between measurements and CUFLOW calculations using WALE SGS model and CSM SGS model for the GaInSn model caster with conducting side walls (case 3)

3.3.2. Instantaneous Results

The flow pattern for the EMBr case with insulated walls (Case 2) was remarkably different from the same case with conducting side walls (Case 3). The transient differences are even greater. Figure 3.6a shows the history of horizontal velocity for Case 2 at P5, a typical point in the jet, which contrasts greatly with the history in Figure 3.6b for Case 3 at the same location. The insulated wall case has strong low-frequency fluctuations which indicate large scale wobbling of the jets. This behavior is not seen in the conducting side wall case. The contrasting transient behaviors are clearly visualized in Figure 3.7, which show contour plots of instantaneous velocity magnitude at the midplane between wide faces at two instances, separated by 2 seconds, for both cases. Case 2 has both side-to-side and up-and-down wobbling of the jets, which makes the entire mold flow very unstable; whereas the jet in Case 3 is relatively stable. Figure 3.7 also shows the contours of time-averaged velocity magnitude for both cases (leftmost column). Case 2 has an asymmetric flow pattern even after collecting

the mean for 28 seconds, whereas the calculations with conducting side walls (Case 3) produced a symmetric time-averaged velocity field after averaging for only 12 seconds. This finding of increased flow stability with conducting side walls, and the contrast of very unstable flow with insulated walls [3], agrees with previous findings using both experiments and URANS models [13, 14].

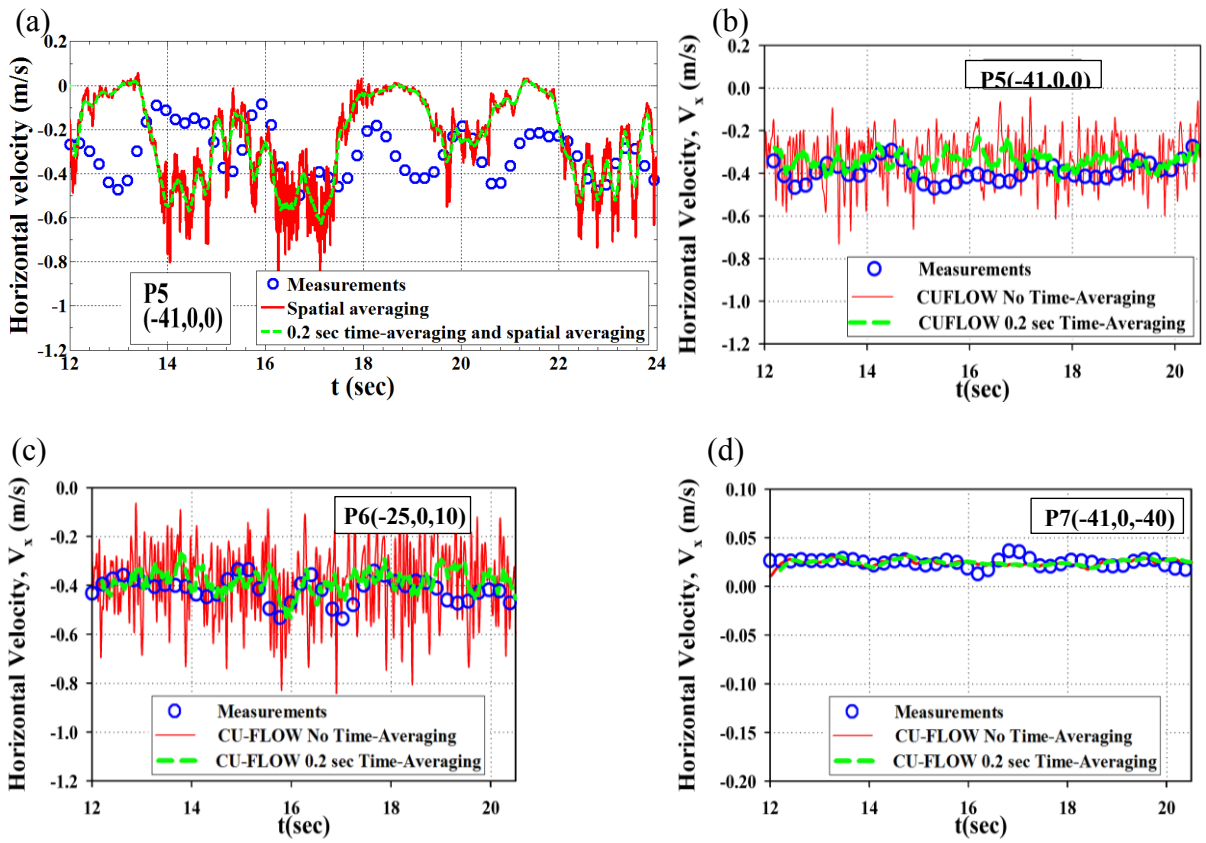

Figure 3.6- Transient horizontal velocity in the jet comparing CUFLOW predictions and measurements in the GaInSn model (a) EMBr with insulated walls [3] and (b)(c)(d) EMBr with conducting side walls

The change in the flow pattern in the presence of the conducting side walls can be explained by the behavior of the current paths [14]. In the case with insulated walls (Case 2) the current lines may close either through the conducting-liquid metal or the Hartmann layers (present on

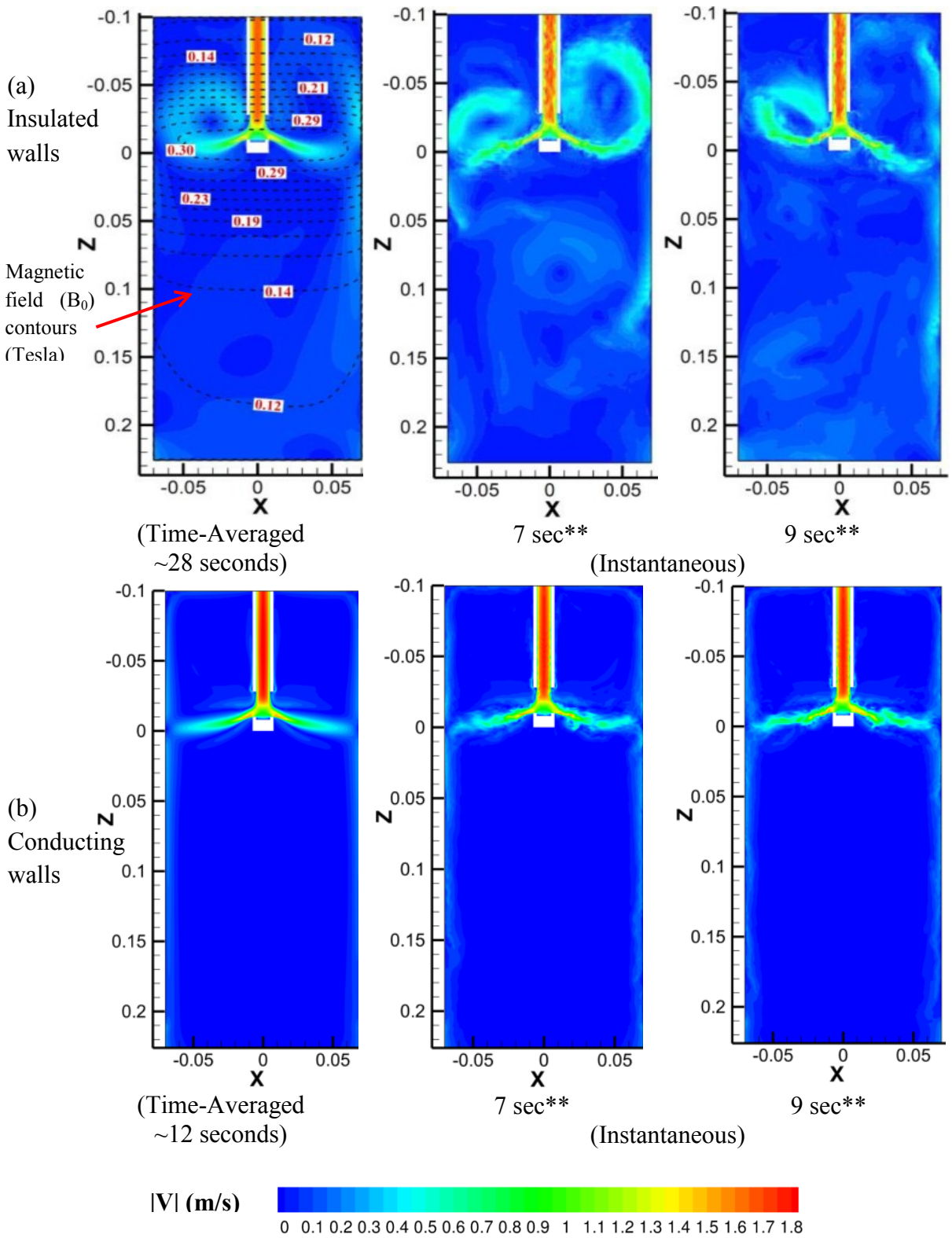

Figure 3.7- Time-averaged and instantaneous velocity magnitude (a) EMBr with insulated walls[3] (b) EMBr with conducting side walls (All axes in meters)
(**Time after switching on EMBr)

walls perpendicular to the magnetic field). The Hartmann layers are extremely thin (~40μm in Case 3 [14]) at high Ha number ($\delta_{Ha} \sim Ha^{-1}$), resulting in high resistance, and thus most of the return current closes through the liquid metal itself. The enhanced stability of the mold flow in case with conducting side walls (Case 3) is enabled by the alternative path provided to the current through the conducting side walls. Most of the current is generated in the jet region and closes locally through the conducting side wall, forming short loops where the magnetic field is strongest. This prevents the current from wandering through the flow, where it can generate strong transient forces causing the unstable flow as seen with insulated walls. Figure 3.8a shows the time-averaged current paths in the regions of the mold with maximum current for Case 3. These current loops are the most important because they produce the maximum Lorentz forces acting on the flowing metal. Most of the current paths can be seen to go up and through the jet, travel to the conducting side walls, move down through the conducting side walls (where they are colored grey) and then back to the jet. Figures 3.8b and 3.8c show contour plots of time-averaged current density magnitude for Case 3 with vectors in the y-z plane at $x = -12mm$ (slice through the jet) and x-y plane at $z = -10mm$ (slice through the SEN ports) respectively. Figure 3.8b shows that the maximum current density arises within the conducting side walls near to the nozzle bottom, while within the fluid, the maximum is associated with the jet, near where high-velocity fluid intersects with the maximum field strength. Figure 3.8c shows that there is high current density in the conducting side walls all across the width of the mold at $z = -10mm$. More importantly, the highest current densities in the fluid region are found inside and just outside the nozzle ports, decreasing towards the narrow faces.

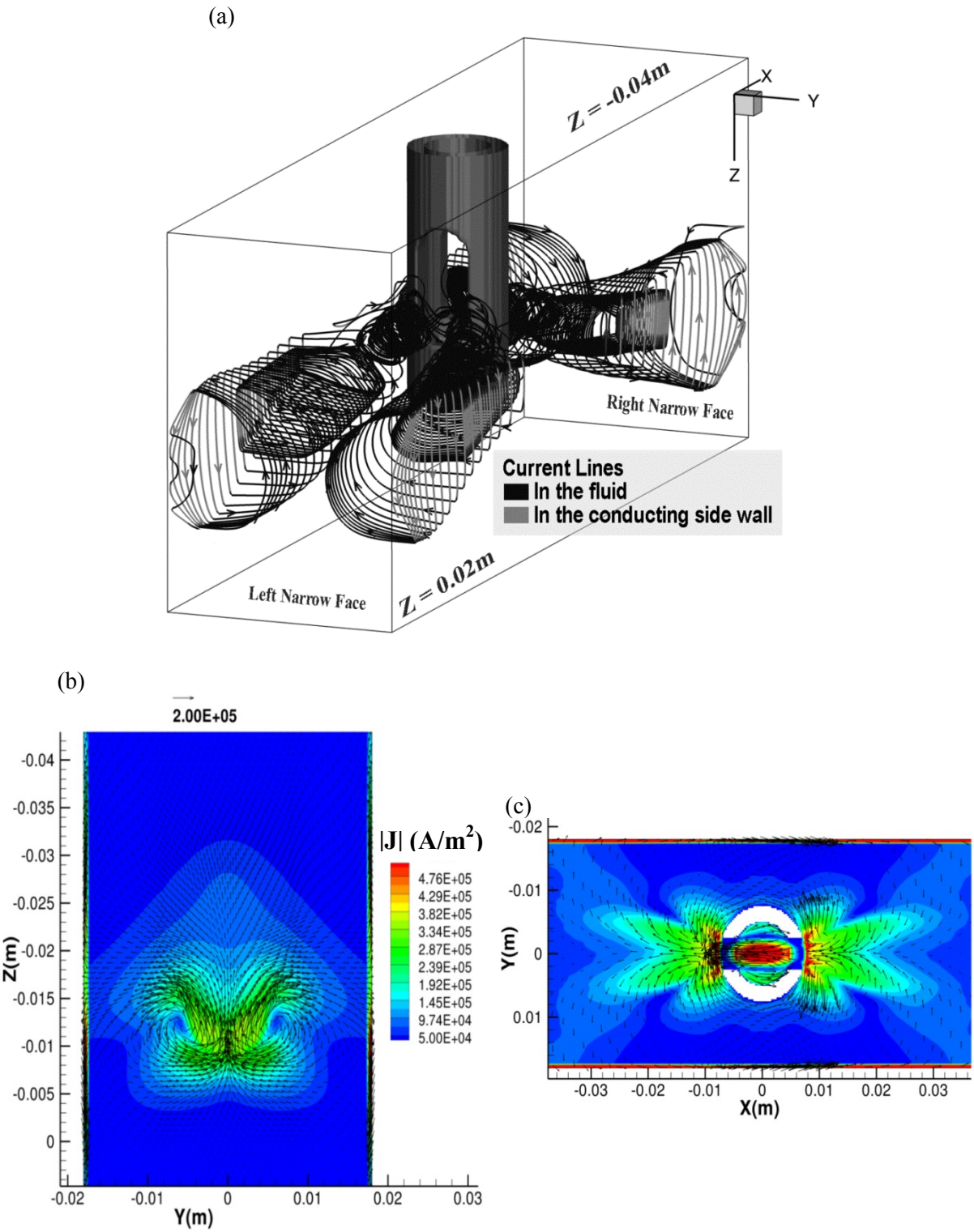

Figure 3.8- (a) Current paths in the mold close to the nozzle ports. Contour plots of time-averaged current density magnitude on (b) Vertical y-z plane at x= -12mm with vectors of J_y and J_z (c) Horizontal x-y plane at z= -10 mm with vectors of J_x and J_y

3.3.3. Time Averaged Results

3.3.3.1. Nozzle Flow

Figure 3.9a and 3.9b show the time-averaged velocity magnitude and vectors at the nozzle port for the No-EMBr (Case 1) and EMBr (Case 3) cases respectively. It can be seen that the time-averaged velocity magnitudes are symmetric in the jet region near nozzle port exit for both cases indicating adequate sample size. The jet in the presence of the EMBr (Case 3) was deflected upwards and was also much thinner compared to the No-EMBr case. There were two strong recirculation regions, above and below the jet, which return the jet fluid close to the jet exit.

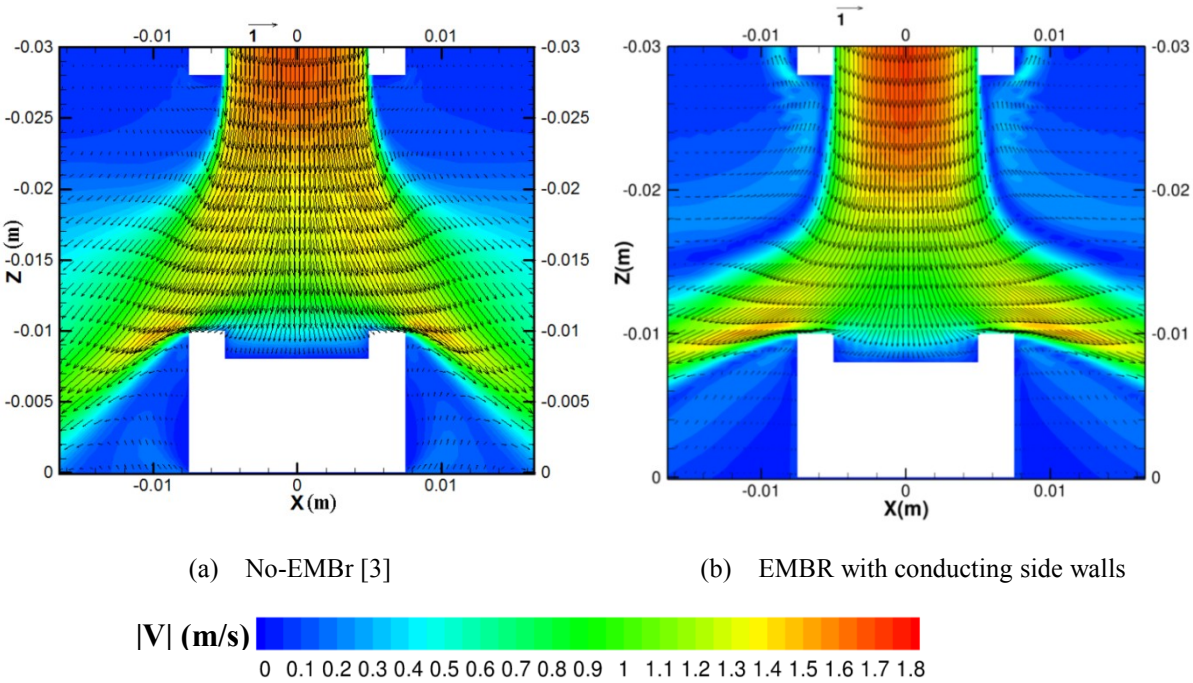

(a) No-EMBr [3] (b) EMBR with conducting side walls

Figure 3.9- Time-averaged velocity magnitude contours and vectors near nozzle bottom in different cases (Note: 66% Vectors are skipped for clarity.)

The application of magnetic fields is known to suppress turbulent fluctuations [27]. This effect is shown in Figure 3.11 where the $\overline{w'w'}$ component of resolved Reynolds stresses is plotted inside the nozzle in the midplane parallel to the narrow faces. The No-EMBr case has the larger fluctuation levels and hence sustains swirl in the z-y plane which was evident from

the high values of the $\overline{w'w'}$ and $\overline{v'v'}$ (not shown) components. The EMBr configuration applies a high strength of magnetic field in the nozzle region which almost completely suppresses the swirl. The suppression was however found to be lesser in the conducting side wall case. Thus another contributing factor to the stability of the mold flow pattern for the conducting side wall case was the better mixing present in the nozzle, as swirling jet flow is known to improve jet stability.

3.3.3.2. Mold Flow

Figure 3.10a shows the contours of time-averaged velocity magnitude and vectors in the mold for the No-EMBr case. Figure 3.10b also shows the contours of time-averaged velocity magnitude for the EMBr case with conducting side walls but with streamlines instead of vectors. Due to the recirculating regions and high gradients close to the jets the vectors masked most of the details. The time-averaged velocity magnitude contours for both cases were symmetric about the nozzle in the entire mold region. Also both cases were found to have stable flow pattern but the No-EMBr (Case 1) case had a weak upper recirculation region. In Case 3 the recirculation regions were very close to the jet and after they reach the nozzle the upper recirculation continues upwards close to the SEN walls whereas the lower recirculation continues in the casting direction. In traditional double roll flow pattern, which was seen in the No-EMBr case, the lower recirculation region extends deep into the mold before returning to the jet region, whereas in the conducting side wall case it is restricted close to jet with the flow below this region aligned to the casting direction.

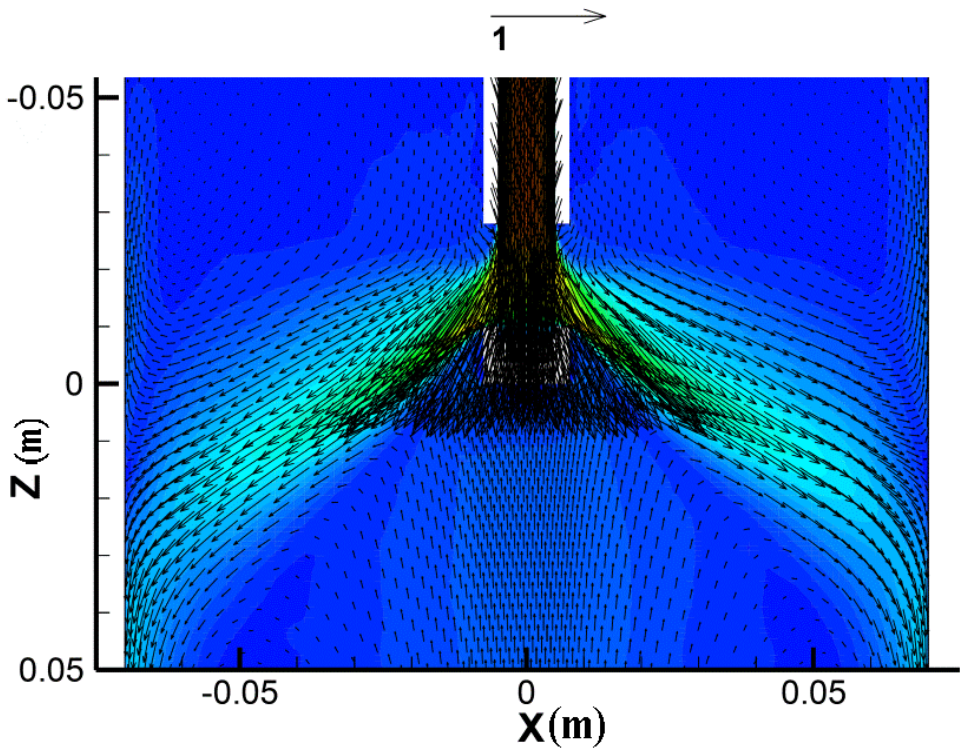

(a) No-EMBr

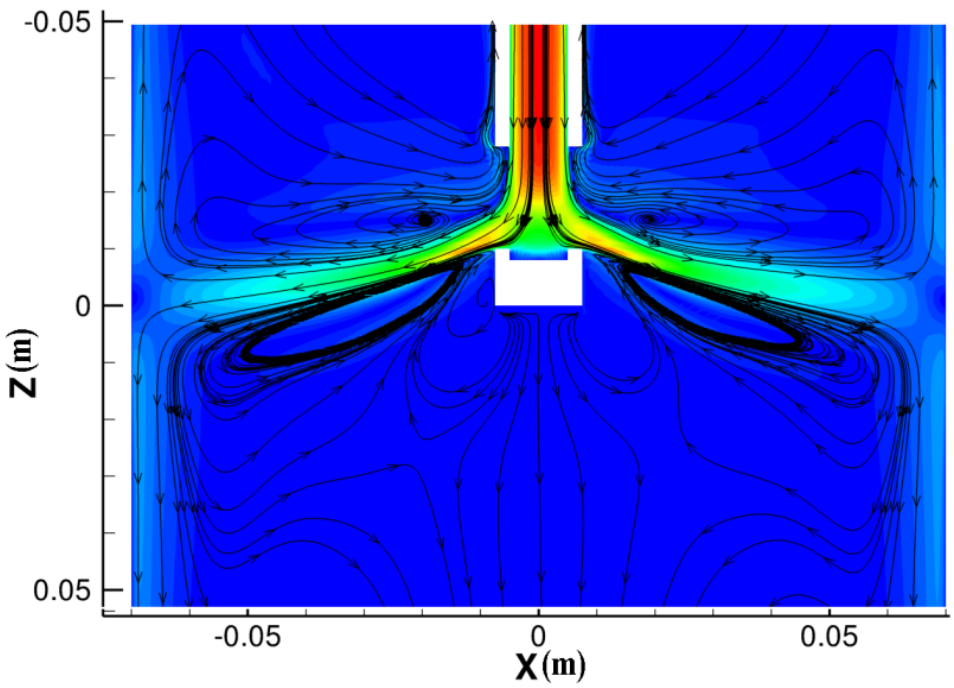

(b) EMBr with conducting side walls

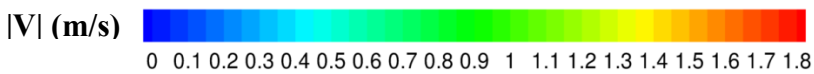

Figure 3.10- Contours of time-averaged velocity magnitude and vectors/streamlines at mold midplane for (a) No-EMBr case [3] (b) EMBr case with conducting side walls (Note: 83% vectors are skipped for clarity.)

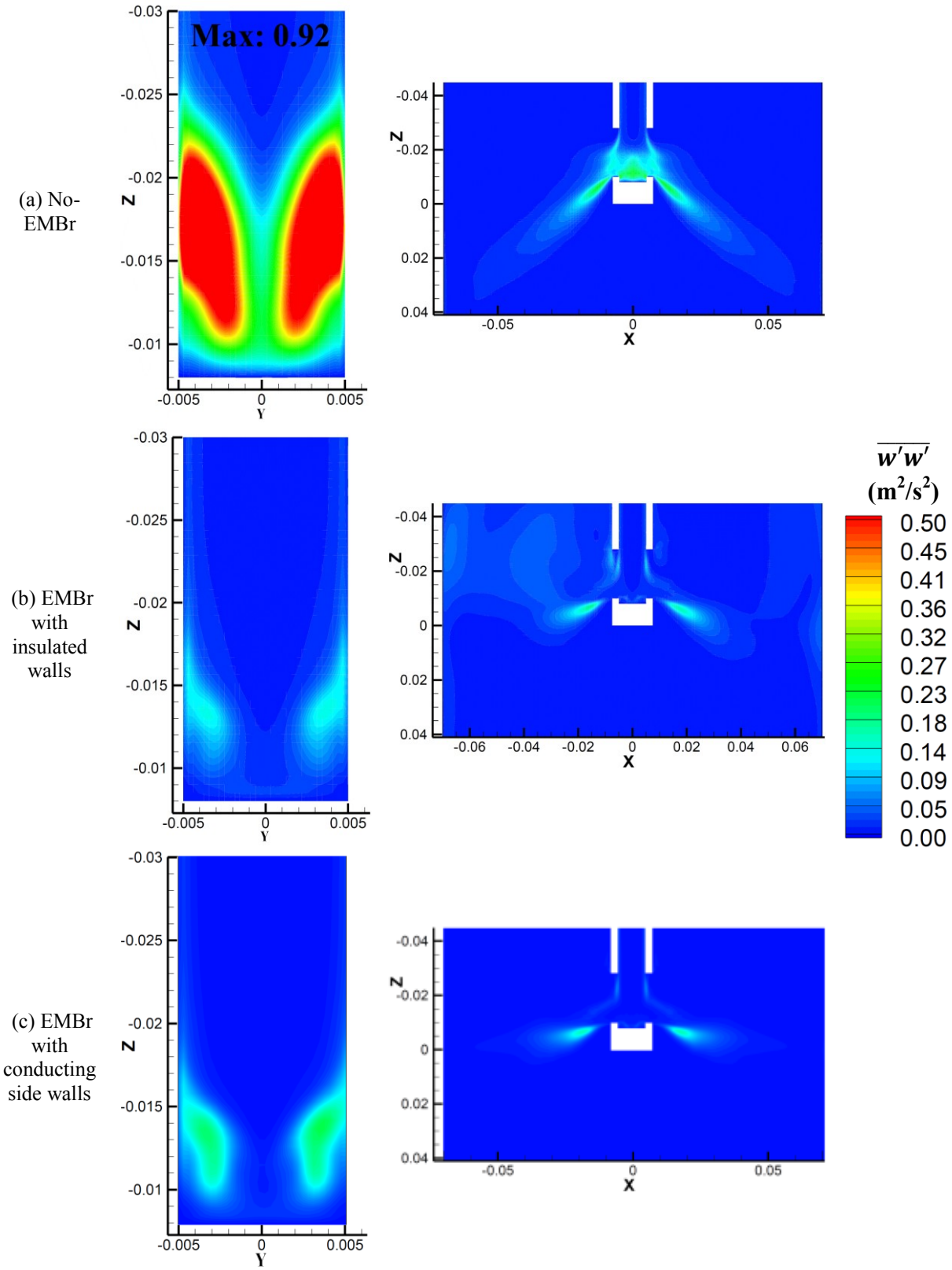

Figure 3.11- $\overline{w'w'}$component of resolved Reynolds stresses at mold mid-planes between wide faces (below) and between narrows faces inside nozzle (above) (a) No-EMBr [3], (b) EMBr with insulated walls [3] and (c) EMBr with conducting side walls (All axes in meters)

The $\overline{w'w'}$ component of resolved Reynolds stresses in the mold region is presented in Figure 3.11. The resolved Reynolds stresses components , $\overline{w'w'}$, $\overline{v'v'}$ and $\overline{u'u'}$, were restricted to the jet region in the conducting side wall case (Case 3), unlike the insulated wall case (Case 2) where the fluctuations extend into the upper mold region confirming an unstable flow pattern. This enhanced suppression in the mold region for the conducting side wall case is attributed to the concentration of the high current density and Lorentz force to the region of strongest magnetic field. The resulting stable upper roll flow is beneficial for defect reduction.

3.3.3.3. Surface Flow

Flow across the top surface is of critical importance to steel quality. Various defects form if the surface flow is either too fast or too slow. Figure 3.12 shows the variation of time-averaged horizontal surface velocity 1mm below the free surface across the mold width, for Cases 1, 2 and 3. In general, the surface velocity in this GaInSn model is low due to the deep submergence depth. The No-EMBr case has the lowest surface velocity (max= 0.045 m/s) and might be susceptible to meniscus freezing [3]. The EMBr with conducting side wall case (Case 3) has the highest surface velocities and the time-average field is also symmetric on both sides. The maximum time-averaged surface velocity for the EMBr with insulated wall case (Case 2) lies between that of Cases 1 and 3, and variation across the mold width for this case was asymmetric about the SEN.

The EMBr flow with conducting side walls also has the beneficial effect of lowering the turbulent kinetic energy at the surface, as shown in Figure 3.13. The extremely high and asymmetric turbulent kinetic energy at the surface for the insulated wall case suggests large-scale level fluctuations and associated quality problems. Thus the effect of the shell

conductivity should be considered in order to accurately study the mold flow under the influence of applied magnetic fields, especially when considering transient phenomena.

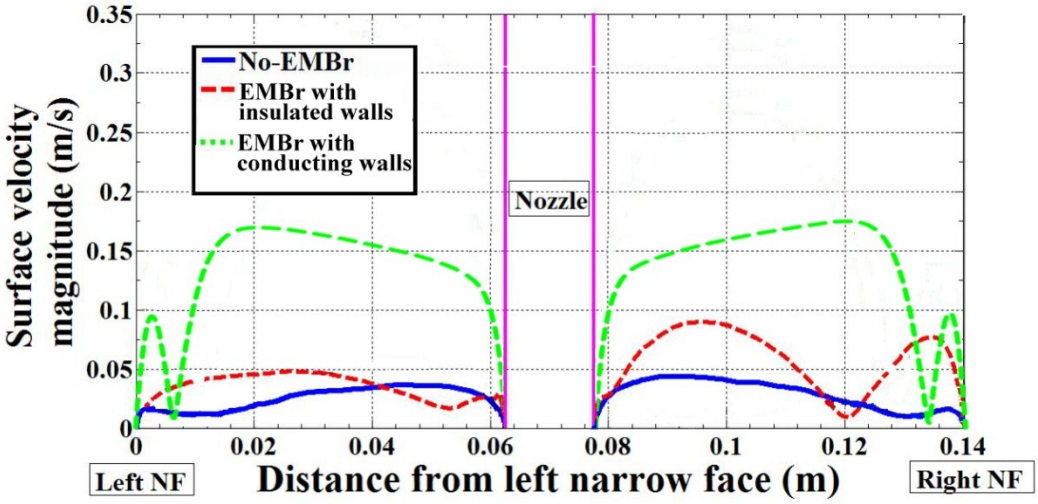

Figure 3.12- Time-averaged horizontal velocity at the surface plotted against distance from left narrow face.

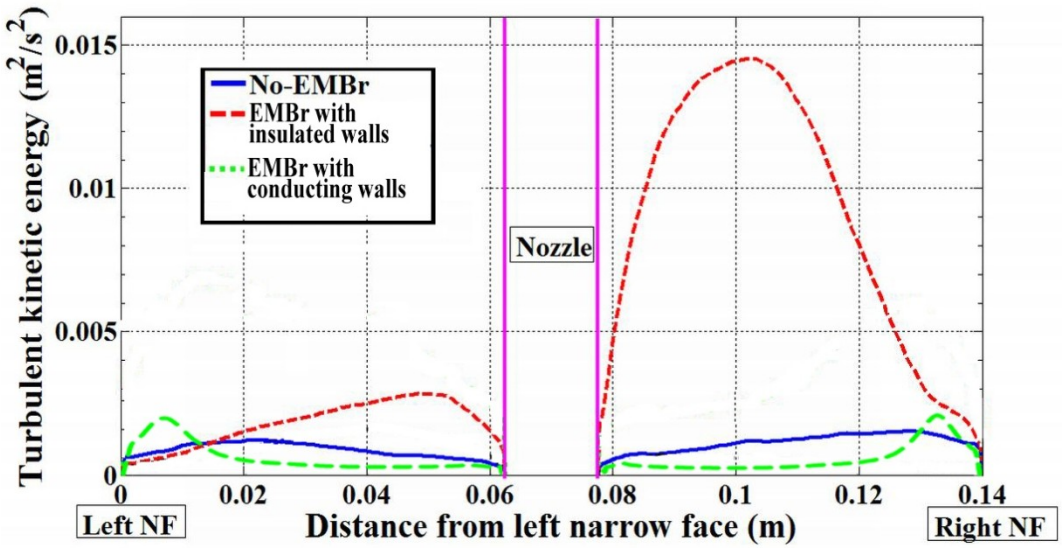

Figure 3.13- Resolved turbulent kinetic energy at the surface plotted against distance from left narrow face.

3.4. Results for the Real Caster

3.4.1. Transient Results

3.4.1.1. Effect of EMBr on Transient Flow

Having validated the CUFLOW model, it was applied to simulate transient flow in a realistic full-scale commercial caster. For both the No-EMBr (Case 4) and the EMBr (Case 5) cases, Figure 3.14 shows instantaneous contours of velocity magnitude at two different times, at intervals of one second. It can be seen that with no EMBr, the transient flow field is dominated by small-scale fluctuations. The application of EMBr damps most of the small-scale fluctuations and deflects the jets upwards. These deflected jets were reasonably stable and the long time fluctuations were comparable with the No-EMBr case. The flow below the jet region quickly aligns to the casting direction and the lower roll was restricted to a small, elongated recirculation loop just below the jet.

It has been previously seen that an applied magnetic field preferentially damps the transient flow fluctuations parallel to its direction [27]. Figure 3.15 shows the computed time history of two fluctuating velocity components (y in the thickness direction and z in the casting direction) at two points P1 (center of SEN bottom) and P2 (near port exit) as previously indicated in Figure 3.1 for the two cases, with and without the magnetic field. The high variation in V_z' and V_y' at P1 with no EMBr indicates the presence of swirling flow in the nozzle bottom. The frequency of the alternating direction of the swirl can be approximated, from the time history of V_y' in Figure 3.15a, to be about 1.5Hz. With EMBr, the low velocity fluctuations at P1 indicate very little swirl in the nozzle which results in a smoother jet with less high-frequency turbulent fluctuations. The time history at P2 shows highly anisotropic suppression of turbulence, as the thickness-direction V_y' component is damped more by the magnetic field.

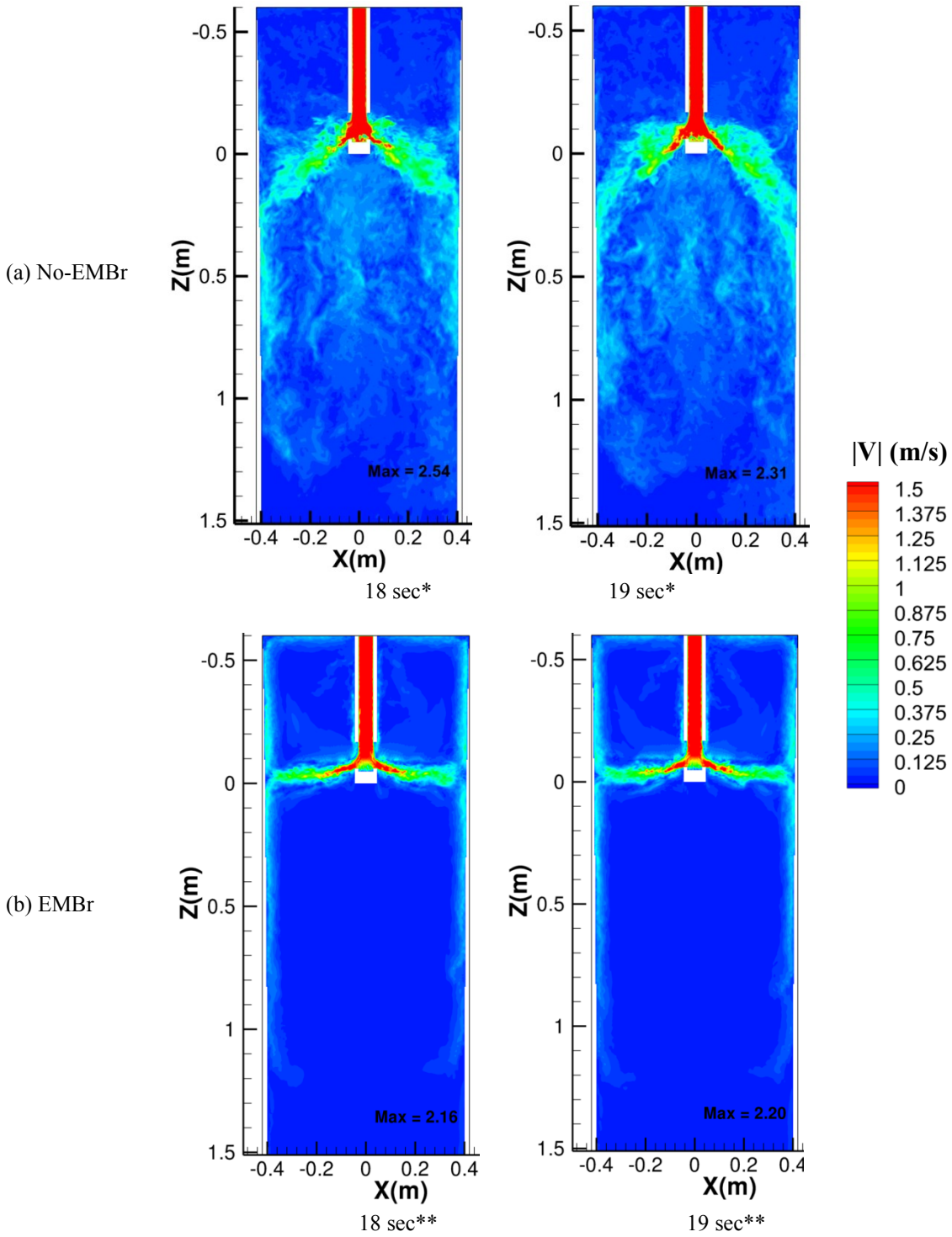

Figure 3.14 - Instantaneous velocity magnitude for the real caster cases (a) No-EMBr (b) EMBr

(* Time from start of simulation, **Time after switching on EMBr)

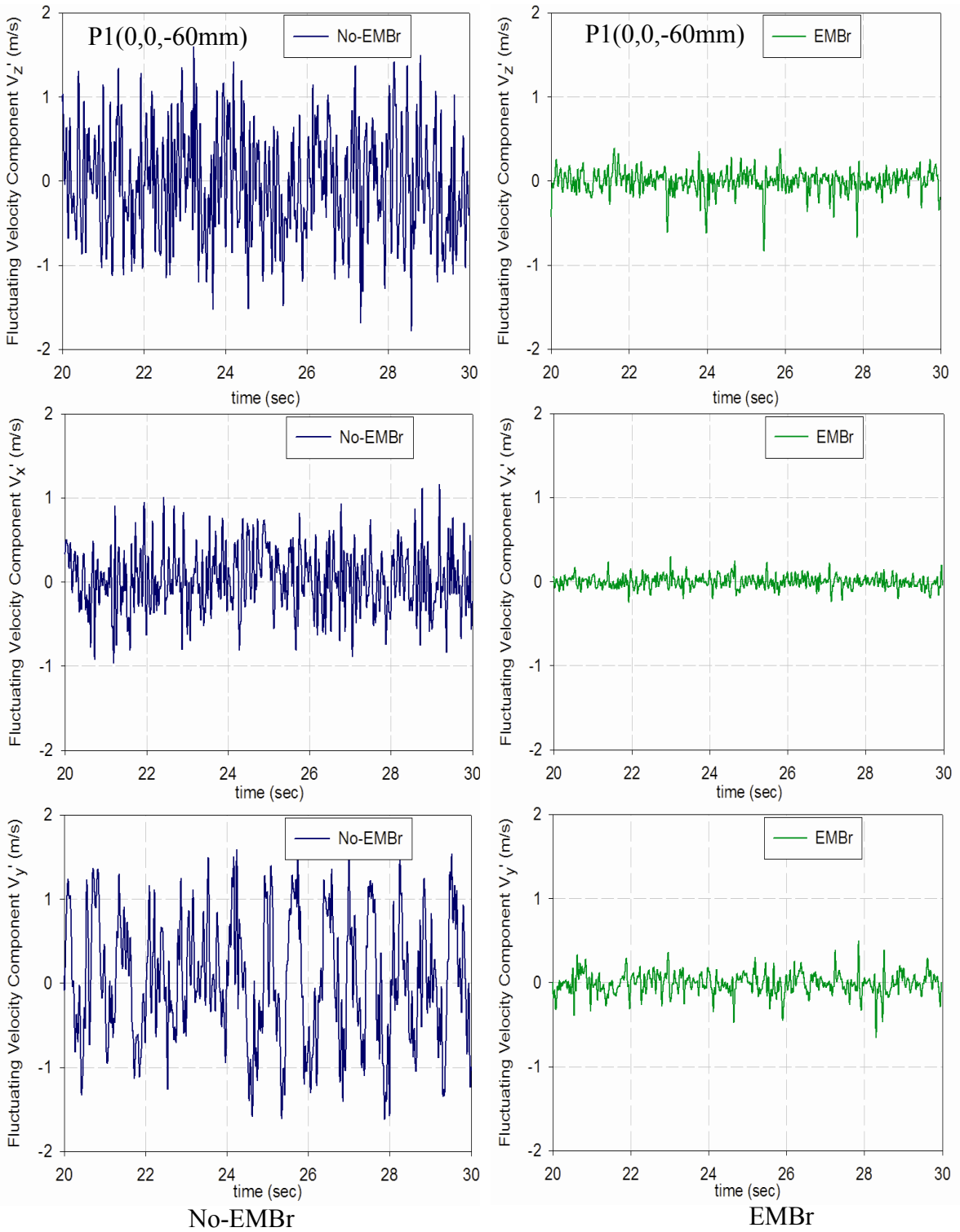

(a)

Figure 3.15- Time variation of components of the fluctuating velocity plotted for the real caster cases at (a) P1 (b) P2. Contd.

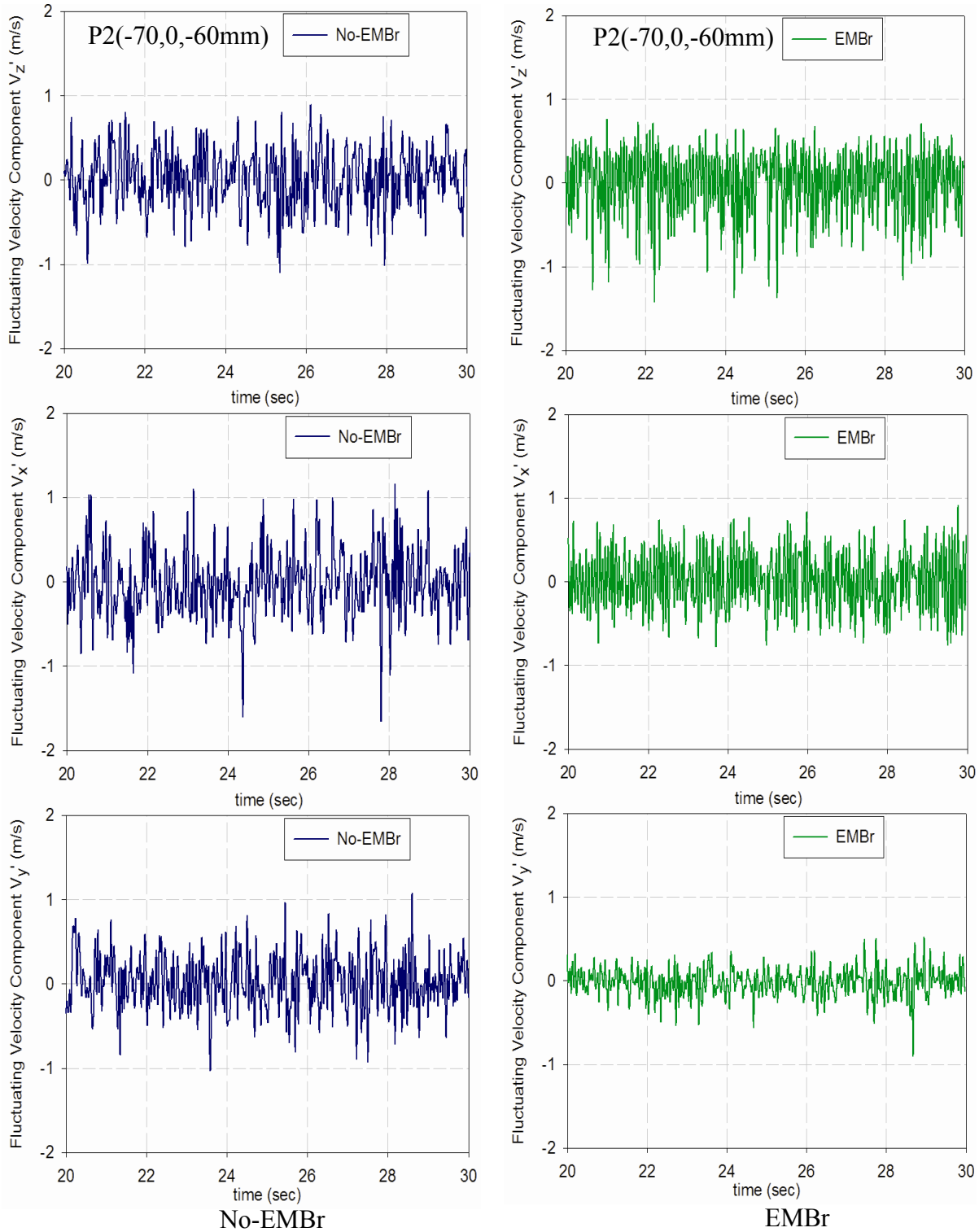

(b)

Figure 3.15- Time variation of components of the fluctuating velocity plotted for the real caster cases at (a) P1 (b) P2

3.4.1.2. Free Surface Fluctuations and Effect of Scaling

The profile of the steel surface level (Z_{sur}) and its fluctuations are of critical importance to the steel quality mold slag entrainment and surface defects can occur if the fluctuations are too strong. The surface level can be approximated using the pressure method shown in Equation 3.4 [34] which gives an estimate of the liquid surface variation using a potential energy balance.

$$Z_{sur} = \frac{p - p_{mean}}{\rho_{steel}\ g} \tag{3.4}$$

The average pressure (p_{mean}) in the current study was calculated on the horizontal line along the top surface on midplane between the wide faces with g taken as $9.81 m/s^2$. Figure 3.16 shows three typical instantaneous surface level profiles, with a 0.5 seconds moving time average, at three instances separated by 5 seconds each. With no EMBr, the surface level remains almost horizontal with higher levels (~0.5mm) close to the narrow face and SEN. The level variation in the EMBr case was greater, due to the increase in momentum, both close to the narrow face (~2.7mm) and to the SEN (~1.7mm). The time variation of the level is plotted, at P3 and P4, and is shown is Figure 3.17. Point P3 is at the midpoint between the narrow face and the SEN; and P4 is close to the narrow face as indicated in Figure 3.1. The No-EMBr case at both locations is found to be stable with only small scale fluctuations. The EMBr case at P3 has small fluctuations with oscillation amplitude of ~0.5mm; whereas at P4 there was a periodic oscillation with amplitude of 3mm and frequency of ~0.2Hz.

In order to compare the level fluctuations predicted by the GaInSn model with the real caster they must be scaled. The obvious scaling method is to multiply the scale-model level fluctuations by the geometric length scaling factor (=6). However, a better scaling method is

to calculate the ratio of the Froude numbers in the two casters, and rearrange to give the following length scaling factor.

$$\frac{Z_R}{Z_S} = \frac{Fr_S}{Fr_R}\left(\frac{V_R}{V_S}\right)^2 = 2.974 \tag{3.5}$$

Here Z is the surface level profile including its fluctuation with time, V is any characteristic velocity, such as the casting speed or the inlet velocity, and the subscripts S and R represent the GaInSn scaled model and the real caster respectively. Figure 3.17 compares the scaled level fluctuations using both scaling methods, with the real caster history, for Case 3 at points P3 and P4. The geometric scaling method overpredicts the average surface level position and its fluctuations in the real caster (Case 5) at both locations. However, the predictions using the Froude-number based scaling factor match the calculated level fluctuations in the real caster very closely. This indicates that the surface level fluctuations in scaled models can accurately predict behavior in the real caster, if they are scaled based on the Froude-number relationship in Equation 3.5.

The velocity in the real caster can be predicted from the scaled model velocities using the relation

$$u_i{}^R = u_i{}^S\left(\frac{V_R}{V_S}\right) \tag{3.6}$$

where, u_i is any component of time-dependent local velocity and superscript S and R represent the GaInSn scaled model and the real caster respectively. The surface level fluctuation is scaled according to Equation 3.5 which can be simplified by substituting the definition of Froude number to yield

$$Z_R = Z_S\frac{V_R}{V_S}\sqrt{\frac{L_R}{L_S}} \tag{3.7}$$

where, L is any characteristic length scale ($L_R/L_S = 6$).

(a)

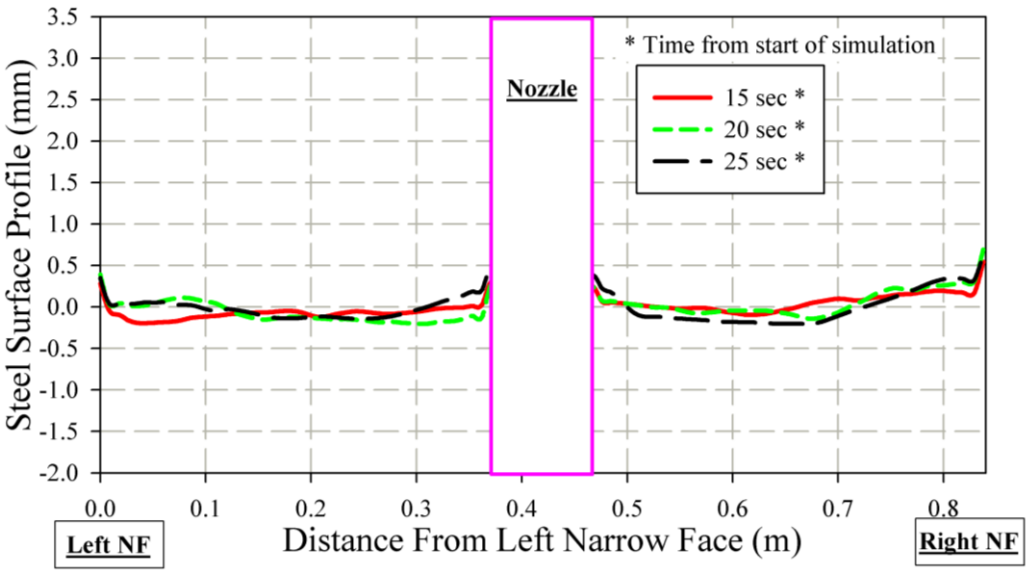

(b)

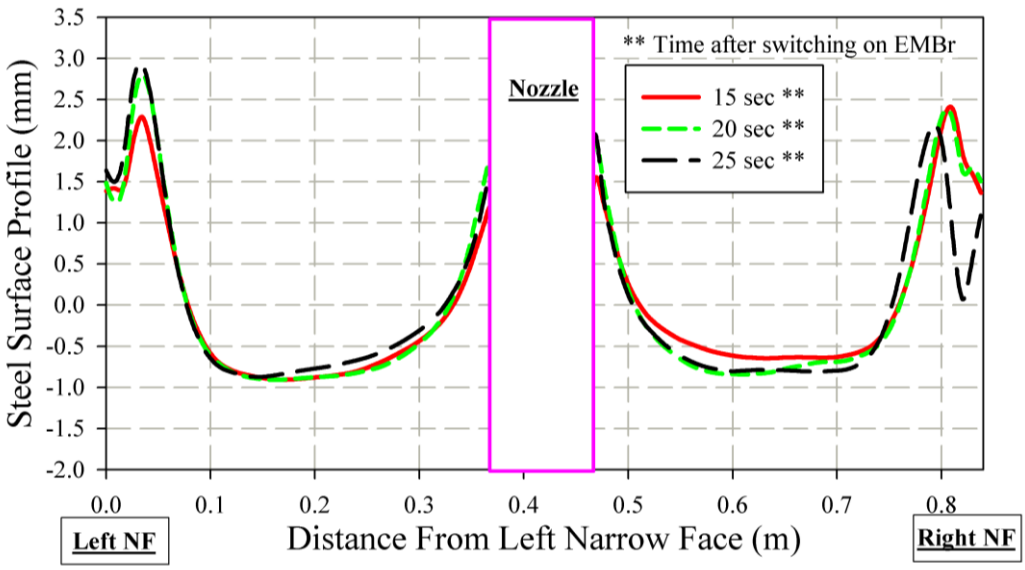

Figure 3.16- Instantaneous mold surface level prediction at three instances for the real caster cases (a) No-EMBr (b) EMBr

(a)

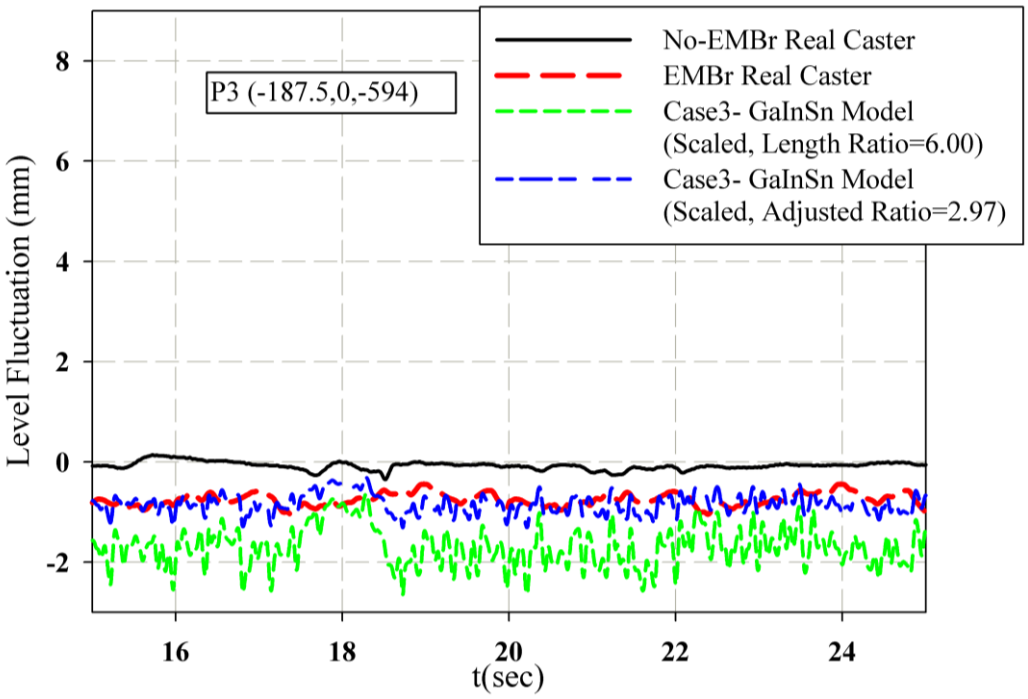

(b)

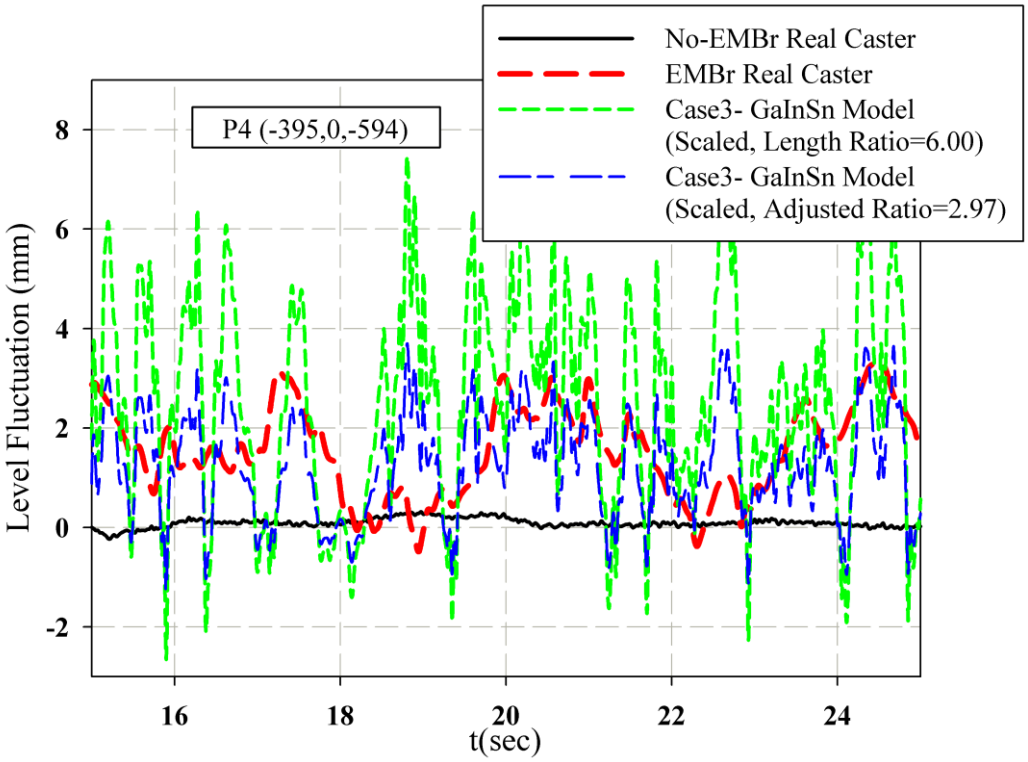

Figure 3.17- Mold surface level histories for the real caster cases and GaInSn model case 3 with scaled surface level (a) midway between SEN and narrow face at P3 and (b) near narrow face at P4

3.4.2. Time Averaged Results

3.4.2.1. Nozzle Flow

Figure 3.18 shows the contours of time-averaged velocity magnitude along with velocity vectors, for the No-EMBr and the EMBr cases. As expected, both contour plots are symmetric about the nozzle centerline indicating adequate time averaging. The jets in the No-EMBr case exit with a steeper angle (30° down) and spread more as compared to the jets in the EMBr case (10° down). Figure 3.19 shows the variation of time-averaged velocity magnitude at the vertical line of the midplane of the nozzle port exits. The No-EMBr case has a lower time-averaged velocity magnitude at the top of the nozzle port exit and the value steadily rises around 30*mm* from the top. The EMBr case also has a low time-averaged velocity magnitude at the top of the nozzle port exit but the value remains low more than halfway (~60*mm*) down the port height. The magnitude then steadily rises reaching approximately the same maximum value as the No-EMBr case. This indicates that there are flatter (in the Z-direction) and thicker (in the Y-direction) jets exiting the nozzle ports in the presence of the EMBr field.

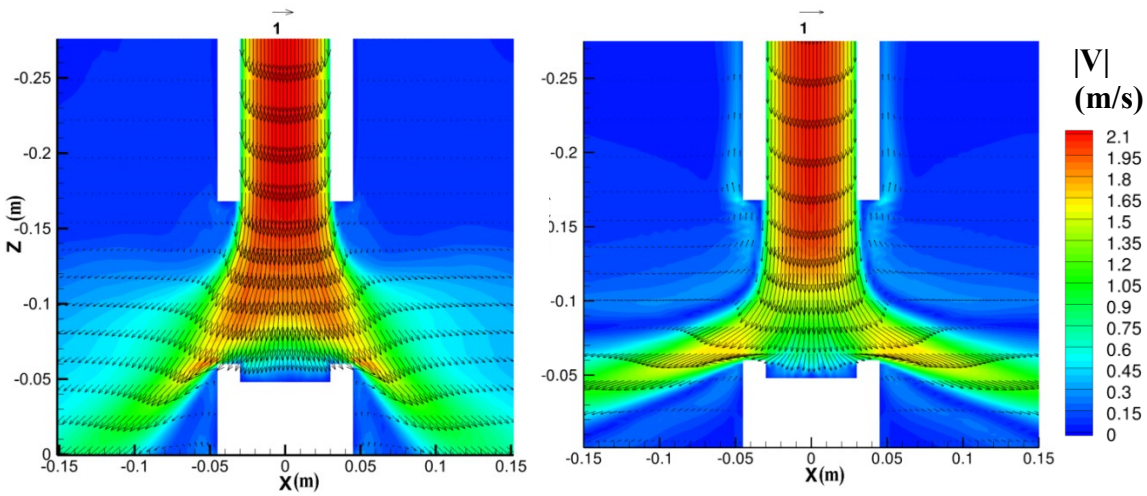

(a) No-EMBr (b) EMBr

Figure 3.18 - Time-averaged velocity magnitude contours and vectors near nozzle bottom for the real caster cases (a) No-EMBr (b) EMBr (Note: 83% Vectors are skipped for clarity.)

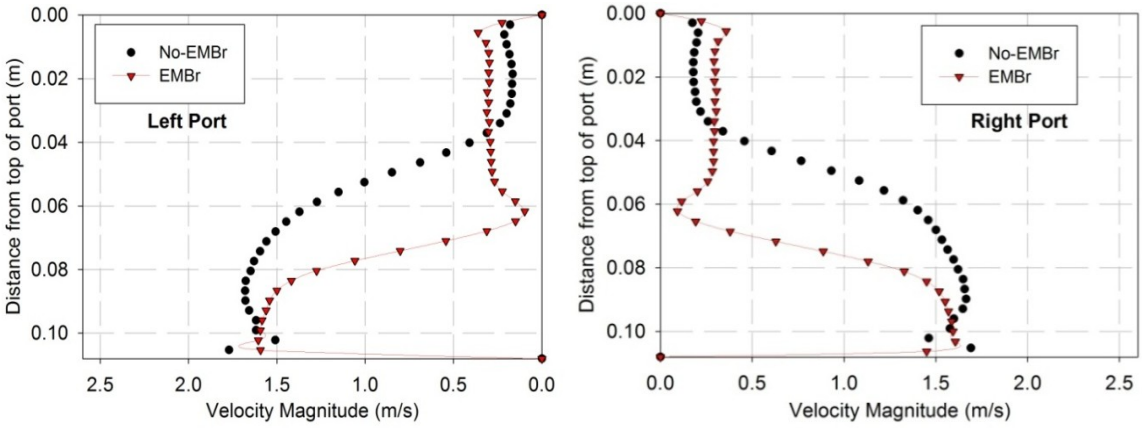

Figure 3.19 - Time-averaged velocity magnitude plotted along the port midplane vertical line for the real caster cases

The suppression of turbulence in the nozzle by the magnetic field is shown in Figure 3.20, where the turbulent kinetic energy (TKE) is plotted with distance down the nozzle port. The variation is symmetric for both cases, but the maximum value with EMBr is lower by a factor of approximately five. The present EMBr position applies the maximum magnetic field strength directly across the nozzle ports, which causes high suppression of both the turbulent fluctuations and the swirl in the SEN well (Figure 3.15). The contours of TKE inside the nozzle in the y-z midplane also aid in visualizing the suppression of alternating swirl in the nozzle as shown in Figure 3.21. The No-EMBr case has high TKE values inside the nozzle which were considerably reduced in the presence of the magnetic field as expected. The vectors of time-averaged velocity field in Figure 3.21 show the structure of the swirling flow at the nozzle bottom. In the No-EMBr case, the swirls at the SEN bottom are bigger and also have stronger velocities as compared to the EMBr case. Furthermore, another important effect of the EMBr field on the nozzle flow is seen in the time-averaged velocity profile in the Y-direction (Figure 3.21) which becomes considerably flat in the presence of the EMBr field. The diagonal components of the Reynolds stress tensors are not shown for Cases 4 and 5 to avoid redundancy as they were qualitatively similar to the Cases 1 and 3 (Figure 3.11) of the GaInSn model.

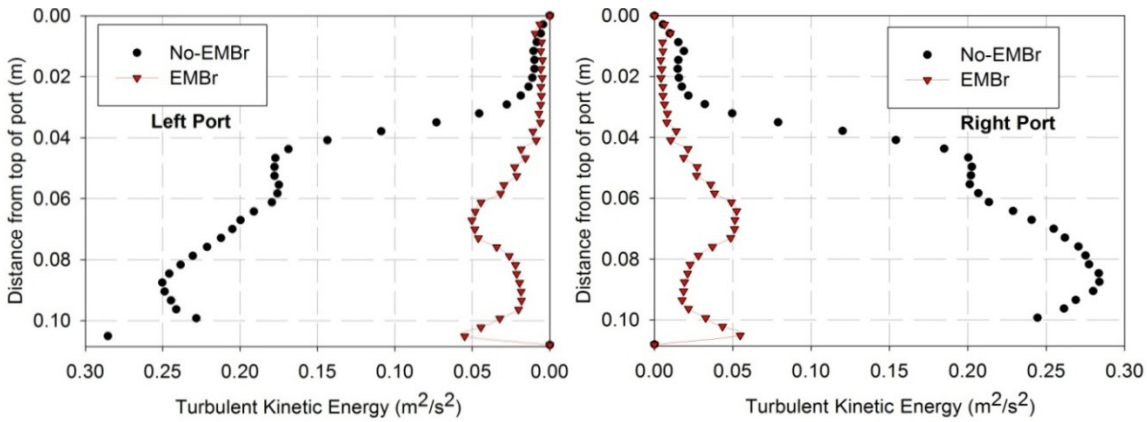

Figure 3.20 - Resolved turbulent kinetic energy plotted along the port midplane vertical line for the real caster cases

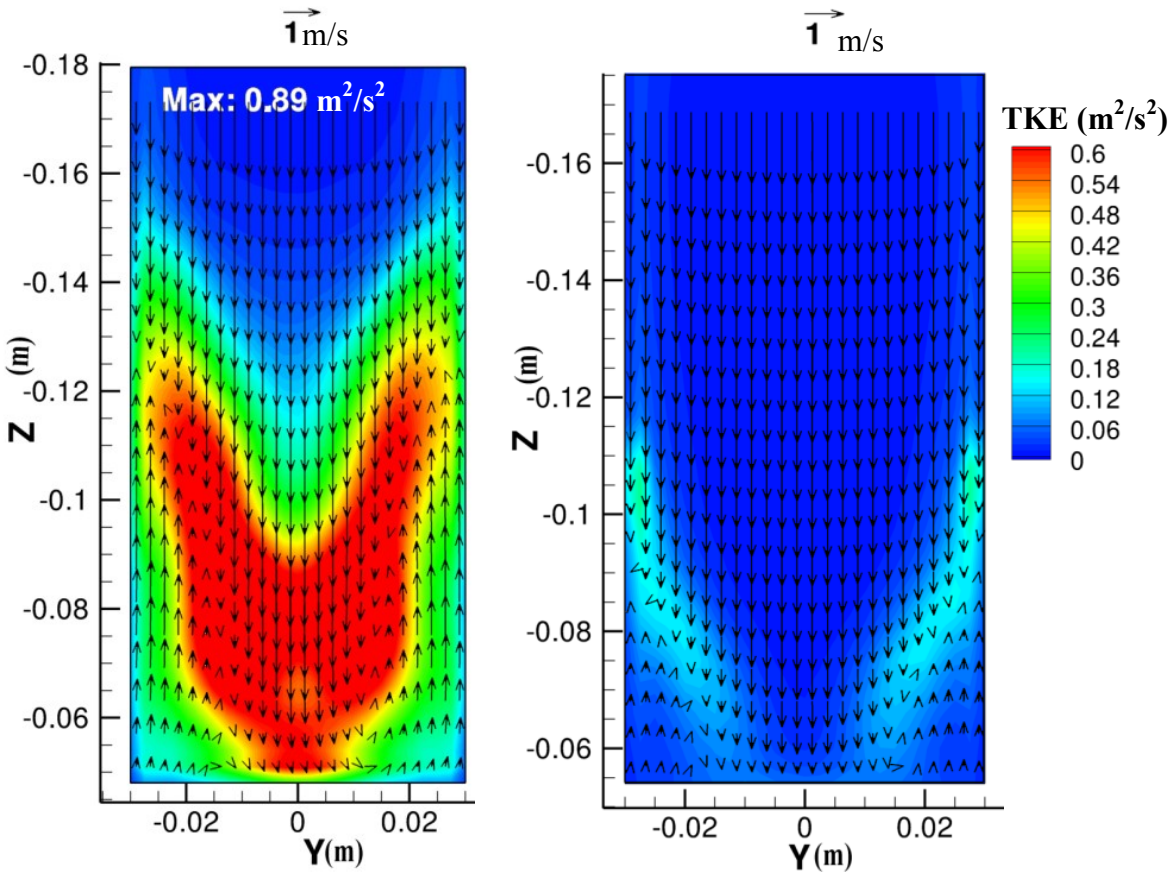

TKE[0.5($\overline{u'u'}$ + $\overline{v'v'}$ + $\overline{w'w'}$)]

(a) No-EMBr (b) EMBr

Figure 3.21 – Contours of turbulent kinetic energy with vectors of time-averaged velocity components (V_z and V_y) at mold mid-planes between narrows faces inside nozzle for the real caster cases (Note: 50% vectors are skipped for clarity.)

3.4.2.2. Mold Flow

Figure 3.22 shows the contours of time-averaged velocity magnitude in the mold region with streamlines for the No-EMBr and EMBr cases. Time averaging over a long time shows the double roll flow pattern present with a weaker upper roll. The mean mold flow pattern for the EMBr case is expected to be the same as the GaInSn model EMBr case with conducting-shell walls because Stuart number similarity was used to scale the process parameters. Application of the EMBr deflects the jets upwards resulting in an increased impinging velocity at higher positions on the narrow faces. The deflected jets strengthen the upper roll and create a similar stable flow pattern to the EMBr with conducting-shell walls case for the GaInSn model. The two small recirculation regions, immediately above and below the jets, as seen in the Case 3, were also observed in the real caster with EMBr case. In addition to this small recirculation region, there were two other recirculation loops in the upper mold region. The jet rising along the narrow face and the stream rising along the SEN wall form the two loops with opposite circulation.

The mold flow below the jet region critically affects the penetration depth and entrapment chances of the bubbles and entrained particles. Figure 3.23 shows variation of time-averaged vertical velocity along three horizontal lines, on the midplane between the wide faces, below the jet region. The downward velocity is always highest near the narrow faces, and decreases with depth down the the caster. The No-EMBr case has higher downward velocity close to the narrow faces as compared to the case with the EMBr field. However, the major difference can be seen away from the narrow faces where the flow is completely reversed with the application of the EMBr. Without EMBr, the flow in the central region is upward, i.e. moving towards the nozzle region, whereas the flow with EMBr aligns with the casting direction. In the EMBr flowfield, the downward velocities away from the narrow faces are small and comparable to the casting velocity (shown in the figure). These

low velocities in the EMBr case should be beneficial for the reduction in penetration and entrapment of bubbles and detrimental nonmetallic particles.

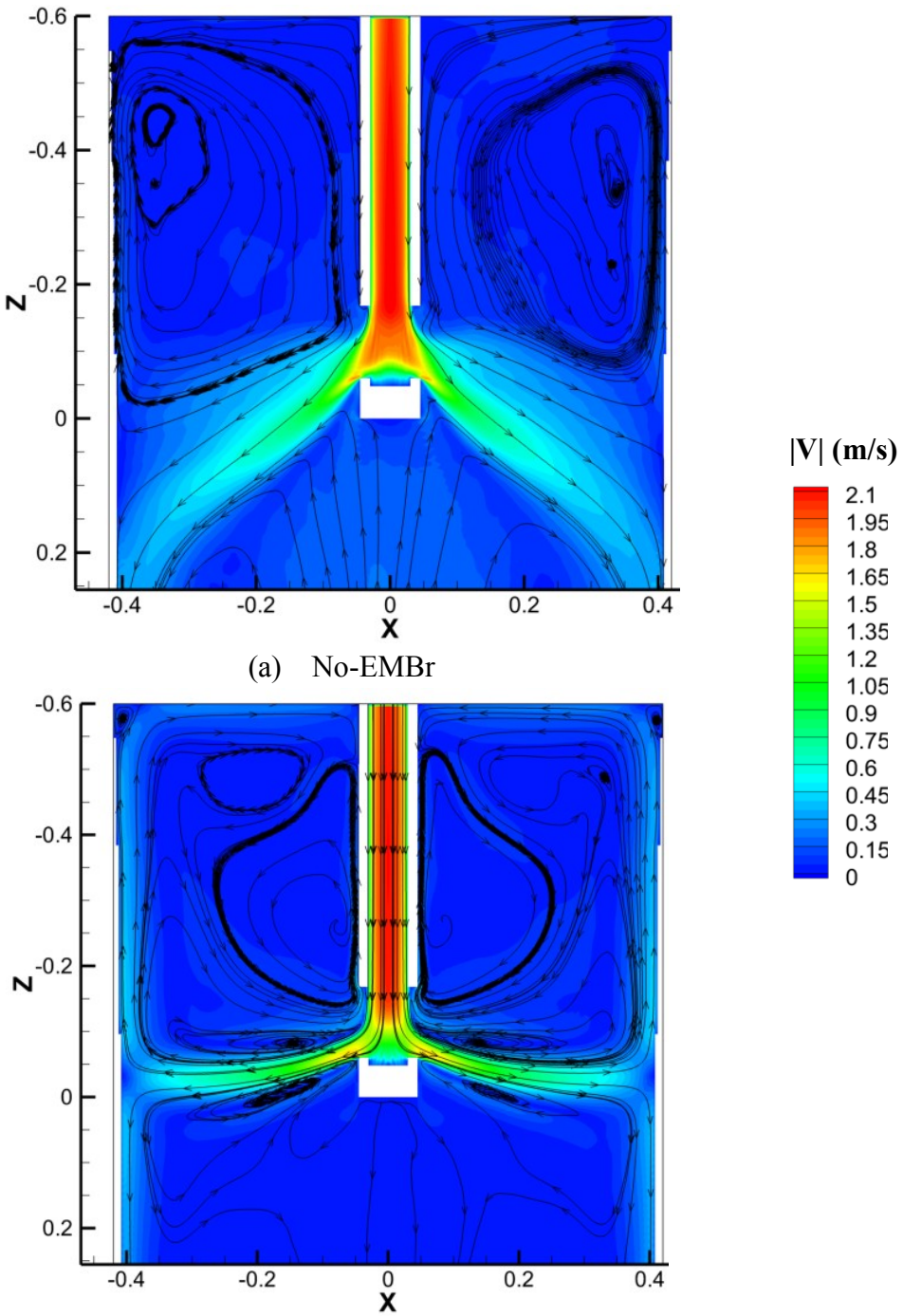

(a) No-EMBr

(b) EMBr

Figure 3.22 - Time-averaged velocity magnitude contours and streamlines at mold midplane for the real caster cases (a)No-EMBr (b) EMBr (All axes in meters)

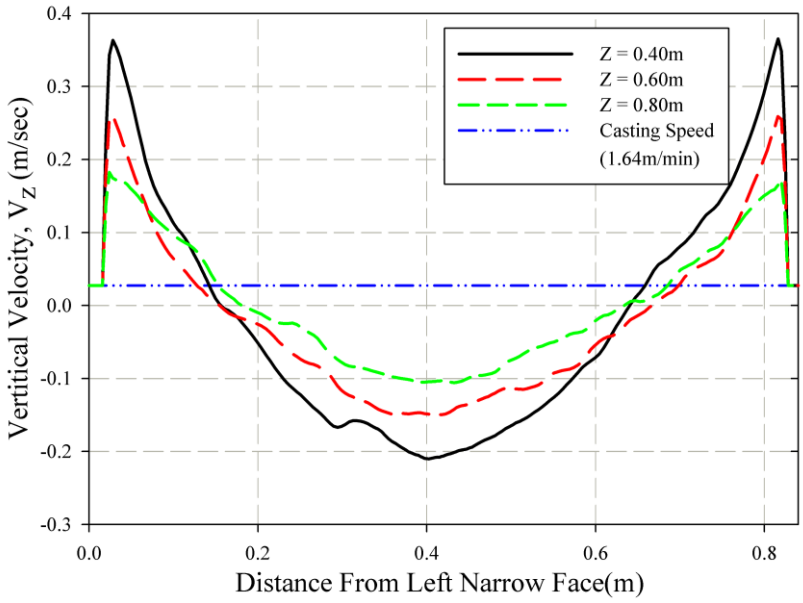

(a) No-EMBr

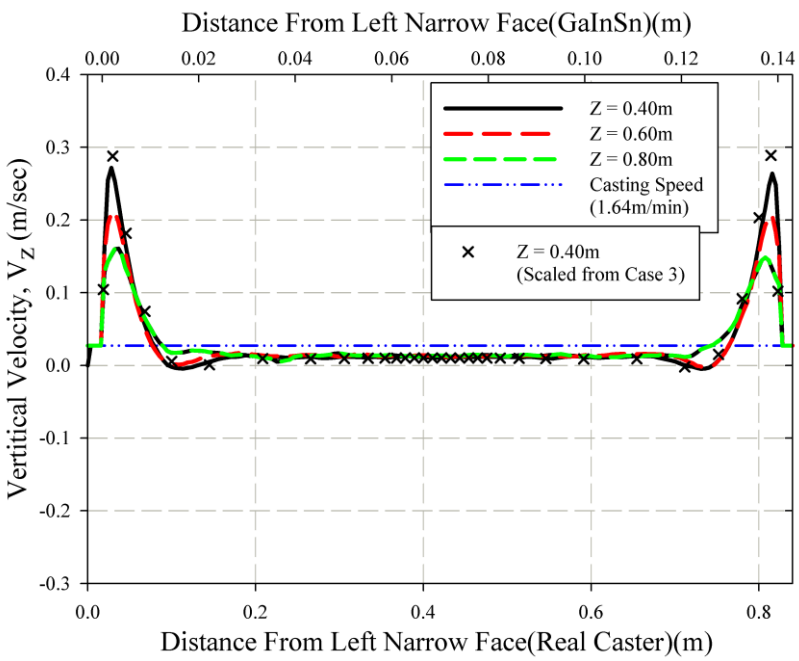

(b) EMBr

Figure 3.23 - Time-averaged vertical velocity (V_z) at three vertical locations in the midplane parallel to the mold wide face plotted against distance from narrow face
(a) real caster No-EMBr case (b) real caster EMBr case and GaInSn model EMBr with conducting-shell wall case (scaled velocity)

3.4.2.3. Surface Flow

Figure 3.24 compares the time-averaged surface velocity magnitude, 6mm below the free surface (which is six times the distance plotted for the GaInSn model) across the mold width,

for the No-EMBr and the EMBr cases. The time-averaged surface velocity magnitude towards the SEN for the EMBr case was much higher (maximum of 0.25m/s in the real caster) as compared to the No-EMBr case (maximum of 0.07m/s), due to the stronger flow up the narrow face walls. The sudden drop to zero surface speed found very close to the narrow face, for the EMBr cases, indicates a switch in the direction of the surface velocity. This is due to a small recirculating region that forms near each narrow face, due to the concave shell profile at the edge of the fluid domain.

The stability of the surface is also an important factor in determining the steel quality. Figure 3.25 shows the variation of TKE along the mold surface on the midplane between the wide faces for the No-EMBr and the EMBr case. Both cases have TKE of the same order of magnitude along the surface. The EMBr case has definite peaks of high TKE close to the narrow face (~0.005m^2/s^2) and SEN (~0.002m^2/s^2), whereas with no EMBr the variation along the width was gradual.

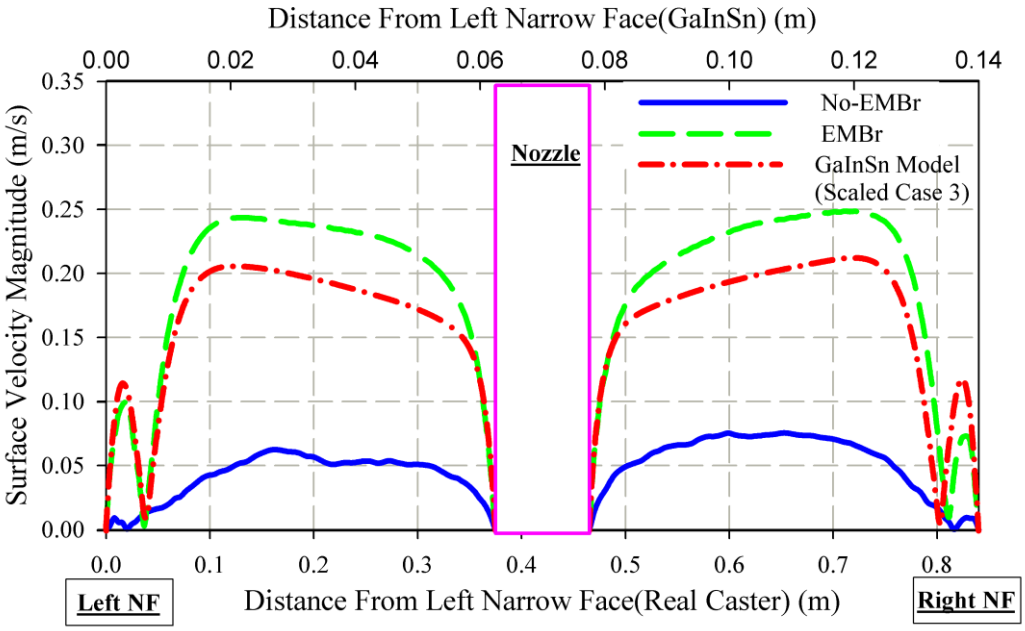

Figure 3.24 - Time-averaged horizontal velocity at the surface plotted against distance from narrow face for the real caster cases and the GaInSn model with conducting-shell wall case (scaled velocity)

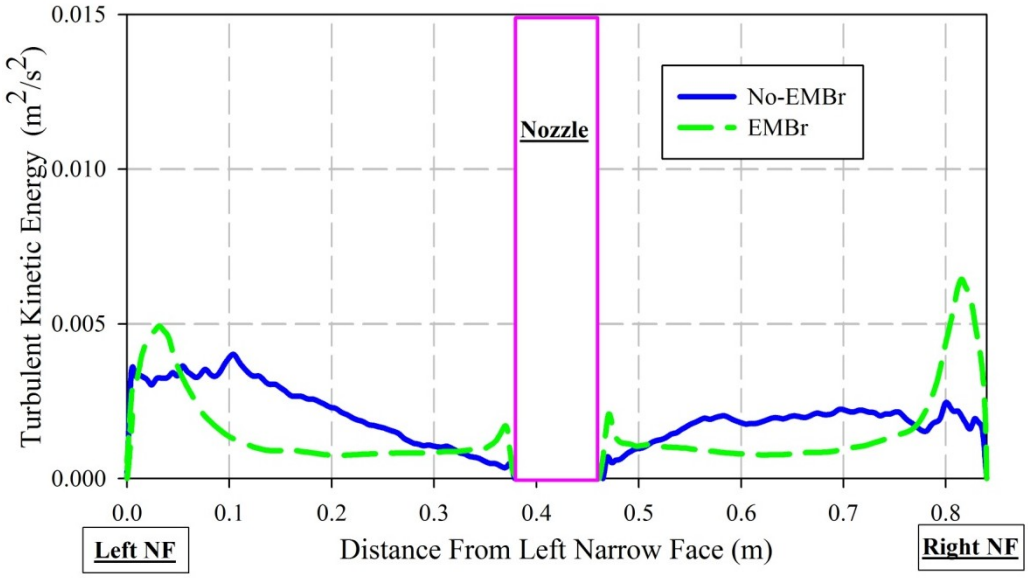

Figure 3.25 - Resolved turbulent kinetic energy at the surface plotted against distance from the left narrow face for the real caster cases

3.4.2.4. Effects of Scaling

The flow fields predicted for the 1/6 scale-model (Case 3) and the real caster (Case 5) are very similar, even though the dimensions differ greatly. The surface-level profiles could be matched using appropriate Froude-number based scaling. To further study the validity of using Stuart number similarity for scaling EMBr cases, velocities in the GaInSn model were scaled by the ratio of the characteristic velocities in the real caster and the GaInSn model (1.7/1.4=1.21, from the inlet velocities in Table 3.1). The resulting scaled vertical velocity below the jet region is shown in Figure 3.23b along one of the horizontal lines ($z = 0.40m$, $y = 0$). The variation of the vertical velocities across the width agrees well with the corresponding real caster curve after shifting and scaling the axes to accommodate for the shell thickness on the narrow faces of the real caster. Scaled surface velocities are also compared with the calculated values in the real caster and are seen to agree (Figure 3.24). The higher surface velocity in the real caster is an effect of the tapered solidifying shell. It has been shown in a previous study that the tapered shell, and the consequent reduction in cross-

section area, deflects more fluid upward into the upper recirculation region, leading to the increased surface velocity [34].

The agreement between the scaled velocities for Case 3 and the velocities for Case 5 is shown more completely also in Figure 3.26. It can be seen that both the flow patterns as well as the velocity magnitudes match well over the entire mold.

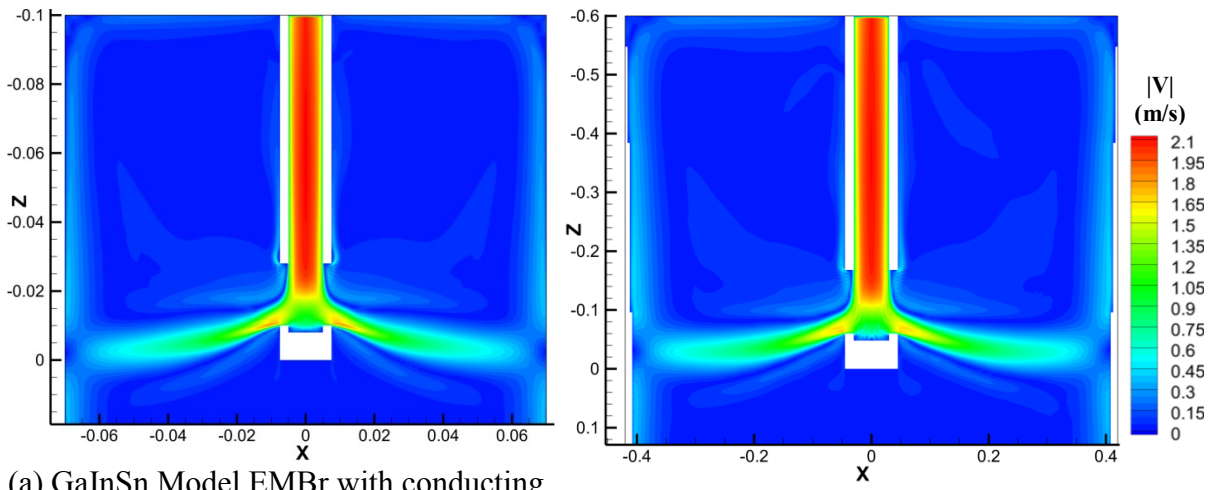

(a) GaInSn Model EMBr with conducting side walls (Scaled Velocity Magnitude)

(b) Real Caster with EMBr

Figure 3.26 - Time-averaged velocity magnitude contour on midplane between wide faces for (a) GaInSn model conducting-shell wall case with scaled velocity magnitude (b) Real caster with EMBr case (All axes in meters)

3.5. Summary and Conclusions

Large Eddy-Simulations of flow in a full-scale steel caster with the effects of a ruler magnetic field and conducting steel shell were performed. The computational approach was first validated with measurements made in a GaInSn physical model [13] and also with simulations with an insulated electrical boundary condition. The GaInSn model was then scaled to correspond with a full-sized caster and was studied at conditions similar to industrial operations. However, in order to compare the results with the GaInSn model the

submergence depth was kept proportionally the same as the GaInSn model which was deeper than typical industrial conditions.

The large-scale jet wobble and transient asymmetric flow in the mold with insulated walls was not found with conducting-shell walls. With a realistic conducting shell for otherwise identical conditions, the flow was stable and quickly achieved a symmetrical flow pattern, which featured three counter-rotating loops in the upper region and top surface flow towards the SEN. The turbulence Reynolds stresses were suppressed in the presence of the applied magnetic field. The suppression in the conducting shell case was however found to be lower in nozzle region. Also, with the conducting shell the Reynolds stresses were restricted only to the jet region in the mold. Thus, it is essential to include the effect of the conducting shell when studying transient mold flow with a magnetic field.

Relative to the case with no EMBr field, the ruler magnetic brake across the nozzle deflects the jets upwards, from approximately 30° down to only 10° down. This strengthens the flow in the upper region and increases the top surface velocity from narrow face to SEN, from 0.07m/s to 0.25 m/s in the real caster. The weaker upper recirculation region without EMBr becomes more complex with the application of the ruler magnetic brake, with three distinct recirculation loops, featuring upward flows along both the narrow face and the SEN. The momentum from these flows raises the surface level near the narrow face and SEN, and generates higher level fluctuations in these two regions. The lower recirculation region becomes a very small elongated loop just below the jet, which is similar to a small loop that forms just above the jet. Flow below this small recirculation loop aligns quickly to the casting direction. These lower downward velocities with EMBr should be beneficial for lessening the penetration and entrapment of bubbles and inclusion particles.

The Stuart number similarity criterion employed in this study enables a close match of both the time-averaged mold flow pattern (qualitative) and velocities (quantitative) between the 1/6-scale model and the real caster. The scaled surface-level profile and its time fluctuations were matched as well, when using a scaling factor based on the ratio of the Froude numbers. Simply scaling the GaInSn model predictions using the geometric scale factor of 6 resulted in an overprediction of the surface level profile and fluctuations, because the Froude number of this scaled model was larger than that of the real caster. This Froude-number based scaling method avoids the need to maintain both Froude number and Stuart number similarity conditions simultaneously when choosing operating conditions for a scaled model caster with EMBr.

3.6 References

1. World steel in figures 2012, World Steel Association, Brussels, Belgium, 2012.
2. R. Chaudhary and B.G. Thomas., "State of the art in electromagnetic flow control in continuous casting of steel slabs: Modeling and plant validation." 6th International Conference on Electromagnetic Processing of Materials EPM, 2009.
3. R. Chaudhary, B. G. Thomas, and S. P. Vanka., "Effect of electromagnetic ruler braking (EMBr) on transient turbulent flow in continuous slab casting using large eddy simulations.", *Metallurgical and Materials Transactions B*, 2012, vol. 43, pp. 532-553.
4. C. Zhang, S. Eckert, and G. Gerbeth., "The flow structure of a bubble-driven liquid-metal jet in a horizontal magnetic field.", *Journal of Fluid Mechanics*, 2012, vol. 575, pp. 57-82.
5. K. Cukierski and B.G. Thomas., "Flow control with local electromagnetic braking in continuous casting of steel slabs.", *Metallurgical and Materials Transactions B*, 2008, vol. 39, pp. 94-107.

6. D. Kim, W. Kim, and K. Cho., "Numerical simulation of the coupled turbulent flow and macroscopic solidification in continuous casting with electromagnetic brake.", *ISIJ International*, 2000, vol. 40, pp. 670-676.
7. K. Takatani, K. Nakai, N. Kasai, T. Watanabe, and H. Nakajima., "Analysis of heat transfer and fluid flow in the continuous casting mold with electromagnetic brake.", *ISIJ International*, 1989, vol. 29, pp. 1063-1068.
8. M.Y. Ha, H.G. Lee, and S.H. Seong., "Numerical simulation of three-dimensional flow, heat transfer, and solidification of steel in continuous casting mold with electromagnetic brake.", *Journal of Materials Processing Technology*, 2003, vol. 133, pp. 322-339.
9. H. Harada, T. Toh, T. Ishii, K. Kaneko, and E. Takeuchi., "Effect of magnetic field conditions on the electromagnetic braking efficiency.", *ISIJ International*, 2001, vol. 41, pp. 1236-1244.
10. B. Li, T. Okane, and T. Umeda., "Modeling of molten metal flow in a continuous casting process considering the effects of argon gas injection and static magnetic-field application.", *Metallurgical and Materials Transactions B*, 2000, vol. 31, pp. 1491-1503.
11. A. Idogawa, M. Sugizawa, S. Takeuchi, K. Sorimachi, and T. Fujii., "Control of molten steel flow in continuous casting mold by two static magnetic fields imposed on whole width.", *Materials Science and Engineering: A*, 1993, vol. 173, pp. 293-297.
12. K. Timmel, X. Miao, S. Eckert, D. Lucas, and G. Gerbeth., "Experimental and numerical modeling of the steel flow in a continuous casting mold under the influence of a transverse DC magnetic field.", *Magnetohydrodynamics*, 2010, vol. 46, pp. 437-448.

13. K. Timmel, S. Eckert, and G. Gerbeth., “Experimental investigation of the flow in a continuous-casting mold under the influence of a transverse, direct current magnetic field.”, *Metallurgical and Materials Transactions B*, 2011, vol. 42, pp. 68-80.
14. X. Miao, K. Timmel, D. Lucas, S. Ren, Z.and Eckert, and G. Gerbeth., “Effect of an electromagnetic brake on the turbulent melt flow in a continuous-casting mold.”, *Metallurgical and Materials Transactions B*, 2012, vol. 43, pp. 954-972.
15. B.G. Thomas and L. Zhang., “Mathematical modeling of fluid flow in continuous casting.”, *ISIJ International*, 2001, vol. 41, pp. 1181-1193.
16. R. Chaudhary, C. Ji, B.G. Thomas, and S.P. Vanka., “Transient turbulent flow in a liquid-metal model of continuous casting, including comparison of six different methods.”, *Metallurgical and Materials Transactions B*, 2011, vol. 42, pp. 987-1007.
17. Z. Qian, Y. Wu, B. Li, and J. He., “Numerical analysis of the influences of operational parameters on the fluid flow in mold with hybrid magnetic fields.”, *ISIJ International*, 2002, vol. 42, pp. 1259-1265.
18. R. Kageyama and J.W. Evans., “Development of a three dimensional mathematical model of the electromagnetic casting of steel.”, *ISIJ International*, 2002, vol. 42, pp. 163-170.
19. Y. Miki and S. Takeuchi., “Internal defects of continuous casting slabs caused by asymmetric unbalanced steel flow in mold.”, *ISIJ International*, 2003, vol. 43, pp. 1548-1555.
20. T. Ishii, S.S. Sazhin, and M. Makhlouf., “Numerical prediction of magnetohydrodynamic flow in continuous casting process.”, *Ironmaking & Steelmaking*, 1996, vol. 23, pp. 267-272.

21. Y.Hwang, P. Cha, Ho-Seok Nam, Ki-Hyeon Moon, and Jong-Kyu Yoon., "Numerical analysis of the influences of operational parameters on the fluid flow and meniscus shape in slab caster with EMBr.", *ISIJ International*, 1997, vol. 37, pp. 659-667.

22. P.H. Dauby., "Continuous casting: make better steel and more of it!", *International Journal of Metallurgy*, 2012, vol. 109, pp. 113-136.

23. Q. Yuan, B.G. Thomas, and S.P. Vanka., "Study of transient flow and particle transport in continuous steel caster molds: PartI- Fluid flow.", *Metallurgical and Materials Transactions B*, 2004, vol. 35, pp. 685-702.

24. R. Chaudhary, S. P. Vanka, and B. G. Thomas., "Direct numerical simulations of magnetic field effects on turbulent flow in a square duct.", *Physics of Fluids*, 2010, vol. 22, pp. 075102-15.

25. R. Chaudhary, A.F. Shinn, S.P. Vanka, and B.G. Thomas., "Direct numerical simulations of transverse and spanwise magnetic field effects on turbulent flow in a 2:1 aspect ratio rectangular duct.", *Computers & Fluids*, 2011, vol. 51, pp. 100-114.

26. H. Kobayashi., "Large eddy simulation of magnetohydrodynamic turbulent duct flows.", *Physics of Fluids*, 2008, vol. 20, pp. 015102-14.

27. R. Moreau., "Magnetohydrodynamics", Kluwer Academic Pub. Co., Norwell, MA, 1990, pp. 110-64.

28. A.F. Shinn and S.P. Vanka., "Large eddy simulations of film-cooling flows with a micro-ramp vortex generator.", *Journal of Turbomachinery*, 2013, vol. 135, pp. 011004-16.

29. A.F. Shinn., "Large eddy simulations of turbulent flows on graphics processing units: application to film-cooling flows.", PhD Thesis, University of Illinois at Urbana-Champaign, 2011.

30. J. Smagorinsky., “General circulation experiments with the primitive equations.”, Annual Weather Review, vol. 96, pp. 99-164.
31. F. Nicoud and F. Ducros, “Subgrid-scale stress modelling based on the square of the velocity gradient tensor.”, Flow, Turbulence and Combustion, 1999, vol. 62, pp. 183-200.
32. H. Kobayashi., “Large eddy simulation of magnetohydrodynamic turbulent channel flows with local subgrid-scale model based on coherent structures.”, Physics of Fluids, 2006, vol. 18, pp. 045107.
33. J. Iwasaki and B.G. Thomas., “Thermal-mechanical model calibration with breakout shell measurements in continuous steel slab casting”, Supplemental Proceedings, John Wiley & Sons, Inc., 2012, pp. 355-362.
34. R. Chaudhary, B.T. Rietow, and B.G. Thomas., “Differences between physical water models and steel continuous casters: A theoretical evaluation.”, Inclusions in Clean Steel, Mater. Sci. Technol., AIST/TMS, Pittsburgh, PA, 2009, pp. 1090-1101.
35. H. Werner and H. Wengle., “Large-eddy simulation of turbulent flow over and around a cube in a plate channel.”, 8th Symposium on Turbulent Shear Flows, 1991, pp. 155-168.
36. Anatoliy Vorobev, Oleg Zikanov, Peter A. Davidson, and Bernard Knaepen., “Anisotropy of magnetohydrodynamic turbulence at low magnetic reynolds number.”, Physics of Fluids, 2005, vol. 17, pp. 125105-16.

CHAPTER 4- LARGE EDDY SIMULATIONS OF A REAL CONTINUOUS CASTER MOLD AND EFFECTS OF A FC-MOLD ELECTROMAGNETIC BRAKING (EMBr)

4.1 Introduction

Having validated CUFLOW and studied the scaled model caster in detail in Chapter 3 we now apply the model to study the mold flow of a real caster. This study is conducted without and with an applied EMBr field at industrial operating conditions. Ideally the understanding of the mold flow in industrial casters could be developed by conducting experiments However, this is very difficult due to the high temperature of the molten steel and the incapability of conventional equipment to measure flow quantities through the bulky and opaque mold setup and through the opaque slag layer.

As discussed earlier, surface flow in the mold is extremely important to steel quality as it results in various defects such as meniscus freezing, slag entrainment and defects due to balding of the slag layer [1,2] which causes exposure of molten steel to air. The top surface is also the only region which is accessible for measurements with suitable techniques. Over the years, various methods have been devised to measure surface quantities. Iguchii et al. [3-5] devised a Karman vortex probe which was used to estimate surface velocities by calculating the Karman vortex shedding frequency. Argyropoulos et al. [6,7] estimated surface velocities by calculating the time needed to melt a metal ball in the molten steel. These metal balls were imbedded with sensing wires in the center and the surface velocities were calculated using empirical relations based on the melting time and the superheat of the molten steel. Some simpler techniques include Sub-meniscus Velocity Control (SVC) [8,9] and a similar method developed by Kubota et al. [10]. These methods use a rod dipped into the molten steel surface. The torque and deflection induced on this rod due to the steel flow is measured and

then used to calculate the surface velocities. Another simple technique for studying interface behavior is performed by dipping a nail into the free surface of the mold for 3-5 seconds and analyzing the steel lump which solidifies on the nail. This method was devised by Dauby et al. [11] and has been developed by Thomas et al. [12-14] to predict surface velocity. This method could be used with a single nail or an array of nails to get an instantaneous snapshot of the surface flowfield.

Most of the above mentioned plant experimental techniques are difficult and/or expensive, provide information about only the surface behavior and are prone to experimental errors. Alternative methods to study the mold flow region include using physical models [15-20] and numerical models [13-18,20-32]. Physical models usually have water as the working fluid. However conducting working fluids, such as Mercury [15,17], Tin [16] and GaInSn [18-20], are used if effects of applied magnetic fields are considered. Similitude analysis is performed to establish operating conditions analogous to the corresponding real caster. Though physical models are an effective way to study flow in a continuous casting mold; they are still limited by the capital intensive nature as every real caster requires its own physical model and also by the difficulty in taking measurements.

Over the years, with advancements in computational power and lowering of the costs, numerical studies have become popular. Most numerical studies used averaged models, such as Reynolds Averaged Navier-Stokes (RANS) [13,14,16,17,23,24,30,31] or Unsteady RANS (URANS) [18,20,26], which accurately predict the time-averaged flowfield. However, defect formation and entrapment are more dependent on the transient behavior of the flow [33]. Large Eddy Simulation (LES) method resolves the transient details of a flow and can also predict the time-averaged flowfields. LES has been used in some previous studies of the mold flow phenomena [21,26-29,32]. In recent studies [21,26,34,Ch. 3] we have validated our in-house developed finite volume solver, CUFLOW, with measurements from GaInSn scaled

physical model in the presence of applied magnetic fields and then used CUFLOW to study the effects of other configurations of the applied magnetic fields. CUFLOW has also been previously validated for other canonical flows without [35] and with applied magnetic fields [36,37].

The present chapter focuses on understanding the mold flow in a real operational caster. LES are performed using CUFLOW of the mold flow in the commercial caster. Two simulations were performed in the present study. The first one without any applied magnetic field and the second one with an applied "Flow-Control-mold" or "FC-mold" EMBr magnetic field configuration [16,17,21,29,]. The FC-mold configuration involves two rulers, one positioned across the mold near the meniscus and the other one placed on or below the nozzle ports, which can be adjusted independently. The magnetic field applied here is adopted from the work of Idogawa et al. [17] where they study the effect of this Electro-Magnetic Braking (EMBr) configuration by numerical simulations using experiemnts with a scaled mercury physical model, Reynolds Averaged Navier-Stokes (RANS) model and experiments in a real caster. In this study, we look at the transient and time-averaged behavior to compare both cases in detail. Detailed comparisons of surface velocities, surface flow patterns, surface level profiles, surface level fluctuations, mold flow patterns and Reynolds stresses are presented. Nail board measurements were also taken at the commercial caster, without any applied magnetic field, and are compared with the calculated results.

4.2 Computational Model

4.2.1. Computational Domain, Mesh and Boundary Conditions

The computational domain for the present study included both the liquid region, shown in Figure 4.1, and a separate region consisting of the solidifying shell, which was initialized to move with the casting speed (Table 4.1) in the casting direction. The liquid portion of the domain includes the Upper Tundish Nozzle (UTN), the slide gate, the Submerged Entry

Nozzle (SEN) and the mold. The slide gate, with movement parallel to the narrow face (NF), is used as the flow control mechanism in the commercial plant. The position of the slide gate was 41.48 % open (36.5mm opening), which was calculated according to the liquid steel throughput rate, nozzle geometry, tundish height and argon gas injection rate using a model, based on Bernoulli's equation and empirical relations, developed by Liu and Thomas [38].

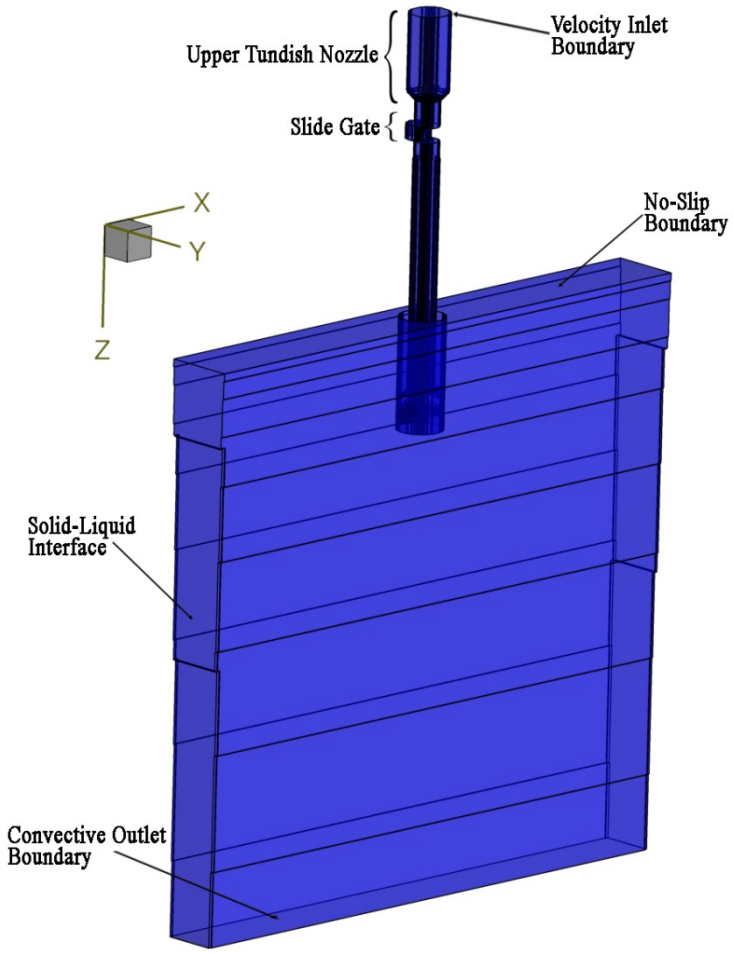

Figure 4.1- Isometric view of the computational domain (fluid flow region) with boundary conditions

The shell thickness s at any given location below the meniscus was calculated from $s = k\sqrt{t}$, where t is the time taken by the shell to travel the given distance and the constant $k(= 2.75)$ was chosen to match the steady-state shell profile predicted from break-out shell measurements by Iwasaki et al [39]. An FC-mold or double-ruler EMBr configuration was applied with the maximum strength of the upper ruler and lower ruler fields occurring 60 mm

and 560 mm below the free surface respectively. Figure 4.2 shows a contour plot of the applied magnetic field and Figure 4.3 shows the variation of the applied magnetic field in the casting direction. The field is uniform in the width and thickness directions of the caster with variation only in the casting direction. Both rulers have only one non-zero magnetic field component, which is parallel to the Y-direction, but with opposite orientation. A Cartesian mesh was used in this study with 5.5 million finite volume cells. In order to generate the caster geometry, first a rectangular domain was meshed with 8.9 million cells and then solid

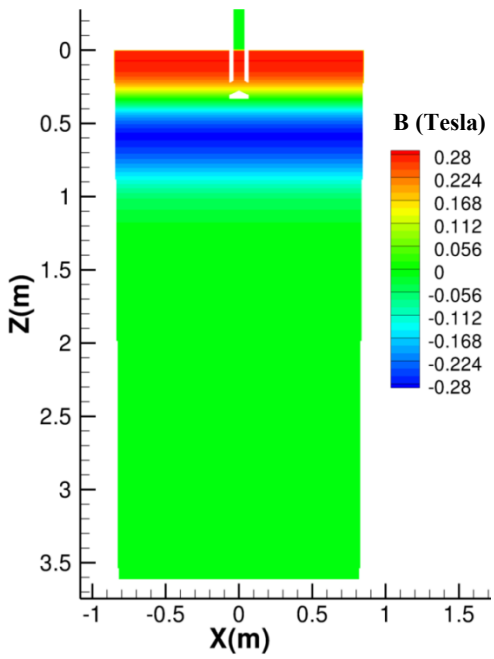

Figure 4.2- Contour plot of the applied magnetic field

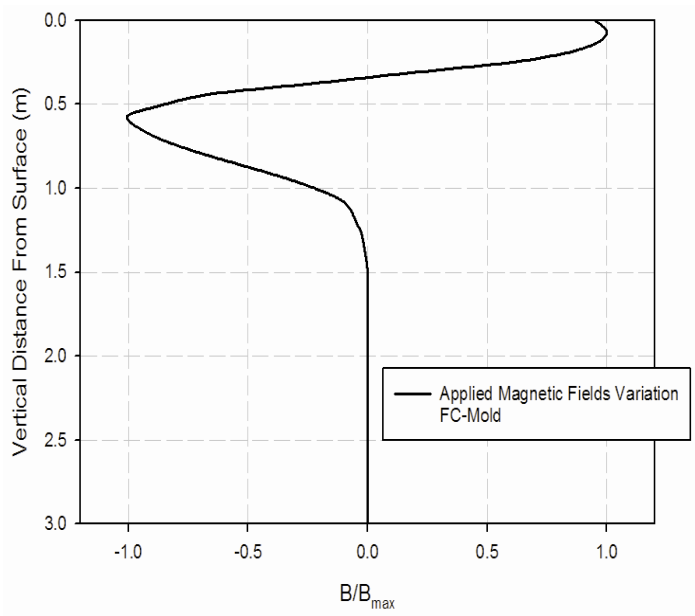

Figure 4.3 Variation of applied magnetic field in the casting direction (Z) with B_{max}=0.28 Tesla in the EMBr case

regions were blocked out. Fixed velocity boundary was applied at the inlet of the UTN and was initialized with a uniform velocity of 0.752 m/s, which was calculated based on the casting speed. A no-slip boundary condition was applied on the top surface to approximately model the effects of the high viscosity slag on slowing down the steel/slag interface at the top surface [40]. A convective boundary condition was applied to the outlet of the caster for all three velocity components according to Equation 4.1.

$$\frac{\partial u_i}{\partial t} + U_{convective}\frac{\partial u_i}{\partial n} = 0 \qquad i = 1,2,3 \tag{4.1}$$

Here $U_{convective}$ is the average normal velocity across outlet plane and n is the direction normal to the outlet plane. It is implemented as described previously. The solidifying shell was initialized with fixed downward vertical velocity equal to the casting speed, which causes liquid to leave the liquid domain to account for both mass transfer and momentum transfer from the fluid region to the solidifying shell. All other boundaries were solid walls and the wall treatment previously reported by Werner and Wengle [41]. The fluid flow equations were solved only in the fluid domain and the MHD equations were solved in the

Table 4.1: Process Parameters

	Real Caster
Volume flow rate | nozzle bulk inlet velocity (at UTN)	8.1 L/s | 1.7m/s
Casting speed	1.4 m/min
Mold width	1706.0 mm
Mold thickness	203.2 mm
Mold length in computational domain	3600.0 mm
Nozzle port diameter	75.0 mm
Nozzle bore diameter($inner \mid outer$)	70 mm | 125 mm
SEN submergence depth (liquid surface to top of port)	220 mm
Thickness of shell on the wide faces	$s(mm) = 2.75\sqrt{t(s)}$
Thickness of shell on the narrow faces	$s(mm) = 2.75\sqrt{t(s)}$
Fluid material	Molten steel
Viscosity	$0.86\times10^{-6} m^2/s$
Fluid density	$7000 Kg/m^3$
Conductivity of liquid (σ_{liquid})	$0.714\times10^6 1/\Omega m$
Conductivity of walls (σ_{wall})	$0.787\times10^6 1/\Omega m$
Nozzle port angle	25.0 deg
Gas injection	No
Reynolds number (Re, based on nozzle diameter)	113,953
Hartmann number (Ha= $BL\sqrt{\sigma/\rho\nu}$, based on mold width)	5,202
Froude number (Fr= $U/\sqrt{gL}$), based on mold width)	0.342
Stuart number (N= $B_0^2 L\sigma/\rho U$), based on mold width)	9.74
Cases	1. No-EMBr 2. EMBr (FC-Mold configuration)

entire computational domain, including the shell. Insulated electrical boundary condition $\left(\frac{\partial \phi}{\partial n} = 0\right)$ was applied on the outer-most boundary of the computational domain to simulate the non-conducting mold slag layer.

4.2.2. Computational Details and Cost

Simulations for both cases, No-EMBr and EMBr, were started from a zero initial velocity. The flowfields were allowed to develop for 10 seconds (200,000 time steps) and 20 seconds (400,000 time steps) for the No-EMBr and EMBr cases respectively before collecting the time-averages. Time-averages were stabilized for 5 seconds in both cases after which the turbulence statistics were collected for 20 seconds and 15 seconds for the No-EMBr and EMBr cases respectively. The computational expense of the EMBr case was nearly twice of the No-EMBr case as it requires the solution of the electric Poisson equation (EPE). The 35 seconds of simulation without the magnetic field required a total of 15 days of calendar computation time. Whereas, the 40 seconds of simulation with the magnetic field took 34 days.

4.3 Results

4.3.1 Transient results

4.3.1.1 Mold Flow

Mold flow patterns are dependent on the condition of the jet entering the mold cavity which is a function of the mold dimensions, casting speed, SEN type, port dimensions, submergence depth, the amount of injected argon gas and electromagnetic forces. There are two extremes in the slab caster mold flow pattern which are known as “single-roll” and “double-roll” flow patterns [42]. If the jet reaches the free surface before reaching the narrow face a “single-roll” flow pattern is generated. On the other hand if the jet impinges on the narrow face, deflects and then reaches the free surface a “double-roll” flow pattern is generated. However, more

complicated flow patterns have been observed in the presence of applied magnetic fields [34]. Figure 4.4a shows the instantaneous contours of velocity magnitude in the mold region for the No-EMBr case. A typical "double-roll" pattern is observed with the lower roll penetrating deep into the mold. Comparing the instantaneous snapshots for the No-EMBr case it can be clearly seen that unbalanced flow occurs with transient asymmetries that alternate between the two halves. This transient unbalanced flow seen in this case is not due to any geometric asymmetry. Displacement of the slide gate parallel to the wide faces results in a stationary unbalanced flow [43,44], but in the present study, the slide gate is displaced parallel to the narrow faces. This unbalanced flow could be due the mountain-bottom nozzle which creates a thin jet with strong low-frequency fluctuations [45]. Unbalanced flow is detrimental to the steel quality as it may result in the creation of more inclusions by various mechanisms such as top surface fluctuations, vortex formation, upward flow impinging on the top surface and slag crawling [2]. Unbalanced flow may also increase the penetration depth of inclusions and bubbles [29]. The application of the EMBr field suppresses the small scales of turbulence and also suppresses the long time scale transient in the mold as shown in Figure 4.4b. The flow is stable and the large velocities, seen in the No-EMBr case mold flow, are damped which results in weaker upper and lower rolls.

4.3.1.2 Surface Flow

Flow past bluff bodies results in vortex shedding which forms a Kármánn vortex street. This phenomenon may occur at the SEN if an unbalanced flow is observed in the mold [46,47]. These vortices at the surface if accompanied by downward flow can result in a funnel of molten slag into the molten steel. However, the creation of these slag funnels does not necessarily result in entrainment of slag particles. If the height of this funnel is large enough to reach the jet region, the funnel breaks apart resulting in entrainment [47,48]. In a double-

roll flow pattern any unbalanced flow leads to vortex formation near the SEN where there is significant downward flow making it ideal for the formation of the liquid-slag funnel [49,50].

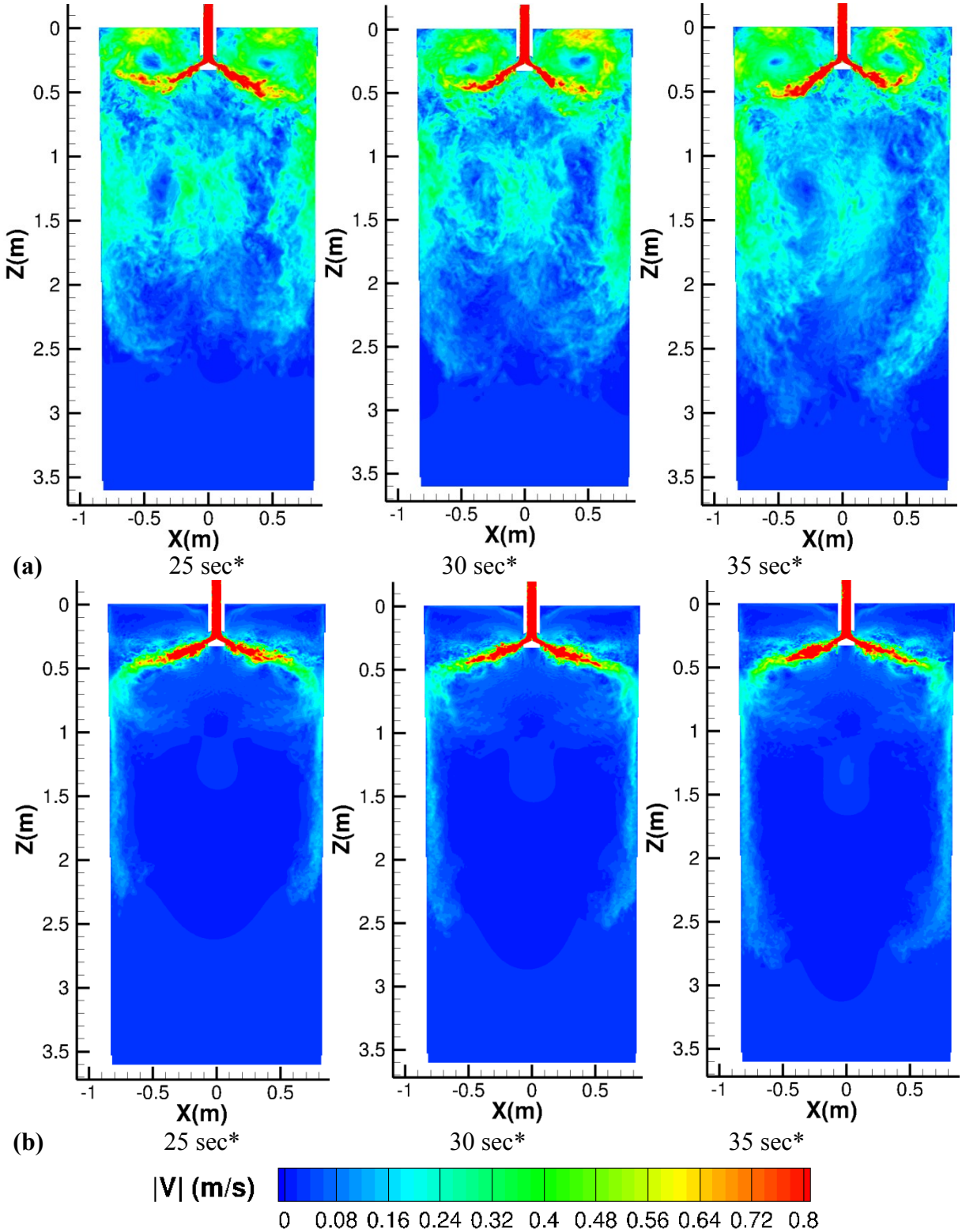

Figure 4.4 Contour plots of instantaneous velocity magnitude for (a) No-EMBr case and (b) EMBr case (*Time from start of simulation)

Figure 4.5 shows four instantaneous snapshots of the contours of velocity magnitude with vectors on the surface for the No-EMBr and EMBr cases. The unbalanced flow in the No-EMBr case can be visualized in the snapshots plotted 30 seconds after the start of the simulations, with the right side having stronger surface flow. This biased flow across the SEN leads to vortex shedding, with two strong vortices on the left of the SEN, as seen in the No-EMBr snapshot at 35 seconds. This pair of vortices survived for approximately 6 seconds of simulation time. The instantaneous plots for the EMBr case indicate no unbalanced flow in the mold. The surface velocities are smaller (Note: Contour scale range and magnitude of reference vector are scaled to a fifth for the EMBr case plots) and minimal turbulent fluctuations are present on the surface as compared to the No-EMBr case. The flow is mostly directed from the NF to the SEN, except close the SEN, which indicates the formation of small recirculation regions.

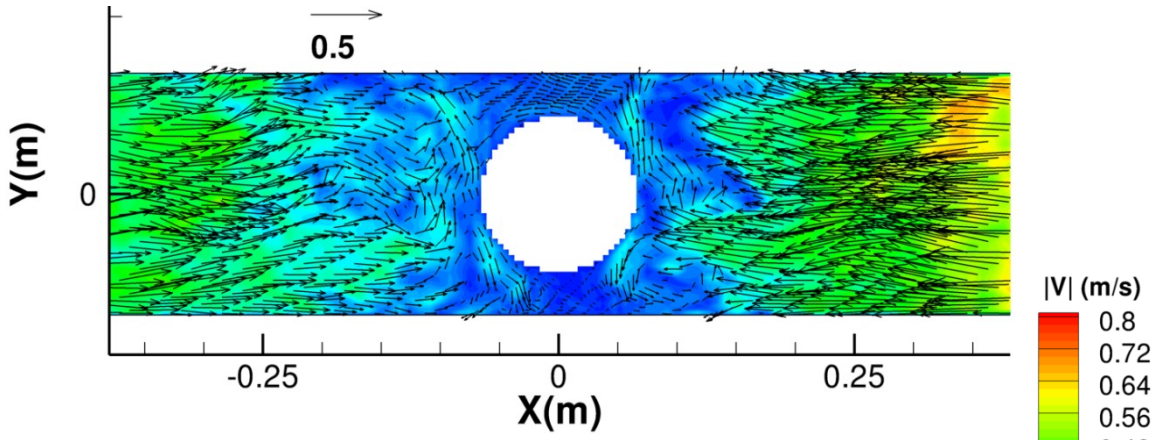

30 sec*

(a)

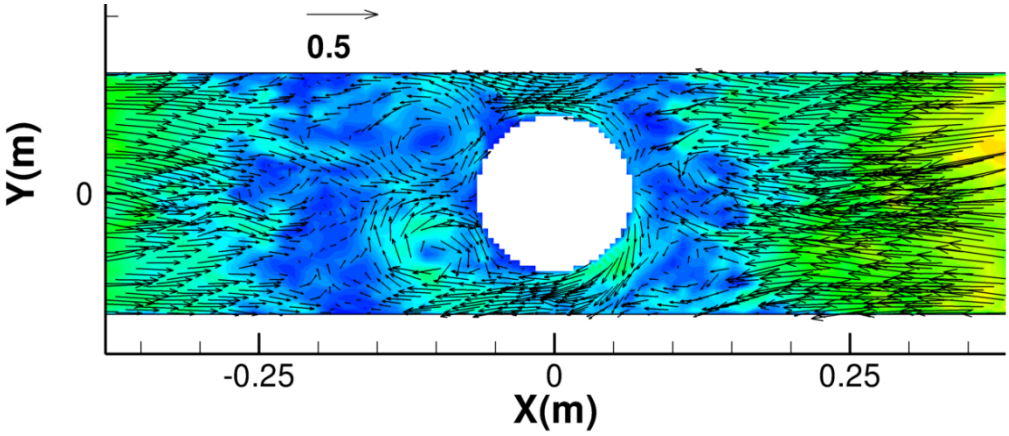

35 sec*

Figure 4.5 Contd.

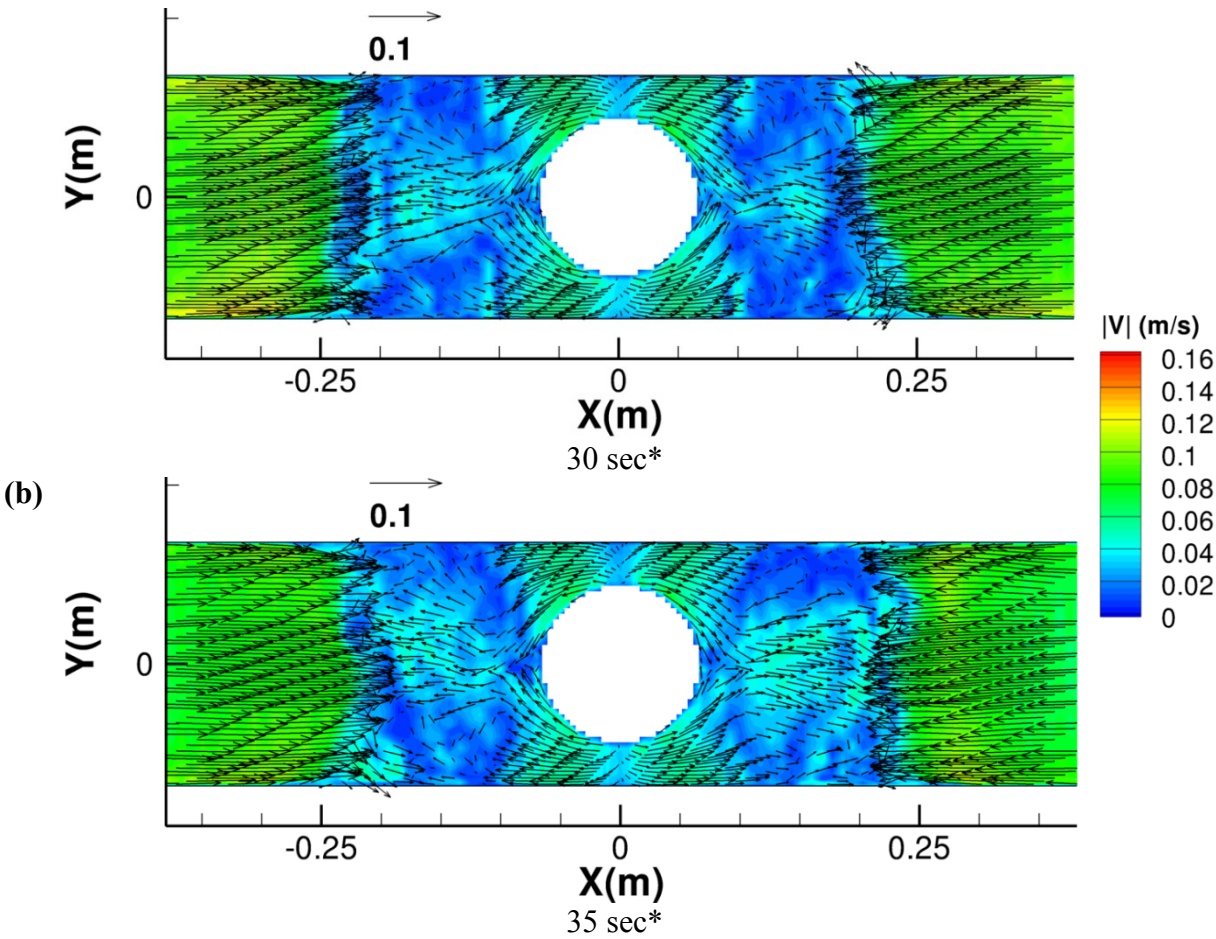

Figure 4.5 Contours of velocity magnitude with vectors, of V_x and V_y, 10mm from the top surface (*Time from start of the simulation, 90% of vectors skipped for clarity)

In order to visualize if these vortices are present in the No-EMBr case, which may result in the molten-slag funnels, streamlines of instantaneous velocity were plotted 35 seconds after the start of the simulation as shown in Figure 4.6. The streamlines on the surface for the No-EMBr case are seen to be drawn to these vortices, sucked down by the downward flow and swirl into the jet region. In contrast, in the case with the EMBr the streamlines do not exhibit any such flow behavior. Thus, the No-EMBr case is more susceptible to the formation of the molten-slag funnels, and likely experiences more slag entrainment as a consequence.

Another mechanism for defect formation in the mold is due to the instability of the standing wave [2]. The standing wave is created by the flow beneath the free surface and may become unstable if the local slope becomes too high [51]. In the present study the surface level profile

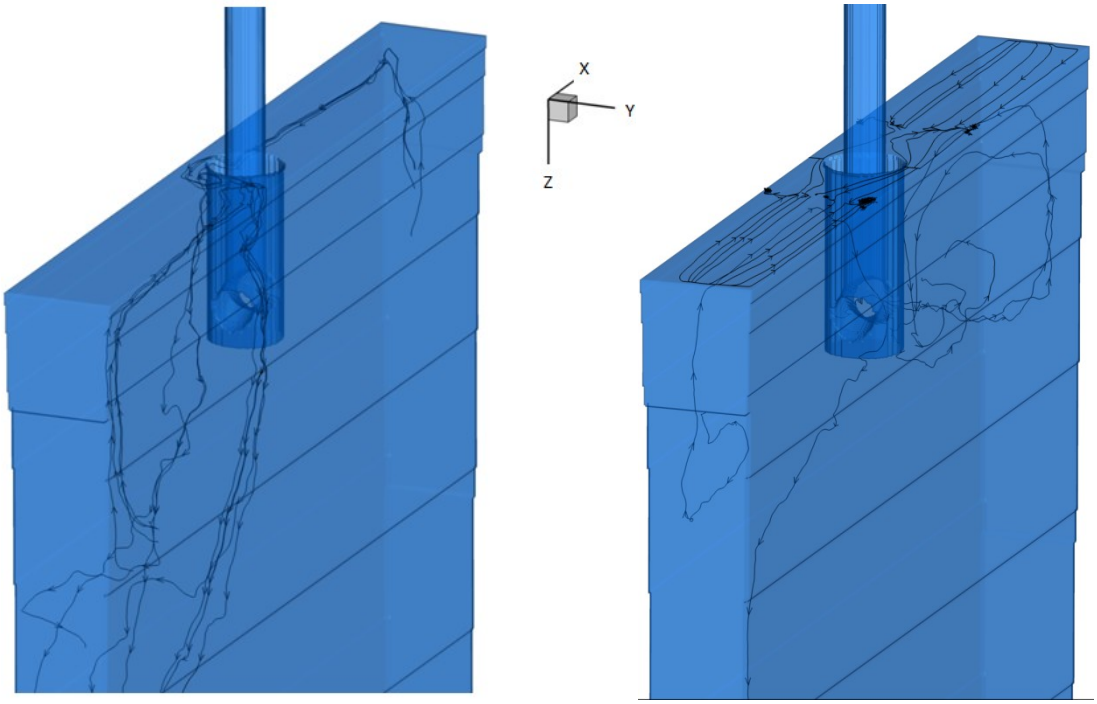

(a) (b)

Figure 4.6 Streamlines of velocity for the (a) No-EMBr case and (b) EMBr case

is approximated using the pressure method shown in Equation 4.2 [34] which gives an estimate of the liquid surface variation using a potential energy balance.

$$Z_{sur} = \frac{p - p_{mean}}{\rho_{steel}\, g} \tag{4.2}$$

The average pressure (p_{mean}) in the current study was calculated on the horizontal line along the top surface on midplane between the wide faces with g taken as $9.81 m/s^2$. Figure 4.7 shows three typical instantaneous surface level profiles, with a one second moving time average, at three instances separated by 5 seconds each. The No-EMBr case has relatively high level variations across the mold width with the difference between the peak and the trough ranging from 10 mm to 21 mm. High levels are found near the NF and the SEN, with the level at the NF usually being higher. The elevated level at the NF is due to the high vertical velocity rising along the NF, whereas the high levels at the SEN are due to the surface velocities impinging on the SEN outer walls. The application of EMBr almost flattens

the surface level with the maximum difference in the peak and trough being only ~1.5 mm. The other noticeable difference is that in the No-EMBr case the trough occurs midway between the NF and the SEN, whereas in the EMBr case the trough occurs close to the SEN outer walls.

(a)

(b)

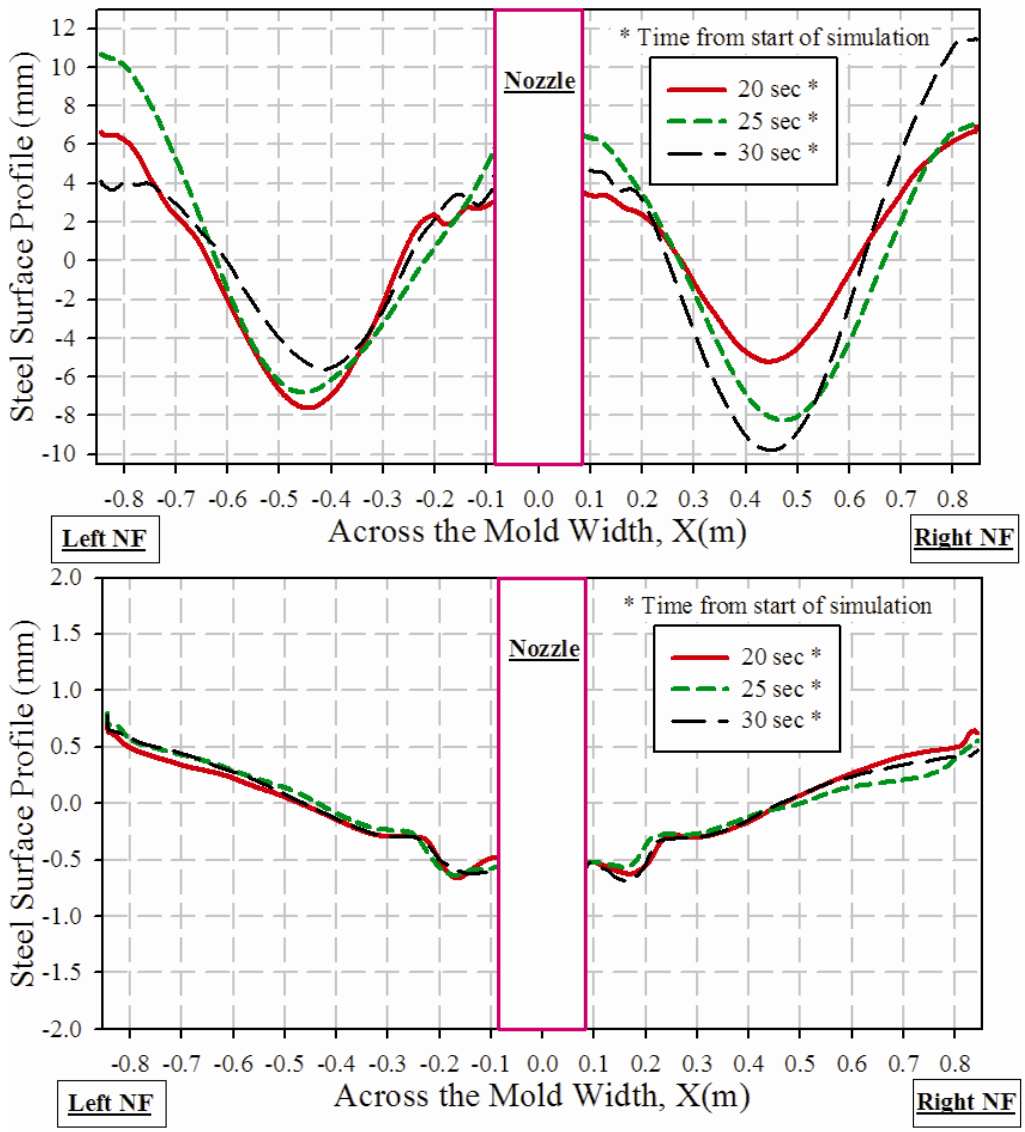

Figure 4.7 Surface level profiles at three instances for (a)No-EMBr case and (b) EMBr case

Excessive surface level fluctuation is also detrimental to the steel quality as it may expose the dendritic solidifying shell to the slag layer which causes entrainment [52]. The level fluctuations in the present study were calculated using the same pressure method given by Equation 4.2. The time histories of fluctuations were calculated at two typical points. The

first one was located close to midway between the NF and the SEN (P1) and the second one was located close to the NF (P2). At both locations for the No-EMBr case there are appreciable turbulent small scales present and also large scale fluctuations with maximum amplitudes of approximately 10 mm. Both small and large scale fluctuations are suppressed by the application of the FC-Mold EMBr, resulting in a stable surface behavior.

(a)

(b)

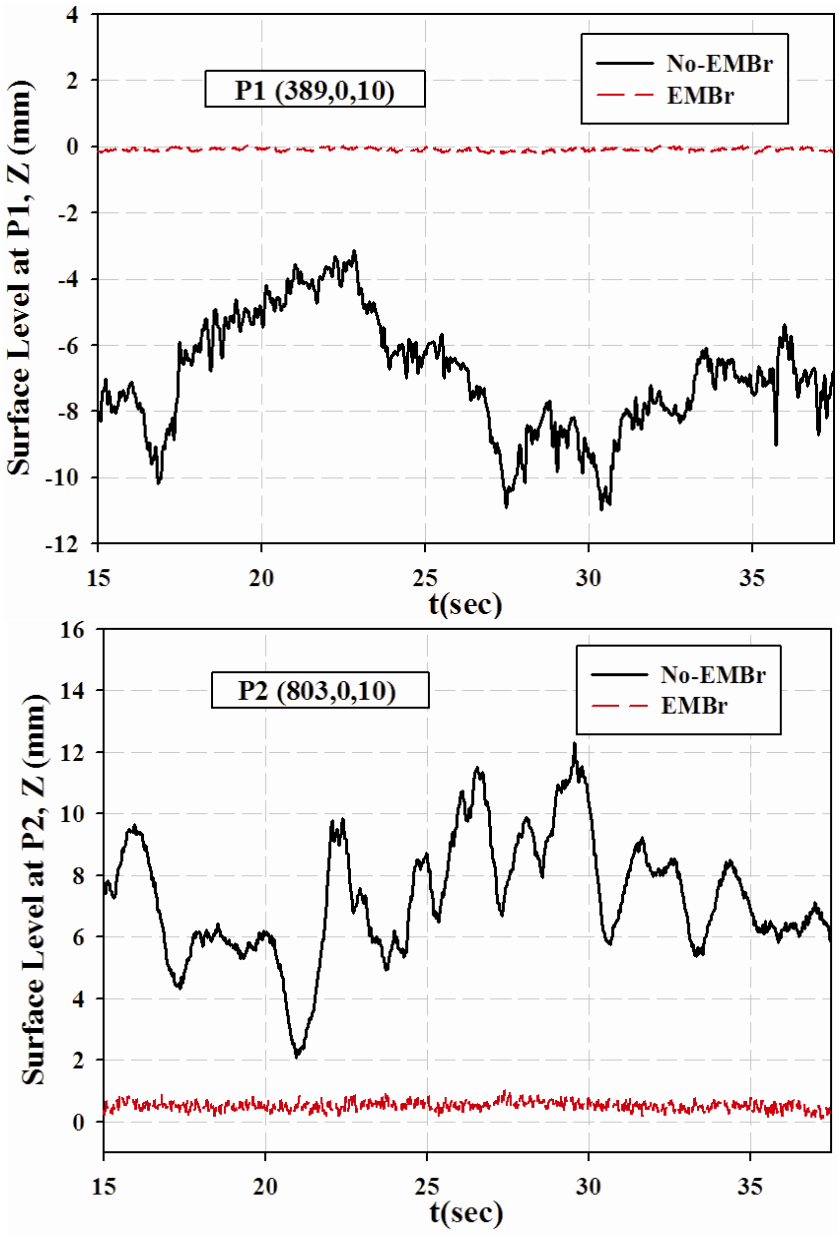

Figure 4.8 Time history of surface level fluctuations at points close to (a) midway between the narrow face and SEN, P1(389mm,0,10mm) (b) narrow face, P2(803mm,0,10mm)

4.3.2 Time Averaged Results

4.3.2.1 Mold Flow

Figure 4.9 shows the contours of time-averaged velocity magnitude in the mold region and the streamlines for the No-EMBr and the EMBe cases. The No-EMBr case has a typical double-roll flow pattern, with the lower roll penetrating deep into the mold as mentioned earlier. The flowfield is almost symmetric after 25 seconds of averaging with slight asymmetry in the lower roll indicating presence of low velocities and long-time transients. The flowfield becomes more complicated with the application of the FC-Mold EMBr. The velocities in the jet and the upper roll region are lower as compared to the No-EMBr case flowfield. There are two strong recirculation zones just above and below the jet which have

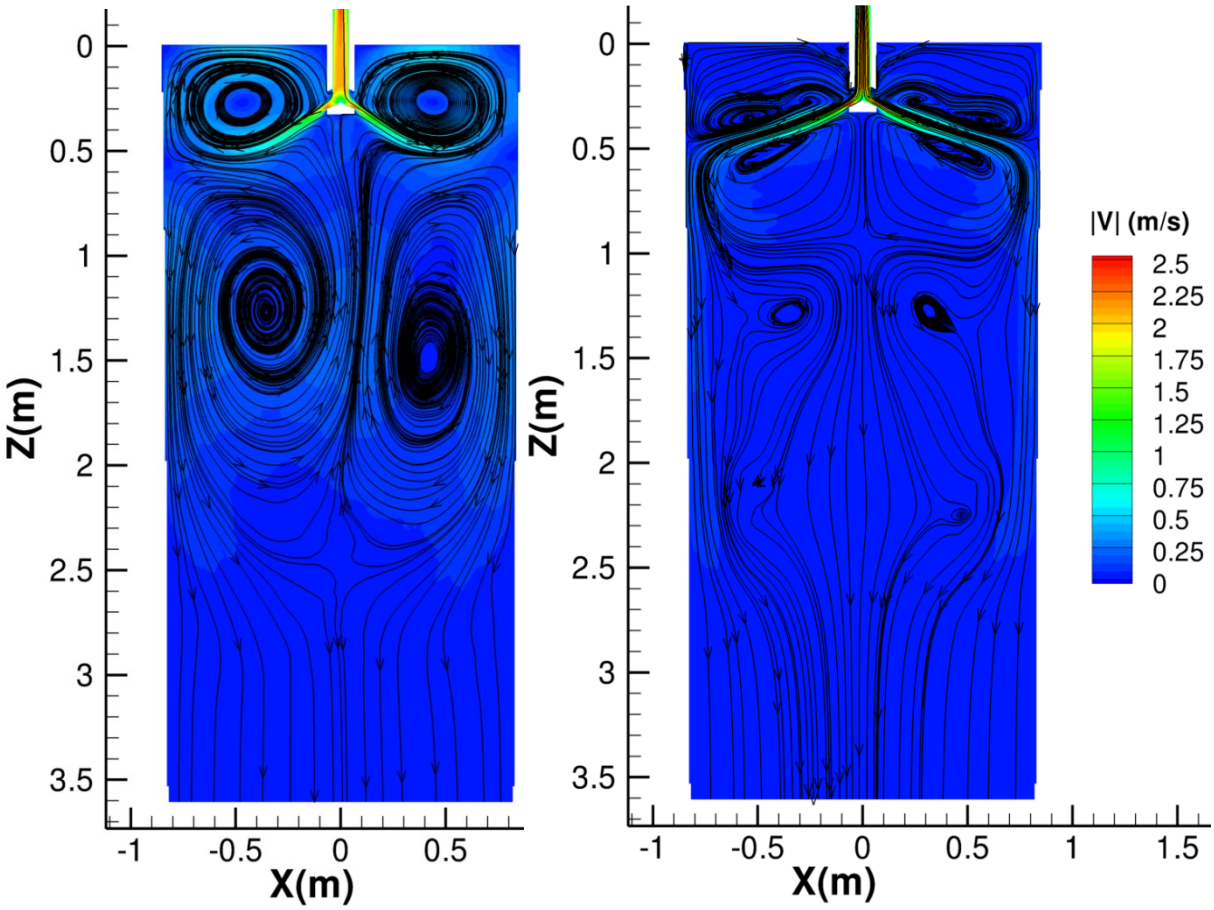

(a) (b)

Figure 4.9 Contour plot of time-averaged velocity magnitude in the mold region with streamlines (a) No-EMBr (b) EMBr

also been observed in a previous study of mold flow with conducting shell [Ch. 3, 34]. Below the lower recirculation zone the flow is mostly aligned to the casting direction with the exception of two small recirculation regions. In the previous study [34] these small recirculation regions were not present as they were damped by the applied magnetic field extending all the way to the mold outlet. However, in the present study the applied magnetic field reduces to zero at approximately 1.5 m from the top surface.

Large vertical velocities below the jet region increase the penetration depth and the chances of bubbles and inclusions being captured in the solidified steel. Figure 4.10 and Figure 4.11 show the variation of time-averaged vertical velocities across the width of the mold on midplane between the side faces (Y=0.0m) and thickness of the mold close to the left NF (X=-0.8m) respectively, at various vertical locations, for both the No-EMBr and EMBr cases. The No-EMBr case has a high downward velocity close to the NF which decreases towards the center of the mold and changes directions approximately midway between the mold center and the NF. The detrimental feature in the No-EMBr case is that the downward velocity close to the NF remains high even at 1.6m from the free surface. The EMBr case has a lower downward velocity close to the NF and these values further decrease with distance from the free surface. Another notable feature observed in both cases in that the vertical velocities reduce to the casting speed and align with the casting direction as we move deeper into the mold. The vertical velocity at Z=3.0m below the free surface almost aligns with the reference line for casting speed. This is because deep into the strand, the flow takes a long time to develop, especially in the No-EMBr case, and thus is not representative of the stationary time-average. Whereas the simulations were performed for the time required to collect statistics in the reigions close to the jet only. Similar behavior is also seen in Figure 4.11 where the variation of time-averaged vertical velocity is plotted against the mold thickness close to the NF (X=-0.8m).

(a)

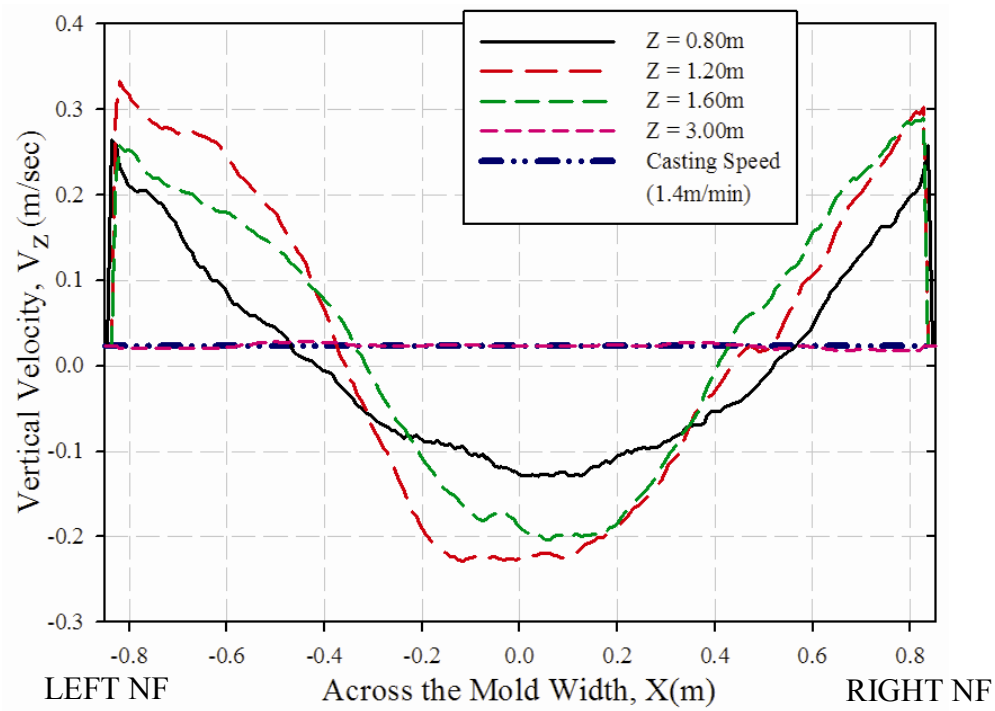

(b)

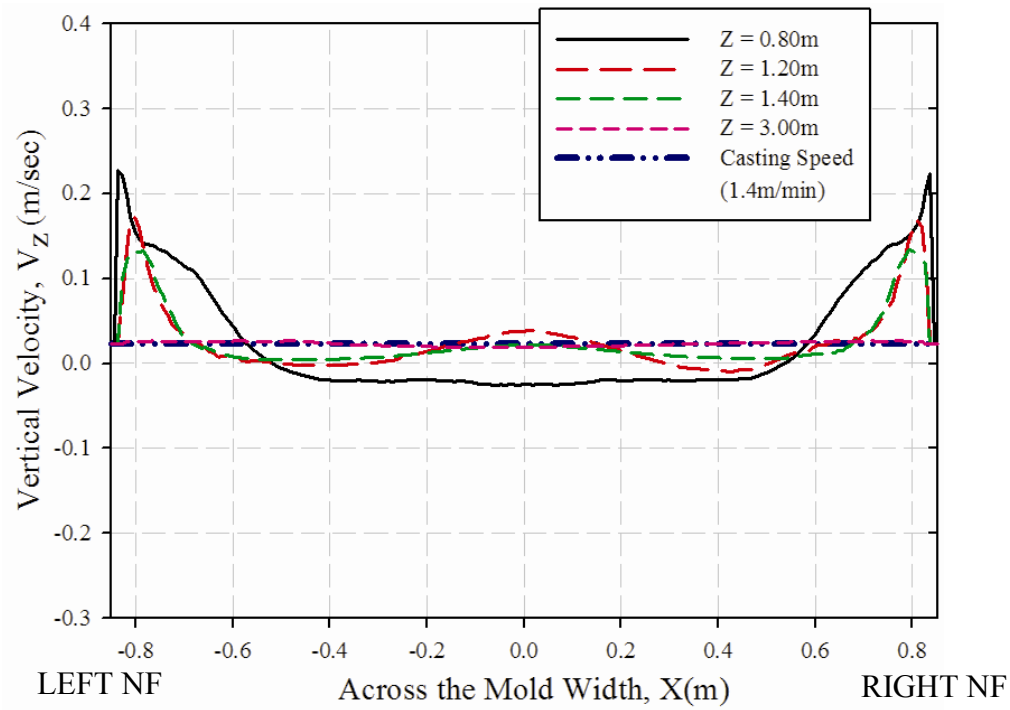

Figure 4.10 Time-averaged vertical velocity (V_z) at four vertical locations in the midplane parallel to the mold wide face plotted across the mold width for (a) No-EMBr case and (b) EMBr case

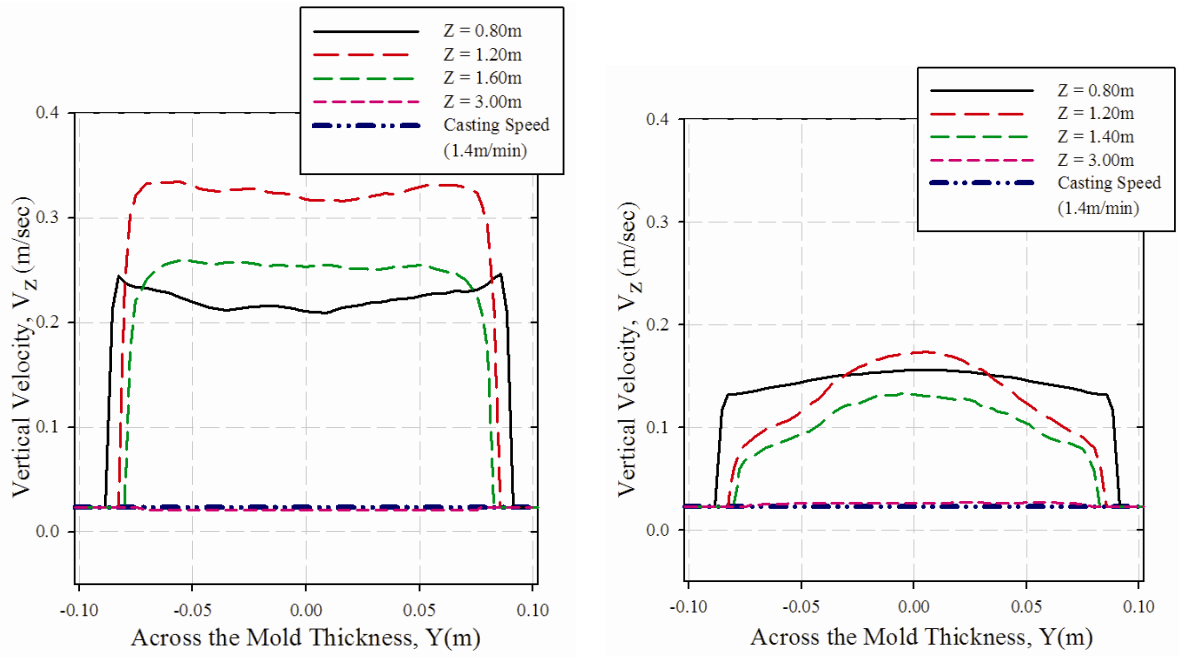

(a) (b)

Figure 4.11 Time-averaged vertical velocity (V_z) at four vertical locations in the midplane parallel to the mold wide face plotted across the mold thickness at X=-0.8m for (a) No-EMBr case and (b) EMBr case

The effect of the applied magnetic field on the turbulence can be understood by studying the time-averaged Reynolds stresses of the flow. Figure 4.12 shows contour plots of the normal components of the time-averaged Reynolds stresses and the Turbulent Kinetic Energy (TKE). Magnetic fields are known to suppress the turbulence in the flow of a conducting material [53] and this effect is seen in this study. The fluctuating quantities in the No-EMBr case are seen to extend along the jet, deep into the upper roll of the mold. Whereas, the application of the EMBr field suppresses the turbulent fluctuations and restricts the Reynolds stresses only to the jet region near the port exits. The $\overline{u'u'}$ and the TKE values are relatively high at the surface for the No-EMBr case as compared to the EMBr case. The FC-Mold EMBr configuration used in this study applies a weak magnetic field at the nozzle ports and thus the contours of these time-averaged fluctuating quantities look very similar in and around the port region of the mold in both cases.

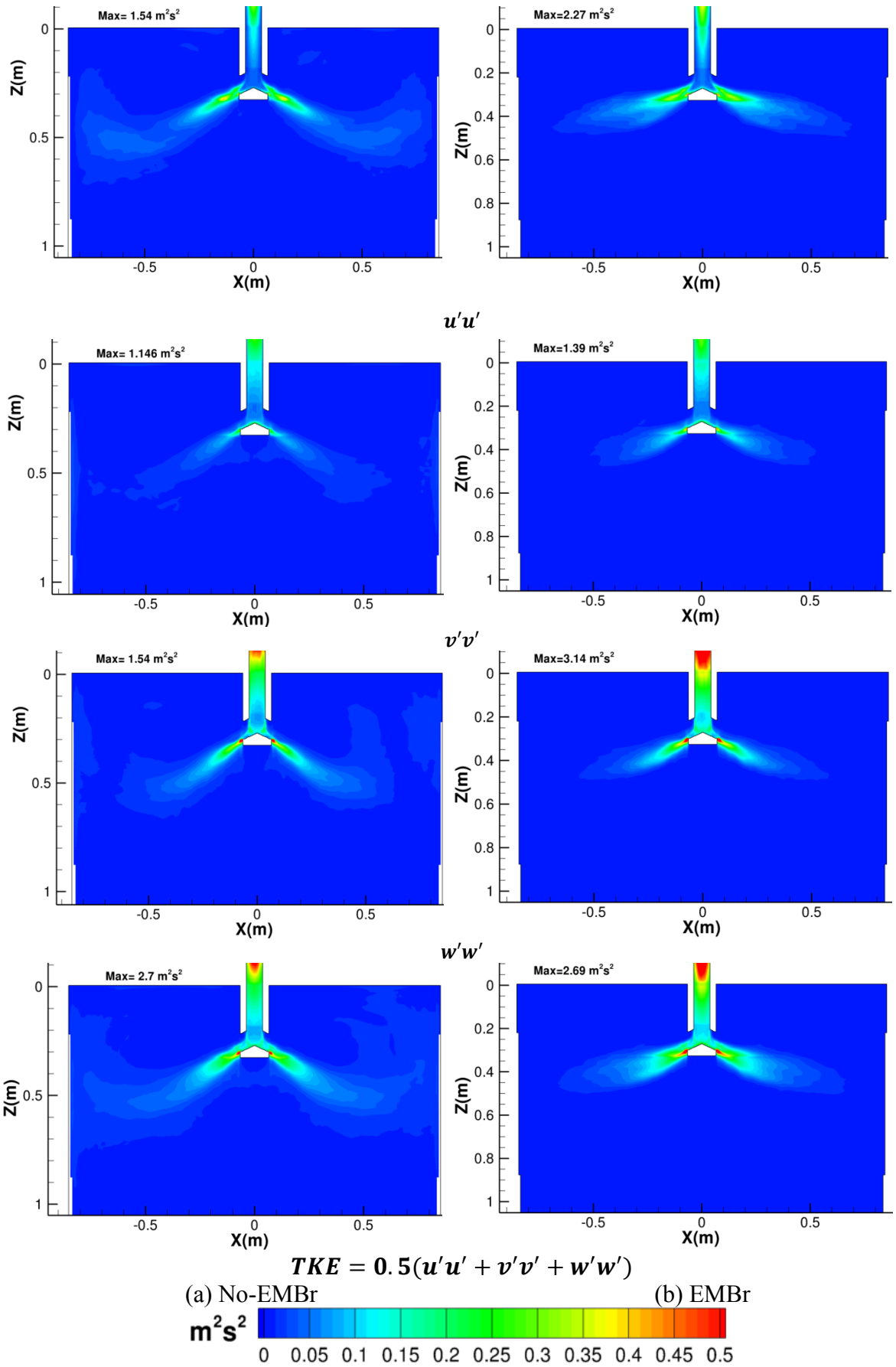

Figure 4.12 Contour plots of normal components of Reynolds stresses and Turbulent Kinetic Energy (TKE) in the mold region for (a)No-EMBr case and (b)EMBr case

4.3.2.2 Nozzle Flow

Figure 4.13 shows contour plots of the time-averaged velocity magnitude, with vectors of V_z and V_x components of velocity, in the SEN region for both cases. The contour plots look symmetric for both cases indicating sufficient averaging time. The mountain-bottom SEN produces thin and strong jets [45], which are observed both in the No-EMBr case and EMBr case. The flow inside the SEN ports are the same in both cases as the FC-Mold EMBr configuration applies a low magnetic field at the SEN bottom region. The jets exiting the ports have the same downward angle in both cases, but the jet in the EMBr case is deflected slightly upwards as it enters the mold. The applied magnetic field also reduces the velocities in the recirculation region above and below the jet.

To study the flow at the port exits, time-averaged velocity magnitude and TKE are shown along the vertical line on midplane between the wide faces, in Figure 4.14 and Figure 4.15 respectively. As expected, these variations are very similar for both the No-EMBr and

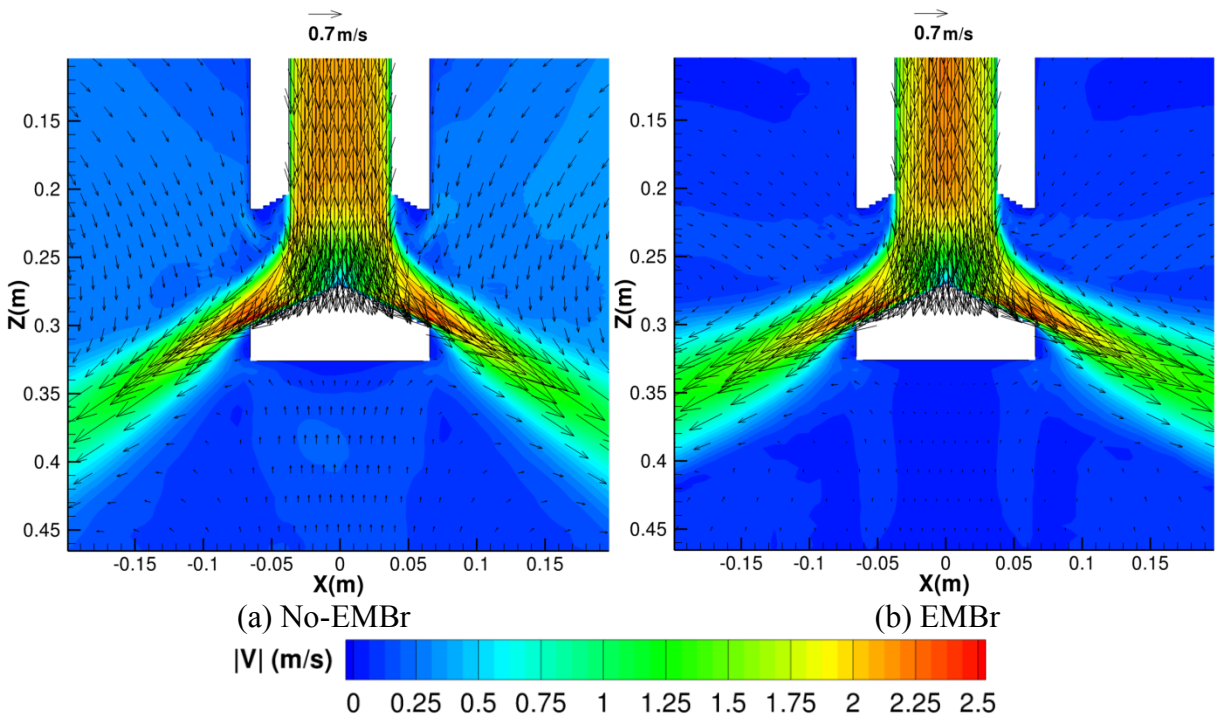

Figure 4.13 Contour plots of time-averaged velocity magnitude with vectors of V_z and V_x in the SEN region for (a) No-EMBr case and (b) EMBr case

the EMbr cases as the magnetic field has only a small effect in this region. The velocity magnitude is small at the top of the ports and remains low till midway between the top and bottom walls of the ports, after which it continuously rises reaching its maximum close to the bottom of the port exits. The variation of the TKE is more complicated with the values being greater for the EMBr case everywhere along the port exit except close to the top. This contradicts our understanding of the applied magnetic field suppressing turbulent fluctuations. However, this phenomenon can be explained by the fact that the flow inside the SEN is initially laminarized by the upper ruler while entering the mold region and then becomes turbulent again as it reaches the nozzle bottom where the magnetic field strength is small.

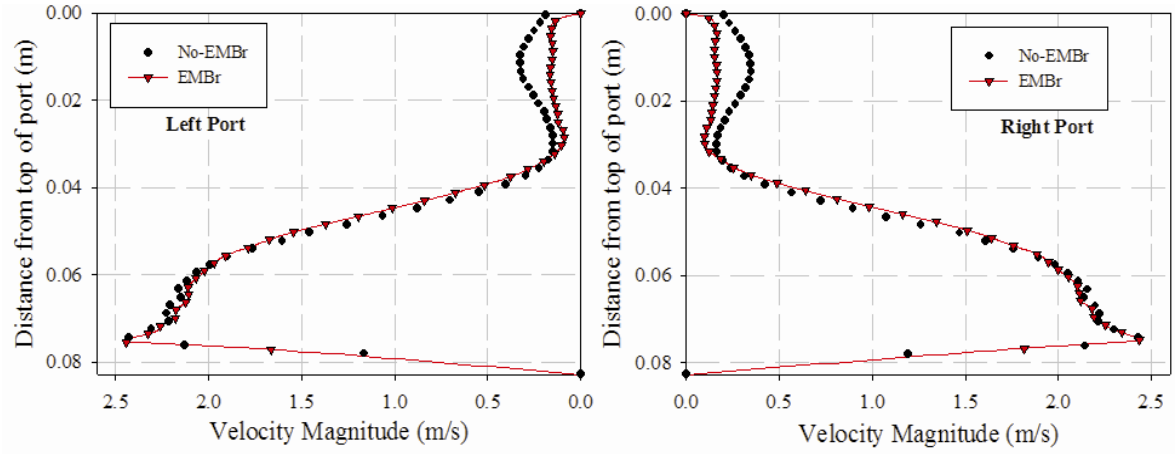

Figure 4.14 Variation of time-averaged velocity magnitude along a vertical line, on midplane between wide faces, at the port exits

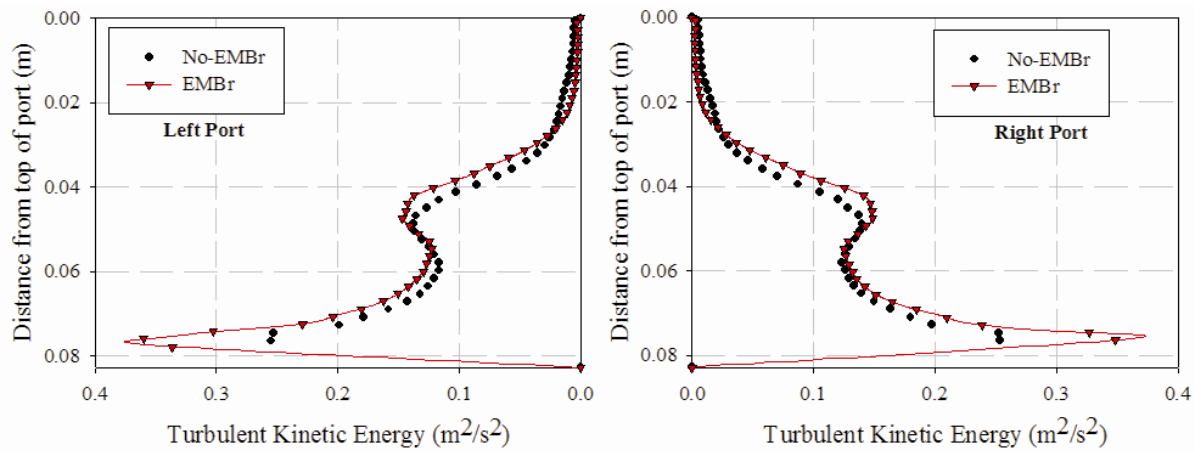

Figure 4.15 Variation of TKE along a vertical line, on midplane between wide faces, at the port exits

4.3.2.3 Surface Flow

As discussed earlier the surface flow is critical to the steel quality. Very high surface velocities may cause entrainment due to shear-layer instability [2], whereas very low surface velocities make the meniscus prone to freezing. Thus the ideal surface velocity would be somewhere in between the upper and lower threshold to avoid effects from either mechanism. The ideal range for top surface velocity was reported as 0.26 m/s to 0.43 m/s [2], however the exact number will change depending on the superheat, slag-layer properties, and other conditions. Figure 4.16a and Figure 4.16b show the variation of time-averaged surface velocity across the mold width and thickness respectively. Across the mold width the No-EMBr has a high surface velocity with the maximum (Max. ~0.55 m/s) occurring midway between the SEN and the NF. The surface velocity for the EMBr case is small compared to the No-EMBr case (Max.~0.09 m/s). The variation across the thickness of the mold at X=0.3m is nearly uniform for the No-EMBr case. The EMbr case is seen to have a typical M-shaped profile in the thickness direction with maximum velocity close to the walls. The M-Shaped profile has been reported in previous studies involving MHD flows with transverse magnetic fields [54].

Thus both cases have surface velocities that are not within the ideal range. It would be recommended to optimize the EMbr case in order to achieve the desired surface velocity as the No-EMBr case has other issues, such as unbalanced mold flow. The surface velocity in the EMBr case could be increased by tailoring the applied magnetic field. This could be done by either moving the lower ruler upwards or decreasing the strength of the upper ruler or both until optimized surface flow is achieved.

(a)

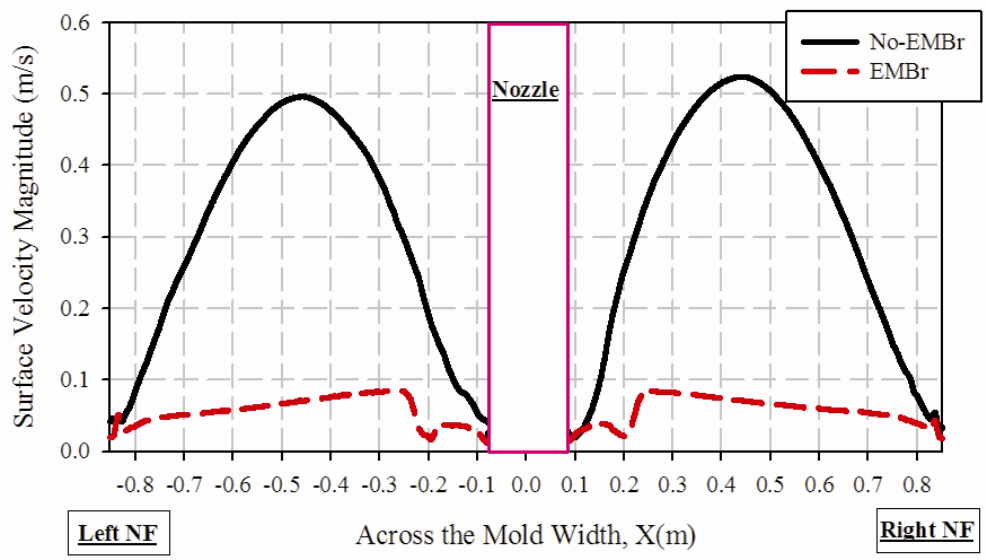

(b)

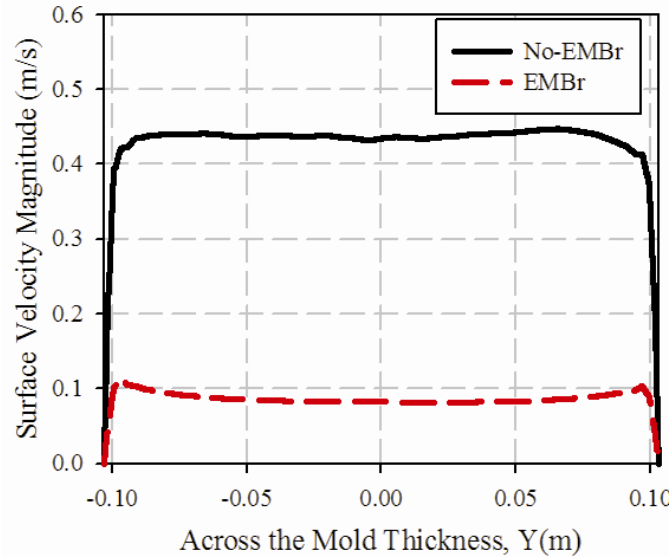

Figure 4.16 Variation of time-averaged velocity magnitude (a) across the width of the mold on the top surface at Y=0 mm and (b) across the thickness of the mold at X=0.3m

4.4 Comparison with Nail Board Measurements

The calculations for the No-EMBr case were performed at the same operating condition as the measured commercial caster, except with no argon gas injection. Nail board measurements were made in the industrial caster which had 4.37% volume fraction of argon injected into the SEN. Figure 4.17 shows the schematic of the steps involved in the nail board measuring technique. The nails are dipped into the molten steel for 3-5 seconds and the flow around the nail imprints its characteristics on the solidified lump. The kinetic energy of the molten steel is converted to potential energy, which results in slope on the top of the lump

with the height decreasing in the direction of the flow. Rietow and Thomas [18] performed a CFD analysis of the nail board dipping and based on these calculations and validation measurements in a steel caster, Rui et al. [9] established a correlation between the lump height difference and the surface velocity as shown in Figure 4.18.

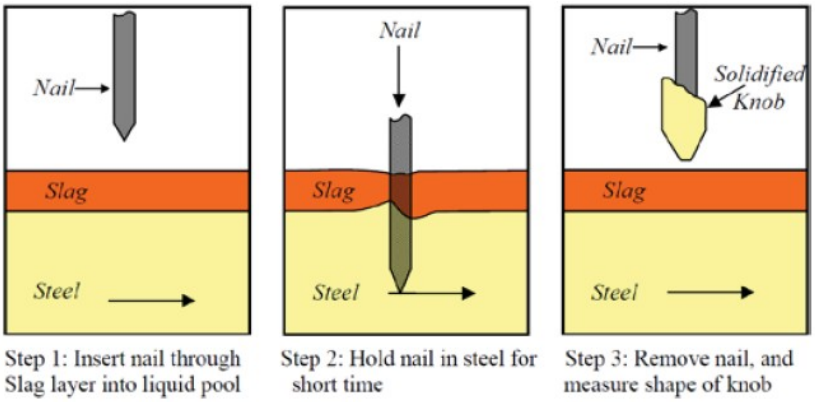

Figure 4.17 Nail Board Test Procedure [13]

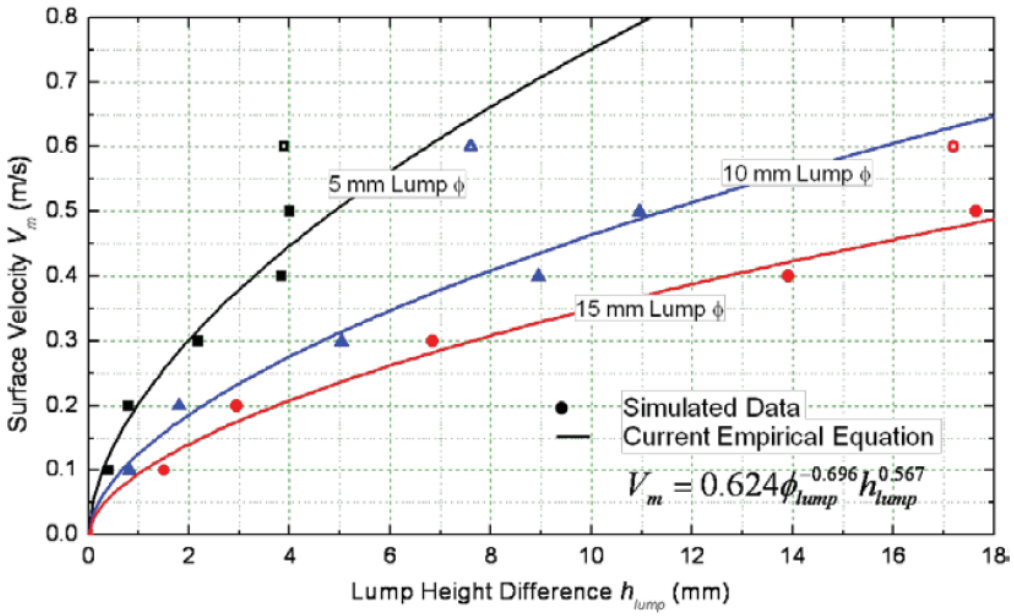

Figure 4.18 Graph to convert height difference at the lump into surface velocity [9]

Figure 4.19 shows photographs of the front and bottom view of the nail board used for taking these measurements. There were two rows of nails along the width of the mold and were referred to as the row closer to the Outer Radius (OR) and Inner Radius (IR). Figure 4.20 compares the measured and calculated surface velocity magnitude across the width of the

mold on the OR and IR rows. The measured surface velocity has high values close to the NF whereas the time-averaged calculation predicts highest values midway between the NF and

(a)

(b)

Figure 4.19 Pictures of the nail board used for the measurements at the commercial steel caster (a) front view and (b) bottom view

SEN. This could be explained by the unbalanced mold flow behavior discussed previously. The measurements could have been taken at the instant when there was dominant recirculation in this half of the mold. In order to match the measured values better, instantaneous velocity magnitude values are plotted at a similar unbalanced flow phase (Figure 4.20). These instantaneous values have similar maximum values as the measurements, but the maximum still occurs midway between the SEN and the narrow face. Some other reasons for differences, between measurements and calculations, are the assumption of single phase in the calculations, measurements providing only instantaneous values, and experimental errors. A pictorial comparison of the measured and calculated velocity vectors is also presented in Figure 4.21.

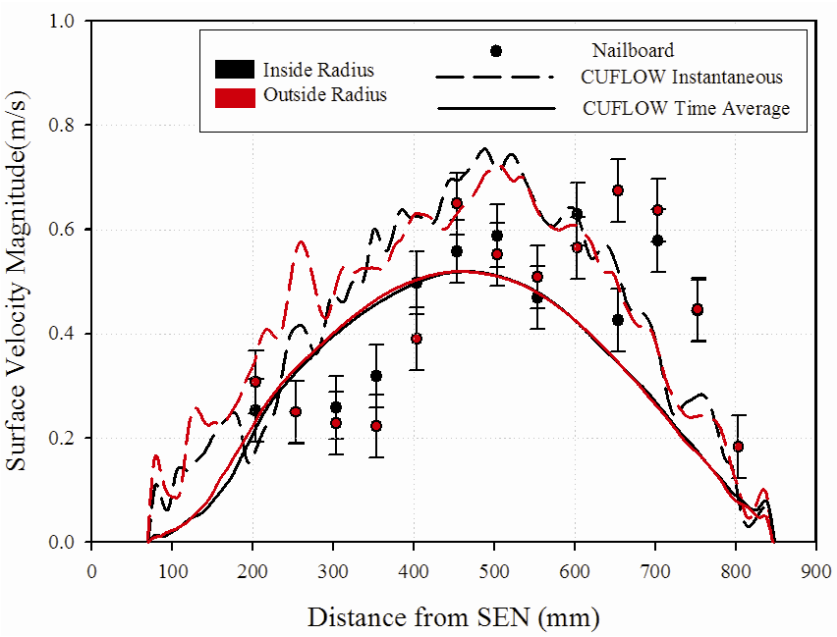

Figure 4.20 Comparison of measured and calculated surface velocity magnitude on the two rows of nails on the nail board

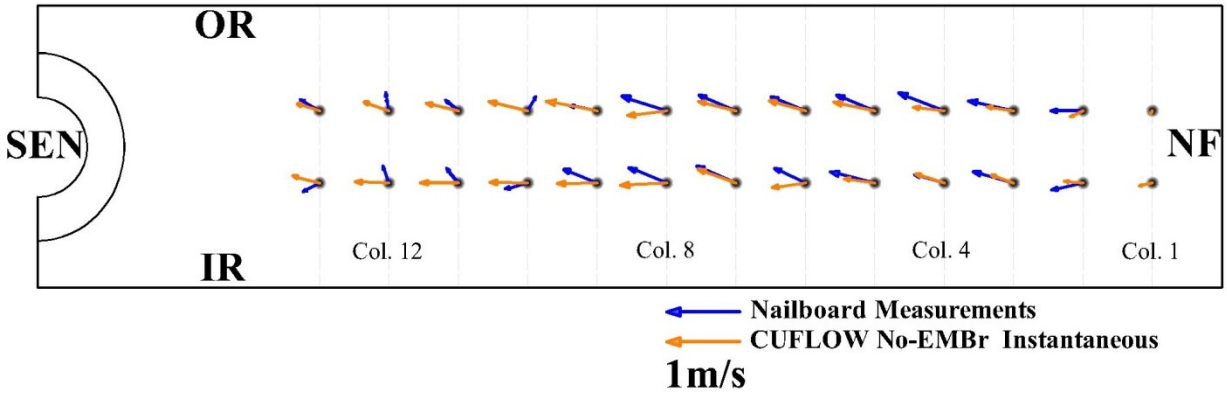

Figure 4.21 Comparison of measured and calculated surface velocity vectors

4.5 Summary and Conclusions

Large eddy simulations of a real caster at industrial operating conditions were conducted in the present study. To understand the effect of EMBr configuration, the first case studied was without any applied magnetic field and the second was with a FC-Mold EMBr configuration.

In the No-EMBr case, a classic double-roll flow pattern is observed with transient unbalanced flow. The upper loops have large velocities which resulted in high variation in the surface

level profile, (~22mm), large surface level fluctuations (~ +/- 12mm) and high surface velocities (up to 0.6m/s). The lower loops penetrated deep into the strand and also have unbalanced transient behaviour, with lower velocities.

Relative to the No-EMBr flowfield, application of the FC-Mold magnetic field damped the unbalanced behavior and made the mold flow much more stable. The upper rolls are weakened, resulting in a stable top surface with flatter surface level profile, extremely small level fluctuations and lower surface velocities. The surface velocity can be controlled by tailoring the applied magnetic field. The lower ruler could be moved upwards to deflect the jet upwards or the upper ruler could be reduced in strength. The lower rolls are restricted to a small recirculation below the jet and the flow below this region has low velocities which are mostly aligned in the casting direction. These low velocities below the jet region are beneficial in reducing the penetration depth and lower the chances of inclusions and bubbles being entrapped in the solidifying front deep in the caster.

The calculated surface velocities for the No-EMBr case were compared with nail board measurements taken at a typical commercial continuous caster of steel slabs. It is difficult to establish a fair comparison as the measurements only provide an instantaneous snapshot of the highly transient surface flow, and the effect of argon gas was ignored in the model. However, the measured surface flow direction was mostly from the NF to the SEN which agrees with the double-roll flow pattern predicted in the calculations. The measured velocity profile also agrees reasonably well.

4.6 References

1. D. Gupta and A. K. Lahiri, “Cold model study of slag entrainment into liquid steel in continuous slab caster,” *Ironmaking and Steelmaking*, vol. 23, no. 4, pp. 361–363, 1996.

2. L. C. Hibbeler and B.G. Thomas, “Mold slag entrainment mechanisms in continuous casting molds”, AISTech 2013 Steelmaking Conference Proc., Pittsburgh, PA, May 6-9, 2013.
3. M. Iguchi, et al., “Development of a Karman vortex probe for measuring the velocity of molten metal flow.”, *Materials Transactions, JIM,* Vol. 35, No. 10 (1994), p. 716-721.
4. M. Iguchi, et al., “Development and calibration of a Karman vortex probe for measurement of molten-steel velocities.” *Metallurgical and Materials Transactions B*, Vol 30 (B), Feb. 1999, p. 53-59.
5. M. Iguchi and Y. Terauchi., “Karman vortex probe for the detection of molten metal surface flow in low velocity range.”, *ISIJ International*, Vol. 42 (2002), No. 9, p. 939-943.
6. B. Melissari and S.A. Argyropoulos., “Measurement of magnitude and direction of velocity in high-temperature liquid metals. Part I. Mathematical modeling.”, *Metallurgical and Materials Transactions B*, Vol 36 (B), 2005, p. 691-700.
7. B. Melissari and S.A. Argyropoulos., “Measurement of magnitude and direction of velocity in high-temperature liquid metals. Part II: Experimental measurements.” *Metallurgical and Materials Transactions B*, Vol 36 (B), 2005, p. 639-649.
8. J. F. Domgin, et al., “Effect of process parameters variation on CC mold hydrodynamics and inclusion behaviour”, Revue de Metallurgie-CIT, No. 10, Oct. 2005, p. 703-710.
9. R. Liu, J. Sengupta, D. Crosbie, S. Chung, M. Trinh and B.G. Thomas, “Measurement of molten steel surface velocity with SVC and nail dipping during continuous casting process.”, *The Minerals, Metals & Materials Society,* 2011.
10. J. Kubota, et al., “Steel flow control in continuous caster mold by traveling magnetic field”, NKK Tech. Rev., 2001. p. 1-9.

11. P.H. Dauby, W.H. Emling, and R. Sobolewski, “Lubrication in the mold: A multiple variable system.” *Ironmaker and Steelmaker*, 1986. 13 (Feb): p. 28-36.
12. R. McDavid and B.G. Thomas, “Flow and thermal behavior of the top-surface flux powder layers in continuous casting molds”, *Metall. Trans. B*, 1996. 27B (4): p. 672-685.
13. K. Cukierski and B.G. Thomas, “Flow control with local electromagnetic braking in continuous casting of steel slabs.” *Metals and Materials Transactions B*, 2007.
14. B. Rietow and B.G. Thomas, “Using nail board experiments to quantify surface velocity in the CC mold.”, AISTech 2008 Steelmaking Conference Proc., Pittsburgh, PA, May 5-8, 2008.
15. H. Harada, T. Toh, T. Ishii, K. Kaneko, and E. Takeuchi., “Effect of magnetic field conditions on the electromagnetic braking efficiency.” *ISIJ International*, 41 (10): 1236–1244, 2001.
16. B. Li, T. Okane, and T. Umeda., “Modeling of molten metal flow in a continuous casting process considering the effects of argon gas injection and static magnetic-field application.”, *Metallurgical and Materials Transactions B*, 31: 1491–1503, 2000.
17. A. Idogawa, M. Sugizawa, S. Takeuchi, K. Sorimachi, and T. Fujii., “Control of molten steel flow in continuous casting mold by two static magnetic fields imposed on whole width.”, *Materials Science and Engineering: A*, 173 (1–2): 293 – 297, 1993.
18. K. Timmel, X. Miao, S. Eckert, D. Lucas, and G. Gerbeth., “Experimental and numerical modeling of the steel flow in a continuous casting mold under the influence of a transverse DC magnetic field.”, *Magnetohydrodynamics*, 46 (4): 437–448, OCT-DEC 2010.
19. K. Timmel, S. Eckert, and G. Gerbeth., “Experimental investigation of the flow in a continuous-casting mold under the influence of a transverse, direct current magnetic

field.", *Metallurgical and Materials Transactions B*, 42: 68–80, 2011. 10.1007/s11663-010-9458-1.

20. X. Miao, K. Timmel, D. Lucas, S. Ren, Z.and Eckert, and G. Gerbeth., "Effect of an electromagnetic brake on the turbulent melt flow in a continuous-casting mold.", *Metallurgical and Materials Transactions B*, 43: 954–972, 2012. 10.1007/s11663-012-9672-0.
21. R. Chaudhary, B. G. Thomas, and S. P. Vanka., "Effect of electromagnetic ruler braking (EMBr) on transient turbulent flow in continuous slab casting using large eddy simulations.", *Metallurgical and Materials Transactions B*, 43: 532–553, 2012. 10.1007/s11663-012-9634-6.
22. D. Kim, W. Kim, and K. Cho., "Numerical simulation of the coupled turbulent flow and macroscopic solidification in continuous casting with electromagnetic brake.", *ISIJ International*, 40 (7): 670–676, 2000.
23. K. Takatani, K. Nakai, N. Kasai, T. Watanabe, and H. Nakajima., "Analysis of heat transfer and fluid flow in the continuous casting mold with electromagnetic brake.", *ISIJ International*, 29 (12): 1063–1068, 1989.
24. M.Y. Ha, H.G. Lee, and S.H. Seong., "Numerical simulation of three-dimensional flow, heat transfer, and solidification of steel in continuous casting mold with electromagnetic brake." *Journal of Materials Processing Technology*, 133 (3): 322 – 339, 2003.
25. B.G. Thomas and L. Zhang., "Mathematical modeling of fluid flow in continuous casting.", *ISIJ International*, 41 (10): 1181–1193, 2001.
26. R. Chaudhary, C. Ji, B.G. Thomas, and S.P. Vanka., "Transient turbulent flow in a liquid-metal model of continuous casting, including comparison of six different methods.", *Metallurgical and Materials Transactions B*, 42: 987–1007, 2011.

27. Z. Qian, Y. Wu, B. Li, and J. He., “Numerical analysis of the influences of operational parameters on the fluid flow in mold with hybrid magnetic fields.”, *ISIJ International*, 42 (11): 1259–1265, 2002.

28. R. Kageyama and J.W. Evans., “Development of a three dimensional mathematical model of the electromagnetic casting of steel.”, *ISIJ International*, 42 (2): 163–170, 2002.

29. Y. Miki and S. Takeuchi., “Internal defects of continuous casting slabs caused by asymmetric unbalanced steel flow in mold.”, *ISIJ International*, 43 (10): 1548–1555, 2003.

30. T. Ishii, S.S. Sazhin, and M. Makhlouf., “Numerical prediction of magnetohydrodynamic flow in continuous casting process.”, *Ironmaking & Steelmaking*, 23 (3): 267–272, 1996.

31. Y.Hwang, P. Cha, Ho-Seok Nam, Ki-Hyeon Moon, and Jong-Kyu Yoon., “Numerical analysis of the influences of operational parameters on the fluid flow and meniscus shape in slab caster with EMBr.”, *ISIJ International*, 37 (7): 659–667, 1997.

32. Q. Yuan, B.G. Thomas, and S.P. Vanka., “Study of transient flow and particle transport in continuous steel caster molds: Part I. Fluid Flow.”, *Metallurgical and Materials Transactions B*, 35: 685–702, 2004.

33. P.H. Dauby., “Continuous casting: make better steel and more of it!”, *International Journal of Metallurgy*, 109: 113–136, 0 2012.

34. R. Singh, B.G. Thomas and S.P. Vanka, “Effects of a magnetic field on turbulent flow in the mold region of a steel caster”, *Metallurgical and Materials Transactions B,* pp.1-21, May 2013.

35. A.F. Shinn and S.P. Vanka., “Large eddy simulations of film-cooling flows with a micro-ramp vortex generator.”, *Journal of Turbomachinery*, 135 (1): 011004, 2013.

36. R. Chaudhary, S. P. Vanka, and B. G. Thomas., “Direct numerical simulations of magnetic field effects on turbulent flow in a square duct.”, *Physics of Fluids*, 22 (7): 075102, 2010.

37. R. Chaudhary, A.F. Shinn, S.P. Vanka, and B.G. Thomas., “Direct numerical simulations of transverse and spanwise magnetic field effects on turbulent flow in a 2:1 aspect ratio rectangular duct.”, *Computers & Fluids*, 51 (1): 100 – 114, 2011.

38. R. Liu and B.G. Thomas, “Transient turbulent flow simulation with water model validation and application to slide gate dithering.”, AISTech 2012 Steelmaking Conference Proc., Atlanta, GA, May 7-10, 2012.

39. J. Iwasaki and B.G. Thomas., “Thermal-mechanical model calibration with breakout shell measurements in continuous steel slab casting”, pp. 355–362. John Wiley & Sons, Inc., 2012. ISBN 9781118357002.

40. R. Chaudhary, B.T. Rietow, and B.G. Thomas., “Differences between physical water models and steel continuous casters: A theoretical evaluation.”, Inclusions in Clean Steel, Mater. Sci. Technol., AIST/TMS, Pittsburgh, PA, 2009, pp. 1090-1101.

41. H. Werner and H. Wengle., “Large-eddy simulation of turbulent flow over and around a cube in a plate channel.”, In *8th Symposium on Turbulent Shear Flows*, pages 155–168, 1991.

42. B.G. Thomas, “The making, shaping and treating of steel: Chap. 14”, 11th ed.,Casting Volume, A.W. Cramb, ed., The AISE Steel Foundation,Warrendale, PA, 2003.

43. H. Bai and B. G. Thomas, “Turbulent flow of liquid steel and argon bubbles in slide-gate tundish nozzles: Part I. model development and validation,” *Metallurgical and Materials Transactions B*, vol. 32, no. 2, pp. 253–267, 2001.

44. H. Bai and B. G. Thomas, “Turbulent flow of liquid steel and argon bubbles in slide-gate tundish nozzles: Part II. Effect of operation conditions and nozzles design,” *Metallurgical and Materials Transactions B*, vol. 32, no. 2, pp. 269–284, 2001.

45. R. Chaudhary, GG. Lee, B.G. Thomas and S-H Kim, “Transient mold fluid flow with well- and mountain-bottom nozzles in continuous casting of steel”, *Metallurgical and Materials Transactions B*, vol. 39, no. 6, pp. 870–884, 2008.

46. D. Gupta and A. K. Lahiri, “Water-modeling study of the surface disturbances in continuous slab caster,” *Metallurgical and Materials Transactions B*, vol. 25, no. 2, pp. 227–233, 1994.

47. S.-M. Cho, G.-G. Lee, S.-H. Kim, R. Chaudhary, O.-D. Kwon, and B. G. Thomas, “Effect of stopper-rod misalignment on asymmetric flow and vortex formation in steel slab casting,” in Jim Evans Honorary Symposium, in Proceedings of The Minerals, Metals, and Materials Society 139th Annual Meeting, pp. 71–77, The Minerals, Metals, and Materials Society, 2010.

48. B. Li, T. Okane, , and T. Umeda, “Modeling of biased flow phenomena associated with the effects of static magnetic-field application and argon gas injection in slab continuous casting of steel,” *Metallurgical and Materials Transactions* B, vol. 32, no. 6, pp. 1053–1066, 2001.

49. Q. He, “Observations of vortex formation in the mould of a continuous slab caster,” *ISIJ International*, vol. 33, no. 2, pp. 343–345, 1993.

50. M. Gebhard, Q. He, and J. Herbertson, “Vortexing phenomena in continuous slab casting moulds,” in 76th Steelmaking Conference Proceedings, pp. 441–446, The Iron and Steel Society, 1993.

51. J. W. Rottman, “Steep standing waves at a fluid interface,” *Journal of Fluid Mechanics*, vol. 124, pp. 283–306, 1982.

52. C. Ojeda, B. G. Thomas, J. Barco, and J. Arana, “Model of thermal-fluid flow in the meniscus region during an oscillation cycle,” in Proceedings of AISTech, vol. 2, pp. 269–283, The Association for Iron and Steel Technology, 2007.

53. R. Moreau., “Magnetohydrodynamics”, Kluwer Academic Pub. Co., Norwell, MA, 1990, pp. 110-64.

54. J.C.R. Hunt, “Magnetohydrodynamic flow in rectangular ducts”, *Journal of Fluid Mechanics*, vol. 21, part 4, pp. 577-590, 1965.

CHAPTER 5- CONCLUSIONS AND FUTURE WORK

5.1 Conclusions

The first part of this study involved development of CUFLOW, the in-house incompressible Navier-Stokes solver on GPUs. CUFLOW was developed to incorporate the capability of simulating flow in a computational domain with blocked solid-conducting regions. This feature has practical applications in continuous caster mold. The solidifying steel shell on the mold edges alters the effects of the applied magnetic fields on the fluid flow and thus should be considered while studying transient mold flow. The conducting shell acts as a finitely conducting boundary of the fluid domain. In the present study, the conducting shell was included in the simulation domain instead of applying approximate boundary conditions to the fluid domain.

In Chapter 3 the CU-FLOW model was applied to simulate previous experiments conducted in a GaInSn scaled physical model of a caster at FZD, Dresden, Germany, where it was used to study mold flow without and with ruler EMBr in the presence of both insulating and conducting side walls.The calculated results were validated for each case by comparison with experimental measurements. The No-EMBr case had a double-roll flow pattern with a weaker upper roll due to the high submergence depth and the well-bottomed SEN design. The application of the ruler EMBr field deflected more fluid upwards strengthening the upper roll, increasing top surface velocity, increasing top surface fluctuations and increasing the slope of the top surface profile. In the case with insulated side walls, long scale and low frequency fluctuations resulted in an extremely unbalanced flow with side-to-side and up-and-down wobbling of the jets. In the presence of the conducting side walls, which approximate the solidifying shell in a real caster, the transient unbalanced flow behavior was damped resulting in a stable flow pattern.

A real-size caster model was developed by scaling every dimension of the GaInSn model six times. Mold flow in the real size caster was studied without EMBr and with single-ruler EMBr in the presence of a solidifying shell. The operating conditions were calculated by performing a similitude analysis with only the Stuart number maintained constant. The Stuart number scaling criterion resulted in a good match of the overall flow pattern and time averaged velocities between the GaInSn EMBr scale model case with conducting side walls and the real size caster case. The surface level profile and its fluctuations matched if scaled using the scaling factor calculated by taking the ratio of the Froude numbers. Whereas, if the length scaling factor (=6), is used the level profile and its fluctuations in the real size caster are overpredicted by the scaled model, owing to its higher Froude number.

In Chapter 4 the validated model is used to study mold flow in a real caster from a commercial steel slab caster, at industrial operating conditions. The mold flow was first studied without any applied magnetic field and then with a FC-Mold EMBr configuration. The No-EMBr case had a double roll-flow pattern with a strong upper loop and high surface flow velocities. The mold flow had transient unbalanced behavior which is detrimental to the steel quality. The application of the FC-Mold EMBr damped the unbalanced flow tendencies and resulted in a stable mold flow. However, the surface velocities in the EMBr case were low enough to make the meniscus prone to freezing. Thus the upper ruler field strength should be optimized to attain surface velocities within the ideal range. Finally, the calculated results were also compared well with the nail board measurements taken at the commercial caster.

5.2 Future Work

In order to better accommodate complex geometries, such as the UTN and slide gate assemblies in the caster, a boundary-fitted grid can be used in CUFLOW. A boundary-fitted grid would be advantageous as, with only slightly more complex transport equations, it could

approximate curved domain edges better and can also easily concentrate more grid points into regions with high gradients. The convergence of the Poisson equations can also be accelerated with the use of Algebraic Multigrid (AMG) method instead of the current geometric multigrid method.

Presently the model in CUFLOW is isothermal and single phase. The code should be extended to study heat transfer and multi-phase Lagrangian inclusion and argon gas transport. This would enable CUFLOW to perform full 3D turbulent flow simulations of real casters with coupled thermal, multiphase and magnetohydrodynamic effects. CUFLOW has been used here to study real casters with a FC-Mold EMBr configuration. It is recommended to perform parametric studies with various field strength ratios between the upper and lower coils to optimize mold flow.

APPENDIX A: SPATIAL DISCRETIZATION OF THE ELECTRIC POISSON EQUATION (EPE)

The Electric Poisson Equation (EPE) discussed in Equation 2.5 is discretized using the finite volume method on the staggered mesh. In the first step we integrate the equation over the scalar control volume Ω, shown in Figure A.1a.

$$\int_{\Omega} \boldsymbol{\nabla} \cdot (\sigma \boldsymbol{\nabla} \phi^{n+1})\, d\Omega = \int_{\Omega} \boldsymbol{\nabla} \cdot \left(\sigma(\boldsymbol{u}^n \times \boldsymbol{B_0})\right) d\Omega \qquad (A.1)$$

And then we apply the divergence theorem which yields

$$\int_{\partial\Omega} (\sigma \boldsymbol{\nabla} \phi^{n+1}) \cdot \boldsymbol{n}\, dA = \int_{\partial\Omega} \left(\sigma(\boldsymbol{u}^n \times \boldsymbol{B_0})\right) \cdot \boldsymbol{n}\, dA \qquad (A.2)$$

where the boundary $\partial\Omega$ is the sum of the six faces of the Cartesian control volume. This equation can be written as

$$\sum_{faces} \int_{A_{face}} (\sigma \boldsymbol{\nabla} \phi^{n+1}) \cdot \boldsymbol{n}\, dA = \sum_{faces} \int_{A_{face}} \left(\sigma(\boldsymbol{u}^n \times \boldsymbol{B_0})\right) \cdot \boldsymbol{n}\, dA \qquad (A.3)$$

The right side of Equation A.3 is the sum of the source terms from all six faces and is calculated explicitly using the velocities from the previous time-step. The calculation of the source term on the x_+ face of the control volume is shown in Equations A.4 to A.9.

$$S_{x+} = \sigma_{x+}\left(v_{x+} B^z_{0,x+} - w_{x+} B^y_{0,x+}\right) A_{x+} \qquad (A.4)$$

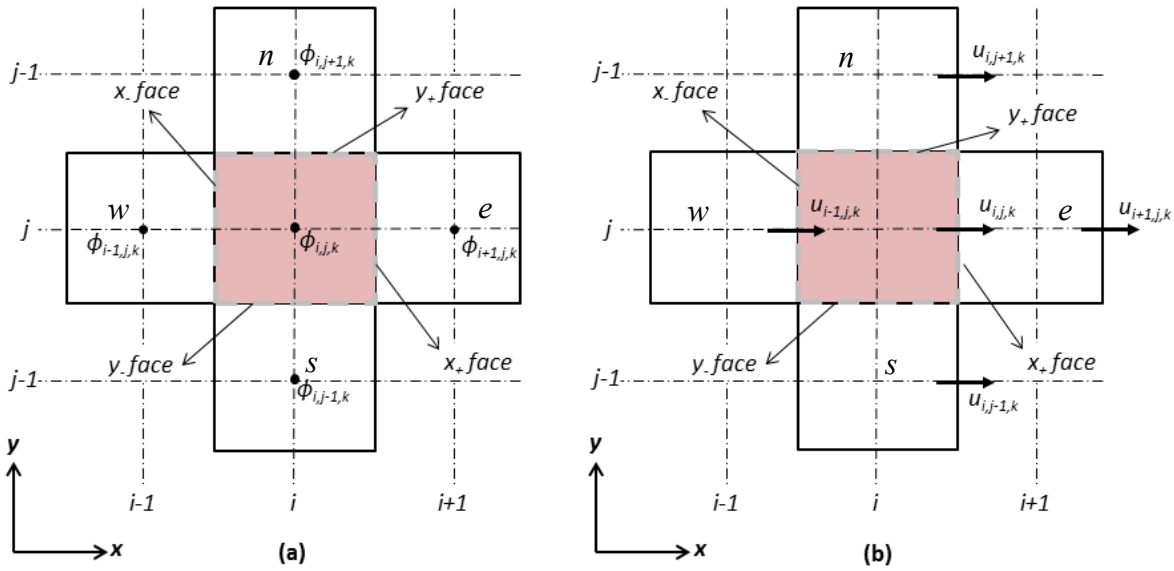

Figure A.1- The (a) scalar and (b) ***u*** control volumes indicated by the dashed boundaries

Where,

σ_{x+} is the harmonic averaged electrical conductivity on the x_+ face and is calculated as

$$\sigma_{x+} = \frac{2\sigma_{i+1}\sigma_i}{\sigma_{i+1} + \sigma_i} \qquad (A.5)$$

v_{x+} and $w_{x+}$are the averaged velocity components on the x_+ face which are calculated as

$$v_{x+} = \frac{1}{4}\left(v_{i,j,k} + v_{i,j-1,k} + v_{i+1,j,k} + v_{i+1,j-1,k}\right) \qquad (A.6)$$

$$w_{x+} = \frac{1}{4}\left(w_{i,j,k} + w_{i,j,k-1} + w_{i+1,j,k} + w_{i+1,j,k-1}\right) \qquad (A.7)$$

$B^z_{0,x+}$ and $B^y_{0,x+}$ are the averaged z and y components of the applied magnetic field on the x_+ face and are calculated as

$$B^z_{0,x+} = \frac{1}{2}\left(B^z_{0(i,j,k)} + B^z_{0(i+1,j,k)}\right) \qquad (A.8)$$

$$B_{0,x+}^{y} = \frac{1}{2}(B_{0(i,j,k)}^{y} + B_{0(i+1,j,k)}^{y}) \qquad (A.9)$$

and $A_{x+}$is the area of the x_+ face. Similarly, these steps are repeated for all six faces and the source terms are summed.

Now the integral on the left-hand-side of Equation A.3 is evaluated on all six faces of the control volume and the electric potential gradient is discretized using central differencing:

$$\int_{A_{x+}} (\sigma \boldsymbol{\nabla} \phi^{n+1}) \cdot \boldsymbol{i}\, dA = \int_{A_{x+}} \left(\sigma \frac{\partial \phi^{n+1}}{\partial \mathrm{x}} \right)_{x+} dA = \sigma_{x+} \frac{\phi_{i+1,j,k}^{n+1} - \phi_{i,j,k}^{n+1}}{(\Delta x_i + \Delta x_{i+1})/2} A_{x+} \qquad (A.10)$$

$$\int_{A_{x-}} (\sigma \boldsymbol{\nabla} \phi^{n+1}) \cdot -\boldsymbol{i}\, dA = \int_{A_{x-}} \left(\sigma \frac{\partial \phi^{n+1}}{\partial \mathrm{x}} \right)_{x-} dA = \sigma_{x-} \frac{\phi_{i,j,k}^{n+1} - \phi_{i-1,j,k}^{n+1}}{(\Delta x_i + \Delta x_{i-1)}/2} A_{x-} \qquad (A.11)$$

$$\int_{A_{y+}} (\sigma \boldsymbol{\nabla} \phi^{n+1}) \cdot \boldsymbol{j}\, dA = \int_{A_{y+}} \left(\sigma \frac{\partial \phi^{n+1}}{\partial \mathrm{y}} \right)_{y+} dA = \sigma_{y+} \frac{\phi_{i,j+1,k}^{n+1} - \phi_{i,j,k}^{n+1}}{(\Delta y_j + \Delta y_{j+1})/2} A_{y+} \qquad (A.12)$$

$$\int_{A_{y-}} (\sigma \boldsymbol{\nabla} \phi^{n+1}) \cdot -\boldsymbol{j}\, dA = \int_{A_{y-}} \left(\sigma \frac{\partial \phi^{n+1}}{\partial \mathrm{y}} \right)_{y-} dA = \sigma_{y-} \frac{\phi_{i,j,k}^{n+1} - \phi_{i,j-1,k}^{n+1}}{(\Delta y_j + \Delta y_{j-1})/2} A_{y-} \qquad (A.13)$$

$$\int_{A_{z+}} (\sigma \boldsymbol{\nabla} \phi^{n+1}) \cdot \boldsymbol{k}\, dA = \int_{A_{z+}} \left(\sigma \frac{\partial \phi^{n+1}}{\partial \mathrm{z}} \right)_{z+} dA = \sigma_{z+} \frac{\phi_{i,j,k+1}^{n+1} - \phi_{i,j,k}^{n+1}}{(\Delta z_k + \Delta z_{k+1})/2} A_{z+} \qquad (A.14)$$

$$\int_{A_{z-}} (\sigma \boldsymbol{\nabla} \phi^{n+1}) \cdot -\boldsymbol{k}\, dA = \int_{A_{z-}} \left(\sigma \frac{\partial \phi^{n+1}}{\partial \mathrm{z}} \right)_{z-} dA = \sigma_{z-} \frac{\phi_{i,j,k}^{n+1} - \phi_{i,j,k-1}^{n+1}}{(\Delta z_k + \Delta z_{k-1})/2} A_{z-} \qquad (A.15)$$

Substituting equations A.10 to A.15 into the original Equation A.3 yields

$$a_e p_{i+1,j,k}^{n+1} + a_w p_{i-1,j,k}^{n+1} + a_n p_{i,j+1,k}^{n+1} + a_s p_{i,j-1,k}^{n+1} + a_h p_{i,j,k+1}^{n+1} + a_l p_{i,j,k-1}^{n+1} - a_p p_{i,j,k}^{n+1}$$

$$= \sum_{faces} S_{face} \qquad (A.16)$$

where the coefficient use compass notation as subscripts (east, west, north, south, high, low). These coefficients are:

$$a_e = \frac{\sigma_{x+} A_{x+}}{(\Delta x_i + \Delta x_{i+1})/2} = \frac{\sigma_{x+} \Delta y_j \Delta z_k}{(\Delta x_i + \Delta x_{i+1})/2} \qquad (A.17)$$

$$a_w = \frac{\sigma_{x-} A_{x-}}{(\Delta x_i + \Delta x_{i-1})/2} = \frac{\sigma_{x-} \Delta y_j \Delta z_k}{(\Delta x_i + \Delta x_{i-1})/2} \qquad (A.18)$$

$$a_n = \frac{\sigma_{y+} A_{y+}}{(\Delta y_j + \Delta y_{j+1})/2} = \frac{\sigma_{y+} \Delta x_i \Delta z_k}{(\Delta y_j + \Delta y_{j+1})/2} \qquad (A.19)$$

$$a_s = \frac{\sigma_{y-} A_{y-}}{(\Delta y_j + \Delta y_{j-1})/2} = \frac{\sigma_{y-} \Delta x_i \Delta z_k}{(\Delta y_j + \Delta y_{j-1})/2} \qquad (A.20)$$

$$a_h = \frac{\sigma_{z+} A_{z+}}{(\Delta z_k + \Delta z_{k+1})/2} = \frac{\sigma_{z+} \Delta x_i \Delta y_j}{(\Delta z_k + \Delta z_{k+1})/2} \qquad (A.21)$$

$$a_l = \frac{\sigma_{z-} A_{z-}}{(\Delta z_k + \Delta z_{k-1})/2} = \frac{\sigma_{z-} \Delta x_i \Delta y_j}{(\Delta z_k + \Delta z_{k-1})/2} \qquad (A.22)$$

Thus the discrete equation, Equation A.16, is used to update the electric potential at each cell to the next time step $n + 1$. This equation represents a system of linear equation that has to be solved simultaneously.